Dynamics and spectroscopy of strongly coupled electrons and nuclei

Jonathan H. Fetherolf

Submitted in partial fulfillment of the
requirements for the degree of
Doctor of Philosophy
under the Executive Committee
of the Graduate School of Arts and Sciences

COLUMBIA UNIVERSITY

2021

Abstract

Dynamics and spectroscopy of strongly coupled electrons and nuclei

Jonathan H. Fetherolf

This thesis describes work on several research topics in which transport and spectroscopy are influenced by strong electron-nuclear or nuclear-nuclear interactions. First, I give a broad overview of the motivations and background for the main topics covered in this thesis. In the next section, I explore the applicability of perturbative quantum master equations to linear absorption and nonlinear two-dimensional and pump-probe spectroscopies. Next, I introduce a theory of charge transport in organic semiconductors that unifies two popular pictures: incoherent polaron hopping and transient localization due to dynamic disorder. In the next section, I investigate the impact of phonon anharmonicity on the charge transport dynamics of soft semiconductors. Finally, I present a new method of efficiently calculating anharmonic vibrational spectra from ab initio molecular potential energy surfaces.

Table of Contents

Acknowledgments vi

Dedication vi

Chapter 1: Introduction and Overview 1

1.1 Motivation 1

1.2 Background 2

1.2.1 Electronic-vibrational interaction 2

1.2.2 Vibrational anharmonicity 4

1.3 Outline 5

Chapter 2: Linear and nonlinear spectroscopy from quantum master equations 8

2.1 Introduction 8

2.2 Spectroscopy, correlation functions, and the quantum regression theorem 10

2.3 Model and Methods 13

2.3.1 Quantum master equations and TCL2 15

2.3.2 TCL2 master equation with frozen modes 16

2.4 Results 18

2.4.1 Model parameters and methodological details 18

2.4.2 Linear spectroscopy and population dynamics 19

2.4.3 Third-order nonlinear spectroscopy . . . 22

2.5 Conclusions . . . 26

Chapter 3: A unification of the Holstein polaron and dynamic disorder pictures of charge transport in organic crystals . . . 29

3.1 Introduction . . . 29

3.2 Theory . . . 31

3.2.1 Hamiltonian . . . 31

3.2.2 Conductivity and mobility . . . 32

3.2.3 One-particle spectral function . . . 37

3.2.4 Limiting behaviors and relation to previous works . . . 37

3.2.5 Discussion of approximations . . . 39

3.3 Results . . . 40

3.3.1 Simulation Details . . . 40

3.3.2 Spectral functions . . . 41

3.3.3 Optical conductivity . . . 42

3.3.4 DC mobility . . . 44

3.4 Conclusions . . . 50

3.5 Appendix: Validity of the approximate Lang-Firsov treatment . . . 52

3.5.1 Exact diagonalization over variational Hilbert space . . . 53

3.5.2 Spectral functions . . . 53

3.5.3 Optical conductivity . . . 56

Chapter 4: Conductivity of electrons coupled to anharmonic phonons . . . 58

4.1 Introduction . . . 58
4.2 Theory . . . 59
4.3 Results and Discussion . . . 63
4.3.1 Simulation Details . . . 63
4.3.2 Optical Phonon Anharmonicity . . . 63
4.3.3 Carrier Dynamics with Optical Phonons . . . 65
4.3.4 Acoustic Phonon Anharmonicity . . . 71
4.3.5 Carrier Dynamics with Acoustic Phonons . . . 72
4.4 Conclusions . . . 75

Chapter 5: Vibrational heat-bath configuration interaction . . . 77
5.1 Introduction . . . 77
5.2 Theory . . . 79
5.2.1 Vibrational heat-bath configuration interaction . . . 79
5.2.2 Epstein-Nesbet perturbation theory . . . 83
5.3 Results . . . 84
5.3.1 Software and simulation details . . . 84
5.3.2 Acetonitrile: A standard benchmark . . . 85
5.3.3 Ethylene: Sixth-order potential . . . 88
5.3.4 Ethylene oxide: Convergence and extrapolation . . . 89
5.3.5 Naphthalene: A 48-dimensional system . . . 94
5.4 Conclusions . . . 97

References . . . 116

Acknowledgements

First I would like to thank my wonderful advisor, Timothy Berkelbach. When I originally applied to the University of Chicago, Tim wasn't even listed on the department website yet, so I didn't consider him as a potential advisor. Then when we met, I quickly learned how well our scientific interests aligned, and I immediately loved his personable and enthusiastic approach. Throughout my time working with him, which included a move from UChicago to Columbia, he has been incredibly patient and generous in his support. All these qualities have made Tim an exceptional advisor, and I am so grateful to have him as a mentor. It has been an honor to play even a small part in his early career achievements.

I would also like to thank the rest of my dissertation committee at Columbia: David Reichman, Xiaoyang Zhu, Milan Delor and Chris Marianetti. David in particular has been very supportive in our interactions during my graduate career, going all the way back to my first visit to Columbia and our subsequent conversations where he encouraged me to join Tim's group. I also thank my second-year defense committee from UChicago: Suri Vaikuntanathan, Greg Engel and Jiwoong Park. I especially thank Suri for his support during my time there; I have many positive memories of his statistical mechanics course, our conversations at the James Franck Institute coffee hour, and hiking (and learning more statistical mechanics) with him in Telluride. I am also thankful for the support of my undergraduate research advisor, Edward Caster Jr. The opportunities and encouragement Ed gave me played a major part in my decision to pursue a PhD.

My colleagues in the Berkelbach group have played an extremely important and positive role in my PhD experience. Malte and Yeongsu started this journey with me, and I am so grateful that

I get to complete it with them. I am also grateful to Bryan, Sam and James for their presence and support in the transition from Chicago to New York. Since our move to Columbia, I have enjoyed the growth of the group and the lively atmosphere that my new colleagues have brought (even over Zoom). I particularly thank Tami for the enjoyable office discussions in our early days at Columbia, and Petra, who I am pleased to see carrying the torch for quantum dynamics in our group. I also thank our collaborator Denis Golež, who contributed to one of my most rewarding projects, and from whom I learned a great deal about many-body physics.

There are many other people who helped make my PhD a rich and rewarding experience. The camaraderie with my cohort helped me get through some tough early days at UChicago. I have fond memories of late nights in Kent basement with Laura, Harry, Chris, Hannah, Jake, Lawson, Elizabeth, and Vishnu, among others. Outside of academics, my involvement in graduate worker unionization has provided a profound source of camaraderie. I would particularly like to thank Clara, who has been a great friend throughout graduate school, and who introduced me to union organizing with Graduate Students United at UChicago. I would also like to thank the other organizers with whom I spent many rewarding hours, particularly Bodhi, Elizabeth and Yanan, as well as our amazing staff organizer Tyler. I immediately got involved with Graduate Workers of Columbia upon moving to New York, and I particularly thank Colleen and Ki Young for being so welcoming.

Finally, I thank my family for their constant support. Moving back home during the pandemic has been a struggle, and but I am grateful that it gave me the opportunity to spend more time with the people I love. Thank you so much for putting up with me.

For my father

Chapter 1: Introduction and Overview

1.1 Motivation

Theory has the unique ability to give a microscopic description of macroscopic observations. However, to glean experimentally relevant information, one must study systems of sufficient size and complexity. This is particularly true in the condensed phase, where one must contend with systems that are infinite from the microscopic viewpoint. The situation is complicated further when symmetries are broken by strong interactions. When faced with such a problem, the theorist is forced to make choices about which components and interactions to treat exactly, which to treat approximately, and which to ignore entirely.

Two of the most ubiquitous approximations throughout chemistry and physics are the Born-Oppenheimer approximation for electrons and nuclei and the harmonic normal-mode approximation for vibrations. Much of quantum chemistry is rightfully performed without questioning their validity. However, there are some classes of problem for which violation of these conditions are central, such as charge and energy transfer in the condensed phase. In this case, other simplifying approximations have been devised. These approximations often still rely on a separation of energy scales – for instance, weak-coupling perturbation theory for electron-phonon coupling, or vibrational perturbation theory for anharmonicity in molecules. In this thesis, I present research on several systems in which strong electron-nuclear or nuclear-nuclear interactions preclude a simple perturbative treatment. Furthermore, I focus on developing theoretical tools most useful for connecting microscopic dynamics with experimental observables such as spectroscopy and transport measurements.

1.2 Background

1.2.1 Electronic-vibrational interaction

The research I present in Chapters 2-4 focuses on systems in which electrons couple strongly to nuclear motions. The generic form of the Hamiltonian is

$$H = H_{\text{el}} + H_{\text{vib}} + H_{\text{el-vib}}, \tag{1.1}$$

where H_{el} is the electronic Hamiltonian, H_{vib} is the vibrational Hamiltonian, and $H_{\text{el-vib}}$ is the electronic-vibrational interaction. I focus on models that assume H_{el} and H_{vib} to be collections of simple one-body operators, with the challenging many-body physics residing in the interaction term $H_{\text{el-vib}}$. In Chapter 2, H_{el} describes a Frenkel exciton, like that which arises from photoexcitation of a multi-chromophore light-harvesting complex. In Chapter 3 and 4 the electronic system describes a single-band charge carrier – an electron in the conduction band or hole in the valence band – like that produced by (photo) doping of an organic semiconductor. Although the details differ between models, H_{vib} almost always represents one or more *harmonic* modes whose displacement couples *linearly* to the energy of the electronic system. While the dynamics of H_{el} and H_{vib} are trivial on their own, the interaction between them is responsible for the complex many-body processes of charge and energy transport.

I will first discuss the problem of nonadiabatic energy transfer in a multi-chromophore system due to coupling to a vibrational bath. This subject has garnered significant theoretical and experimental interest in recent years, with the ultimate goal of using insight from biological energy transfer to aid in chemical and material design [1]. Nonlinear optical spectroscopy is an important experimental probe of such systems, but it is difficult to unambiguously connect experiments to microscopic dynamics [2, 3]. This ambiguity has led to differing interpretations of the relative importance of electronic quantum coherence, incoherent hopping, and coherent vibronic mixing [4, 5]. Progress in this area requires development of theoretical techniques that are practical for

generating both microscopic dynamics and their experimental signatures.

Many common dynamics methods rely on perturbation theory in the electronic-vibrational coupling. These include the time-local and time-nonlocal quantum master equations (TCL2 and TL2), and various Markovian offshoots such as Redfield theory, Lindblad equations and Bloch equations [6]. Naturally, due to their perturbative and Markovian nature, all of these approximate techniques fail in the presence strong electronic-vibrational coupling and non-Markovian "memory" effects [7]. Another class of methods, which includes Förster and Marcus theory, instead relies on perturbation theory on the inter-chromophore electronic coupling [8, 9]. Of course, these methods fail to capture quantum coherence arising from strong electronic coupling. A third broad category of approximate techniques is semiclassical methods, such as surface-hopping and mean-field Ehrenfest dynamics [10, 11]. These methods have the advantage of being non-perturbative in both the electronic and electronic-vibrational coupling, but their semiclassical nature means that nuclear quantum effects are neglected. Many interesting systems fall within a regime where the none of these approximations are fully justified. To cope with these conditions, numerically exact techniques have been to developed, of which the Hierarchical Equations of Motion (HEOM) has gained widespread use [12, 13]. However, HEOM scales poorly with system size and can display troubling numerical instabilities [14].

The state of theory for charge transport in organic semiconductors is quite similar. In this case, the electronic system is a free carrier rather than a Frenkel exciton, and it couples to discrete phonon modes rather than a vibrational bath. The principle experimental observable of interest in such systems is the charge carrier mobility μ, which quantifies the drift of a carrier in an applied electric field. While organic semiconductors have many advantages of traditional materials such as low cost, mechanical flexibility and chemical tunability, their carrier mobility is much lower than traditional inorganic semiconductors, which severely limits their technological application [15]. Because of this drawback, it is a major theoretical goal to derive a set of design principles to maximize transport in these materials [16]. Doing so requires developing theories that can quantitatively predict carrier mobility while providing microscopic insight into its origin.

Theories of solid state charge transport follow a similar set of approximations to those already described. The traditional workhorse of solid state mobility calculations is the Boltzmann transport equation, which is derived via perturbation theory in the electron-phonon coupling [17]. Traditional inorganic semiconductors like silicon and germanium have sufficiently strong electronic coupling (wide electronic bands) that transport occurs in a coherent fashion and treating interaction with phonons perturbatively is justified. At the opposite extreme is Holstein's small polaron theory, in which carriers are sufficiently localized by their interactions with phonons that the electronic coupling is treated as a perturbation, and transport occurs via incoherent hopping [18]. This approximation was derived in the context of relatively poorly-conducting organic semiconductors. Many materials of interest exist in an intermediate regime, where mobility is too high for small polaron theory and too low for Boltzmann transport theory. For this regime, several important studies have gained insight with semiclassical methods, justifying this choice with the assertion that low-frequency lattice vibrations dominate transport [19, 20]. This has led widely-used dynamic disorder picture, in which carriers display features of both localization and band transport [21]. This picture, however, entirely ignores nuclear quantum effects, and is only valid for low-frequency phonon modes. In reality, a wide range of phonons are relevant, suggesting the need for a theory that accounts both for low-frequency dynamic disorder and nuclear quantum effects [22, 23].

1.2.2 Vibrational anharmonicity

In Chapters 4 and 5, the scope of this thesis expands to include many-body interactions in the vibrational Hamiltonian H_{vib}. It can be generically written as

$$H_{\text{vib}} = \sum_{i=1}^{N} \frac{1}{2} \left[P_i^2 + \omega_i^2 Q_i^2 \right] + V^{\text{an}}(Q_1, Q_2, \ldots, Q_N), \tag{1.2}$$

where ω_i, P_i and Q_i are the frequency and mass-weighted momentum and displacement for vibrational mode i. Under the harmonic approximation, the Hamiltonian is given by the first term, and

it is composed of N 1-body operators. In reality the full (anharmonic) Hamiltonian contains up to N-body interactions.

The task of accurately treating H_{vib} in isolation is essential for extracting accurate vibrational spectra from ab initio electronic structure calculations. Of course, if all terms in V^{an} are small compared to the harmonic term, the task is much easier – the harmonic approximation is sound and only minor corrections are needed, if any. For such cases, vibrational perturbation theory or vibrational self-consistent field are safe and efficient choices [24–26]. However, if interactions between vibrational modes are strong, then a non-perturbative solution is needed. Classical and semiclassical methods are useful for finite temperature spectra [27]. However, obtaining an exact quantum mechanical vibrational spectrum is a many-body problem on par with strongly correlated electrons. Because of the similar complexity, several high-level electronic structure techniques have been borrowed, including configuration interaction, coupled cluster and dynamical renormalization group theory [28–30].

1.3 Outline

All work in the subsequent chapters was conducted and written in collaboration with and under the guidance of my advisor, Prof. Timothy C. Berkelbach.

In Chapter 2 we investigate the accuracy of the second-order time-convolutionless (TCL2) quantum master equation for the calculation of linear and nonlinear spectroscopies of multi-chromophore systems. We show that, even for systems with non-adiabatic coupling, the TCL2 master equation predicts linear absorption spectra that are accurate over an extremely broad range of parameters and well beyond what would be expected based on the perturbative nature of the approach. For third-order (two-dimensional) spectroscopy, the importance of population dynamics and the violation of the so-called quantum regression theorem degrade the accuracy of TCL2 dynamics. To correct these failures, we combine the TCL2 approach with a classical ensemble sampling of slow microscopic bath degrees of freedom, leading to an efficient hybrid quantum-classical scheme that displays excellent accuracy over a wide range of parameters.

In Chapter 3 we present a unified and nonperturbative method for calculating spectral and transport properties of Hamiltonians with simultaneous Holstein (diagonal) and Peierls (off-diagonal) electron-phonon coupling. Our approach is motivated by the separation of energy scales in organic molecular crystals, in which electrons couple to high-frequency intramolecular Holstein modes and to low-frequency intermolecular Peierls modes. Our method reduces to the popular polaron picture due to Holstein coupling and the dynamic disorder picture due to Peierls coupling. For realistic parameters, temperature-dependent DC mobility is largely determined by the Peierls-induced dynamic disorder with minor quantitative corrections due to polaronic band-narrowing, and an activated regime is not observed at relevant temperatures. In contrast, for frequency-resolved observables, a quantum mechanical treatment of the Holstein coupling is qualitatively important for capturing the phonon replica satellite structure. Work on this project was done in collaboration with Dr. Denis Golež.

In Chapter 4, we investigate the effect of phonon anharmonicity on the carrier dynamics in organic semiconductors. Inspired by the success of trajectory-based methods in calculating mobilities of organic crystals, we perform semiclassical dynamics for carriers coupled to optical and acoustic phonons with anharmonicity up to fourth order. We find that the effect of moderate anharmonicity is well captured by a harmonic model with a temperature-dependent effective frequency. Phonon lifetime effects have relatively little impact on carrier transport due to the low frequency of the phonons. We find that for modes with significant softening, effective harmonic models are less accurate. This is especially true when mobility is calculated in the static disorder limit. Mode-softening due to a highly asymmetric potential leads to a nongaussian disorder profile that cannot be captured by a harmonic model. Work on this project was done in collaboration with Petra Shih.

Finally in Chapter 5, we introduce vibrational heat-bath configuration interaction (VHCI), an accurate and efficient method for calculating vibrational eigenstates of anharmonic systems. Inspired by its origin in electronic structure theory, VHCI is a selected CI approach that uses a simple criterion to identify important basis states with a pre-sorted list of anharmonic force constants. Screened second-order perturbation theory and simple extrapolation techniques provide significant

improvements to variational energy estimates. We benchmark VHCI on four molecules with 12 to 48 degrees of freedom and use anharmonic potential energy surfaces truncated at fourth and sixth order. When compared to other methods using the same truncated potentials, VHCI produces vibrational spectra of tens or hundreds of states with sub-wavenumber accuracy at low computational cost.

Chapter 2: Linear and nonlinear spectroscopy from quantum master equations

The material for this chapter was taken from Reference [31].

2.1 Introduction

Non-adiabatic energy transfer in molecular systems represents a problem of broad interest in chemistry, physics, and materials science. In the condensed phase, these processes commonly occur with many comparable energy scales, precluding simple perturbative treatments of the dynamics such as Golden-rule-type rate theories. This class of problems has motivated the important development of accurate numerical techniques capable of evolving the electronic reduced density matrix and offering insight into the population dynamics of multi-level dissipative quantum systems [12, 32–37]. However, with few exceptions, elements of the reduced density matrix are basis-dependent and not directly observable. Instead, the principal experimental probes of energy transfer dynamics are ultrafast time-resolved spectroscopies, such as pump-probe transient absorption and coherent two-dimensional spectroscopy [2–4, 38–40]. In this manuscript, we evaluate the accuracy of perturbative, but non-Markovian, quantum master equations for the calculation of linear and nonlinear spectroscopies. In particular, we focus on systems characteristic of protein-protected biological chromophores. This class of problems has been the topic of intense study in the quantum dynamics community [5, 41–47], in part because the environmental fluctuations exhibit long correlation times that challenge conventional theories [7, 13].

The Hamiltonian for multichromophore systems can be generically written as the sum of an electronic (system) Hamiltonian, a nuclear (bath) Hamiltonian, and the interaction between the two, $H = H_{\mathrm{s}} + H_{\mathrm{b}} + V$. In the present manuscript, we consider a Frenkel exciton model of coupled

chromophores, with the system Hamiltonian

$$H_{\mathrm{s}} = \sum_m \left(\overline{\epsilon} + \epsilon_m\right) B_m^\dagger B_m + \sum_{mn} J_{mn} B_m^\dagger B_n, \tag{2.1}$$

where $\overline{\epsilon}$ is a mean excitation energy for the excited-state manifold (equal to 10,000–30,000 cm^{-1} for visible-light absorbing chromophores), ϵ_m is the deviation from this mean excitation energy for site m, and J_{mn} is the electronic coupling between sites m and n. The operators $B_m^\dagger$ and B_m create and annihilate localized excitations on site m and satisfy the commutation relation $[B_m, B_n^\dagger] = \delta_{mn}(1 - 2B_m^\dagger B_m)$. The bath Hamiltonian is that of the nuclear degrees of freedom in the electronic ground-state. The system-bath interaction can be generically decomposed into the form $V = \sum_a E_a F_a$ where E_a are bath operators and F_a are system operators. For simplicity, we consider the case

$$V = \sum_m E_m B_m^\dagger B_m, \tag{2.2}$$

where E_m is a collective bath operator whose fluctuations act to modulate the energy gap of molecular site m. An otherwise generic second-order perturbation theory in the system-bath interaction requires only the equilibrium time correlation function of the nuclear degrees of freedom in the electronic ground state,

$$C_m(t) = \mathrm{Tr}_{\mathrm{b}} \left\{ E_m(t) E_m(0) \rho_{\mathrm{b}}^{\mathrm{eq}} \right\} \tag{2.3}$$

where $E_m(t) = \exp(iH_{\mathrm{b}}t/\hbar) E_m \exp(-iH_{\mathrm{b}}t/\hbar)$. For simplicity, we assume nuclear degrees of freedom belonging to different molecular sites are uncorrelated. This approach is commonly pursued to account for dephasing dynamics via atomistic simulations; in this approach, classical molecular dynamics are used to generate trajectories for the evaluation of the energy gap autocorrelation function in Eq. (2.3), leading to the second-order cumulant approximation to the lineshape [2, 48],

$$I_m(\omega) \propto \int_0^\infty dt e^{i\omega t} \exp\left[- \int_0^t dt_1 \int_0^{t_1} dt_2 C_m(t_2) \right]. \tag{2.4}$$

Strictly, the correlation function in Eq. (2.3) is a quantum time correlation function and a variety

of approximate schemes exist to reconstruct a quantum time correlation function from its classical counterpart [49, 50]. We note that the above formalism neglects energy transfer (or non-adiabatic effects) associated with the intermolecular couplings J_{mn}. In this $J_{mn} = 0$ limit of "pure dephasing," the second order cumulant approximation is quantum mechanically exact if the E_m operators are linear in the coordinates of a harmonic bath [51, 52]; this linear coupling model will be adopted below. In the more general case of energy transfer associated with population relaxation, spectroscopy calculations require a more general approach to quantum dynamics, which we discuss in the next section.

2.2 Spectroscopy, correlation functions, and the quantum regression theorem

In order to calculate spectroscopic observables, we augment our Hamiltonian with a light-matter interaction term to be treated via time-dependent perturbation theory [2],

$$H_{\text{spec}}(t) = H - \boldsymbol{\mu} \cdot \boldsymbol{E}(t); \tag{2.5}$$

here, $\boldsymbol{E}(t)$ is a classical electric field and $\boldsymbol{\mu}$ is the dipole operator

$$\boldsymbol{\mu} = \sum_m \mu_m (B_m^\dagger + B_m) \tag{2.6}$$

where, via the Condon approximation, the dipole matrix element μ_m is independent of the bath degrees of freedom. For simplicity, here and henceforth we neglect the vectorial nature of the transition dipole matrix element.

Linear absorption spectra are calculated from the equilibrium time-correlation response function,

$$S^{(1)}(t) = \frac{i}{\hbar}\theta(t)\text{Tr}\Big\{ [\mu(t), \mu]\, \rho^{\text{eq}} \Big\} = \frac{i}{\hbar}\theta(t)\text{Tr}\Big\{ \mu \mathcal{G}(t) \mu^\times \rho^{\text{eq}} \Big\} \tag{2.7}$$

where $\mu^\times A \equiv [\mu, A]$ and the Liouville-space propagator is defined by $\mathcal{G}(t)A = e^{-iHt/\hbar} A e^{iHt/\hbar}$.

Two-dimensional spectra are calculated from the third-order response function,

$$S^{(3)}(t_3,t_2,t_1) = \left(\frac{i}{\hbar}\right)^3 \theta(t_3)\theta(t_2)\theta(t_1) \times \mathrm{Tr}\Big\{\mu\mathcal{G}(t_3)\mu^\times\mathcal{G}(t_2)\mu^\times\mathcal{G}(t_1)\mu^\times\rho^{\mathrm{eq}}\Big\}. \tag{2.8}$$

With exact quantum dynamics, the above expressions produce exact spectra that contain the effects of coherence dephasing as well as population relaxation, with explicit treatment of system-bath correlations spanning multiple light-matter interactions.

As a one-time observable, the linear-response function can be calculated exactly from the time evolution of a reduced density-like operator

$$\rho_\mu(t) \equiv \mathrm{Tr_b}\Big\{\mathcal{G}(t)\mu^\times\rho^{\mathrm{eq}}\Big\} = \mathcal{G}_{\mathrm{red}}(t,0)\rho_\mu(0), \tag{2.9}$$

$$S^{(1)}(t) = \frac{i}{\hbar}\mathrm{Tr_s}\Big\{\mu\rho_\mu(t)\Big\} = \frac{i}{\hbar}\mathrm{Tr_s}\Big\{\mu\mathcal{G}_{\mathrm{red}}(t,0)\rho_\mu(0)\Big\}. \tag{2.10}$$

Therefore, any theory of reduced dynamics may be used to calculate the linear response function, such as a formally exact time-convolutionless quantum master equation [6, 53–56],

$$\frac{d\rho(t)}{dt} = -\frac{i}{\hbar}\left[H_{\mathrm{s}},\rho(t)\right] - \mathcal{R}(t)\rho(t) \equiv -\frac{i}{\hbar}\mathcal{L}_{\mathrm{red}}(t)\rho(t), \tag{2.11}$$

$$\rho(t) = T\exp\left[-\frac{i}{\hbar}\int_0^t d\tau\,\mathcal{L}_{\mathrm{red}}(\tau)\right]\rho(0) \equiv \mathcal{G}_{\mathrm{red}}(t,0)\rho(0), \tag{2.12}$$

where T is the time-ordering operator. Naturally, the lowest-order approximation to the time-dependent relaxation operator $\mathcal{R}(t)$ may be used; this is the second-order time convolutionless (TCL2) quantum master equation [6]. Unlike the second cumulant approach described in Sec. 2.1, the TCL2 master equation (detailed below) provides a perturbative description of population relaxation and coherence dephasing on equal footing. Importantly, in the absence of population relaxation, the TCL2 approximation yields uncoupled dephasing dynamics of the (in this case off-diagonal) reduced operator $\sigma(t)$ that are identical to those of the second-order cumulant approximation, and thus exact for linear coupling to a harmonic bath. In other words, the dynamical

resummation inherent in the TCL2 approximation is exact for this example of the pure-dephasing problem (due to underlying Gaussian statistics). We emphasize that this exactness is independent of the number of bath degrees of freedom, the energy scales of the bath, or the strength of the system-bath coupling.

However, in the presence of population relaxation with $J_{mn} \neq 0$, the TCL2 approximation is no longer exact, and its range of validity is commonly understood to be restricted to the nearly-Markovian, weak-coupling limit under which it is typically derived. We will demonstrate that such statements are completely dependent on the observable and *not* determined exclusively by the energy scales in the Hamiltonian. In particular, we will show that for the same Hamiltonian, TCL2 predicts qualitatively incorrect non-equilibrium population dynamics but quantitatively accurate linear absorption lineshapes.

Unfortunately, the simplicity of the linear response function is not maintained for higher-order correlation functions. If we were to generalize Eqs. (2.9) and (2.10) to the third-order response function, we might be led to the tempting approximation

$$\begin{aligned}\tilde{S}^{(3)}(t_3,t_2,t_1) = &\left(\frac{i}{\hbar}\right)^3 \theta(t_3)\theta(t_2)\theta(t_1) \\ &\times \mathrm{Tr_s}\Big\{\mu\mathcal{G}_{\mathrm{red}}(t_1+t_2+t_3,t_1+t_2) \\ &\qquad \times \mu^{\times}\mathcal{G}_{\mathrm{red}}(t_1+t_2,t_1)\mu^{\times}\mathcal{G}_{\mathrm{red}}(t_1,0)\rho_{\mu}(0)\Big\},\end{aligned} \tag{2.13}$$

which can be shown to be consistent with a quantum version of Onsager's regression hypothesis known as the quantum regression theorem (QRT) [57, 58]. In general, the QRT is not exact [59, 60]. The exact multi-time correlation function is related to the approximate one by a number of correction terms, which are non-vanishing even to lowest-order in the system-bath interaction [61–63]. To summarize, in the context of the current manuscript, *the rigorous calculation of nonlinear response functions requires more information than contained in quantum master equations*.

The violation of the QRT is intimately linked to the degree of non-Markovianity present in the reduced dynamics. For purely Markovian reduced dynamics, the QRT is exact [60, 64]. For weak

system-bath coupling leading to nearly Markovian reduced dynamics, the corrections to the QRT are small. In this manuscript, we will study the accuracy of TCL2 dynamics, within the approximation implied by the QRT, Eq. (2.13), for the simulation of two-dimensional spectroscopy. Unsurprisingly, we find that the results deteriorate with increasing non-Markovianity due to stronger coupling or slower bath degrees of freedom.

In order to maintain the simplicity of quantum master equations while seeking broad applicability to nonlinear spectroscopy, we will evaluate the use of the "frozen modes" approach, recently introduced by one of us and co-workers [65]. The method will be described in more detail below, but the idea is to simulate generically non-Markovian dynamics by an average over many independent nearly-Markovian trajectories. In each trajectory, the low-frequency bath degrees of freedom are dynamically arrested: they are removed from the master equation's relaxation operator and treated as a source of static disorder. This frozen-mode approximation is obviously best for low-frequency (slow) degrees of freedom, which are precisely those that contribute to non-Markovian behavior and the inaccuracy of perturbative quantum master equations. Compared to the original problem, each individual trajectory in the frozen modes approach exhibits less non-Markovian behavior and weaker system-bath coupling. Because these are the same effects responsible for the violation of the QRT in nonlinear response calculations, we will demonstrate that the frozen-mode variant of TCL2 dynamics leads to accurate two-dimensional spectra, even in highly non-Markovian regimes.

2.3 Model and Methods

For the remainder of this work, we will adopt the common system-bath model that assumes a harmonic nuclear bath linearly coupled to the system's excitation number operator, i.e. Eqs. (2.1) and (2.2) with

$$H_{\mathrm{b}} = \frac{1}{2} \sum_{m} \sum_{k} (P_{m,k}^2 + \omega_{m,k}^2 Q_{m,k}^2), \tag{2.14}$$

$$E_m = \sum_{k} c_{m,k} Q_{m,k}, \tag{2.15}$$

where $P_{m,k}$ and $Q_{m,k}$ are the mass-weighted momentum and position of mode k belonging to the nuclear degrees of freedom of site m. For such a simplified form of the system-bath interaction, *all* properties are determined solely by the equilibrium autocorrelation function in Eq. (2.3),

$$\begin{aligned} C_m(t) &= \sum_k c_{m,k}^2 \mathrm{Tr}_\mathrm{b} \left\{ Q_{m,k}(t) Q_{m,k}(0) e^{-\beta H_\mathrm{b}} \right\} / \mathrm{Tr}_\mathrm{b} e^{-\beta H_\mathrm{b}} \\ &= \frac{\hbar}{\pi} \int_0^\infty d\omega J_m(\omega) \Big\{ \coth(\beta\hbar\omega/2) \cos(\omega t) - i \sin(\omega t) \Big\}, \end{aligned} \tag{2.16}$$

where we have introduced the spectral density

$$J_m(\omega) = \frac{\pi}{2} \sum_k \frac{c_{m,k}^2}{\omega_{m,k}} \delta(\omega - \omega_{m,k}). \tag{2.17}$$

Note that the spectral density can be obtained from the real-part of the cosine-transform of the bath correlation function

$$J_m(\omega) = \tanh(\beta\hbar\omega/2) \int_0^\infty dt \cos(\omega t)\ \mathrm{Re} C_m(t), \tag{2.18}$$

which provides a way to extract a model spectral density from atomistic simulations of the energy gap autocorrelation function, as done recently for light-harvesting complexes [66, 67]. In the following, we assume all sites have identical spectral densities $J_m(\omega) = J(\omega)$ and employ an Ohmic spectral density with a high-frequency Lorentzian cutoff

$$J(\omega) = \frac{2\lambda\omega_c\omega}{\omega_c^2 + \omega^2}, \tag{2.19}$$

which follows from the assumption of an exponentially-decaying autocorrelation function (in the high-temperature limit), $\mathrm{Re} C(t) = 2\lambda k_\mathrm{B} T \exp(-\omega_c t)$. Therefore, the bath relaxation time is given by ω_c^{-1} and the magnitude of fluctuations is related to the reorganization energy $\lambda = (\hbar\pi)^{-1} \int_0^\infty d\omega J(\omega)/\omega$. We emphasize that most of our conclusions are not restricted to any particular form of $J(\omega)$, including those with arbitrary structure (as may be obtained from simulation).

Specifically, we expect that the *accuracy* of our results is only weakly dependent on the form of the spectral density, and can be safely applied to any system-bath Hamiltonian exhibiting only linear coupling to a harmonic bath. However, while the method is entirely *applicable* to more general system-bath Hamiltonians, the accuracy is harder to assess. For example, we note that even for the pure-dephasing problem, the second cumulant is no longer exact for systems that are quadratically-coupled to harmonic baths [51, 52].

2.3.1 Quantum master equations and TCL2

Introduced above, the TCL2 quantum master equation evolves reduced-density-like system operators $\sigma(t)$ according to the time-local equation of motion in Eq. (2.20). This equation of motion assumes a factorized initial condition of the total density-like operator $\rho(0) = \sigma(0)\rho_{\mathrm{b}}(0)$, and we henceforth assume that the initial bath density operator is at equilibrium, $\rho_{\mathrm{b}}(0) = \rho_{\mathrm{b}}^{\mathrm{eq}}$. We note that for Hamiltonians with a minimum excited-state gap that is much larger than thermal energy, the total equilibrium density operator is factorized to an excellent approximation, $\rho^{\mathrm{eq}} \approx |0\rangle\langle 0|\rho_{\mathrm{b}}^{\mathrm{eq}}$, justifying factorized initial conditions for equilibrium correlation functions. In the basis of eigenstates of the system Hamiltonian, the TCL2 relaxation superoperator $\mathcal{R}$ is a tensor with elements

$$\begin{aligned}\mathcal{R}_{\alpha\beta\gamma\delta}(t) &= \mathrm{Tr}_{\mathrm{s}}\left\{|\alpha\rangle\langle\beta|\,\mathcal{R}(t)\,[|\delta\rangle\langle\gamma|]\right\} \\ &= \Gamma^{+}_{\delta\beta\alpha\gamma}(t) + \Gamma^{-}_{\delta\beta\alpha\gamma}(t) \\ &\quad - \delta_{\beta\delta}\sum_{\zeta}\Gamma^{+}_{\alpha\zeta\zeta\gamma}(t) - \delta_{\alpha\gamma}\sum_{\zeta}\Gamma^{-}_{\delta\zeta\zeta\beta}(t),\end{aligned} \tag{2.20}$$

with

$$\Gamma^{\pm}_{\alpha\beta\gamma\delta}(t) = \frac{1}{\hbar^2}\sum_{m} N_m^{\alpha\beta} N_m^{\gamma\delta}\,\Theta^{\pm}_m(\omega_{\gamma\delta}; t) \tag{2.21}$$

and

$$\Theta^{\pm}_m(\omega; t) = \int_0^t d\tau e^{-i\omega\tau} C_m(\pm\tau). \tag{2.22}$$

In the above, $N_m^{\alpha\beta} = \langle\alpha|B_m^\dagger B_m|\beta\rangle$ and $C_m(t)$ is given in Eq. (2.16). The relevant dimensionless parameter that controls the accuracy of weak-coupling master equations is roughly given by $\lambda k_{\rm B}T/(\hbar\omega_c)^2$; in particular, very slow bath relaxation dynamics are a challenge as they violate the quasi-Markovian approximations inherent in such master equations. As such, we will also consider a quantum-classical hybrid scheme that microscopically treats slow nuclear degrees of freedom as static variables sampled from their respective canonical distributions, discussed next.

2.3.2 TCL2 master equation with frozen modes

The spectral density defined in Eq. (2.17) can formally be separated into fast and slow components under the condition that $J(\omega) = J_{\rm fast}(\omega) + J_{\rm slow}(\omega)$. In the ideal partitioning, the slow part is comprised of quasi-adiabatic modes that evolve much more slowly than the system and can safely be treated classically, while the fast part contains modes which evolve much more quickly than the system and therefore can be treated with nearly-Markovian weak-coupling theories [35, 68, 69]. The partitioning between slow and fast parts of $J(\omega)$ can be done with a switching function,

$$J_{\rm slow}(\omega) = s(\omega;\omega^*)J(\omega) \tag{2.23a}$$

$$J_{\rm fast}(\omega) = [1 - s(\omega;\omega^*)]J(\omega), \tag{2.23b}$$

where $s(\omega;\omega^*)$ is a function which goes from a value of 1 at $\omega = 0$ to a value of 0 at a specified splitting frequency $\omega = \omega^*$. Following previous work [65, 68, 69] we use the smooth switching function

$$s(\omega,\omega^*) = \begin{cases} [1-(\omega/\omega^*)^2]^2 : & \omega < \omega^* \\ 0 : & \omega \geq \omega^*, \end{cases} \tag{2.24}$$

which avoids long-time oscillatory features in the bath correlation function. The free parameter ω^* determines the set of modes to be treated classically. Two example partitionings of an Ohmic-Lorentz spectral density are shown in Fig. 2.1.

While the slow modes could be treated with several different semiclassical techniques, includ-

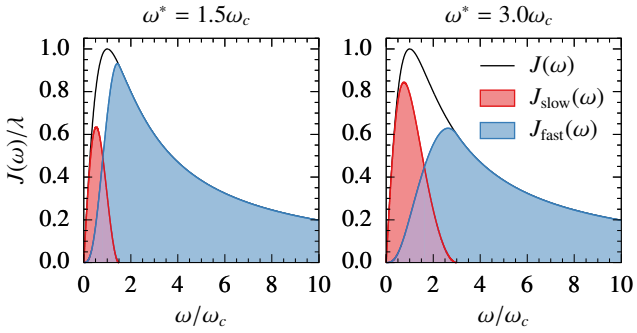

Figure 2.1. Two example partitionings of an Ohmic-Lorentz spectral density using different values of the splitting frequency ω^*; see Eqs. (2.23). Larger values of ω^* result in more modes being treated classically and fewer modes treated quantum mechanically, but perturbatively.

ing mean-field Ehrenfest dynamics [35, 68, 69], here we make the simplest approximation and treat the modes described by $J_{\text{slow}}(\omega)$ as completely frozen. In this case, positions of the slow degrees of freedom $Q_{m,k}$ are sampled from the Boltzmann distribution of a harmonic oscillator and used to alter the energy levels of the system Hamiltonian,

$$\epsilon_m \longrightarrow \epsilon_m + \sum_{k\in\text{slow}} \bar{c}_{m,k} Q_{m,k}(0), \tag{2.25}$$

where $\bar{c}_{m,k}$ is a renormalized coupling constant due to the partitioning enforced by the switching function $S(\omega;\omega^*)$. This new system Hamiltonian is used with the *fast* part of the spectral density to perform a single realization of TCL2 dynamics. This process is repeated and averaged. Further details and discussion of the method can be found in Ref. [65].

In the spectroscopic context, the frozen modes are most physically interpreted as a source of inhomogeneous broadening. If the nuclear degrees of freedom are extremely slow, so as to appear effectively frozen during the decay of the dipole autocorrelation function, then this is the correct result. We emphasize that this inhomogeneous broadening is entirely microscopic because it originates from degrees of freedom in the total Hamiltonian; it is not an artificial, unidentified source of inhomogeneous broadening. When applied to linear absorption spectra of systems without non-adiabatic effects, this approach is equivalent to the inhomogeneous cumulant expansion described in Refs. [2, 70], but differs for higher-order spectroscopies.

The combination of TCL2 dynamics with frozen-mode sampling (TCL2-FM) leads to many trajectories that are each *more Markovian* than the original problem. This property mitigates corrections to the QRT, which are not considered explicitly in this work. Furthermore, the TCL2-FM approach prevents the application of perturbation theory beyond its regime of validity (through the use of a faster, more weakly-coupled bath in the quantum master equation). As we show below, these two effects collectively produce semiquantitative accuracy in the prediction of nonlinear spectroscopy.

2.4 Results

2.4.1 Model parameters and methodological details

For simplicity, we present results for a system of two chromophores that has four accessible electronic states: the ground state, two states where each chromophore is separately excited, and one state where both chromophores are simultaneously excited. The absence of a quartic exciton-exciton interaction in Eq. (2.1) implies that the energy of the doubly-excited state is simply the sum of the excitation energies of the individual chromophores. In all results, we use the electronic parameters $\epsilon_1 = 50$ cm^{-1}, $\epsilon_2 = -50$ cm^{-1} and $J_{12} = 100$ cm^{-1}, along with the bath parameters $\omega_c^{-1} = 300$ fs and $T = 300$ K. The reorganization energy λ will be varied. The bath frequency and temperature lead to energy scales $\hbar\omega_c = 18$ cm^{-1} and $k_B T = 208$ cm^{-1}, i.e. all energy scales are comparable, with the bath frequency being the smallest. We emphasize that this particular parameter regime is studied here because it is well outside the range of validity of conventional quantum master equations.

Our TCL2 dynamics are generated with a fourth-order Runge-Kutta integrator. For TCL-FM calculations, the total spectral density was discretized into 300 modes, and those with $\omega > \omega^*$ were discarded. We performed 2×10^4 realizations of frozen-mode sampling to converge the dynamical observables. For all frozen-mode calculations, we use a splitting frequency that characterizes the timescale of isolated electronic dynamics, $\omega^* = [(\epsilon_1 - \epsilon_2)^2 + 4J_{12}^2]^{1/2}/6\hbar$. Other choices that differ by factors of order one give similar qualitative results, and occasionally better quantitative results,

but we find that the above form is reasonable over a broad range of parameters and observables.

All approximate results will be compared to numerically exact results obtained with the hierarchical equations of motion (HEOM) [12, 71, 72]; for the bath parameters used in our results, the HEOM calculations required zero Matsubara frequencies (i.e. the high-temperature approximation with $K = 0$), but as many as $L = 20$ levels in the hierarchy. For spectroscopy calculations, we use transition dipole matrix elements satisfying $\mu_1/\mu_2 = -5$ and spectra will be presented with arbitrary units. All calculations were performed with our open-source quantum dynamics package `pyrho` [73].

2.4.2 Linear spectroscopy and population dynamics

In the frequency domain, we present the imaginary (absorptive) part of the linear-response susceptibility,

$$\chi''(\omega) = \mathrm{Im} \int_0^\infty dt e^{i\omega t} S^{(1)}(t). \tag{2.26}$$

Again we emphasize that for the model Hamiltonian adopted here, the TCL2 master equation is identical to the second-cumulant approximation and exactly solves the pure-dephasing lineshape problem. In the case of excited-state electronic coupling $J \neq 0$, the TCL2 generalizes the second cumulant approximation. While it is not exact, the results are remarkably accurate, as shown in the right-hand column of Fig. 2.2, even for significant coupling to a slow bath. The TCL2-FM approach yields very minor quantitative improvements, which confirms that those local-frequency modes treated as frozen are properly interpreted as giving rise to inhomogeneous broadening.

Unlike the non-Markovian TCL2-based approaches, the Markovian Redfield theory predicts incorrect spectra, with an accuracy that deteriorates for increasing reorganization energy or increasing bath relaxation times. This can be understood simply from the Markovian limit of the relevant pure-dephasing term in the TCL2 tensor: $1/T_2^* = \hbar^{-1} \left[J(\omega) n(\omega)\right]_{\omega=0}$ where $n(\omega)$ is the Bose-Einstein distribution function. For the Ohmic-Lorentz spectral density employed here, one finds $1/T_2^* = 2\lambda k_\mathrm{B} T/\hbar\omega_c^2$. As shown in Fig. 2.2, this Markovian theory predicts linewidths that are much too large.

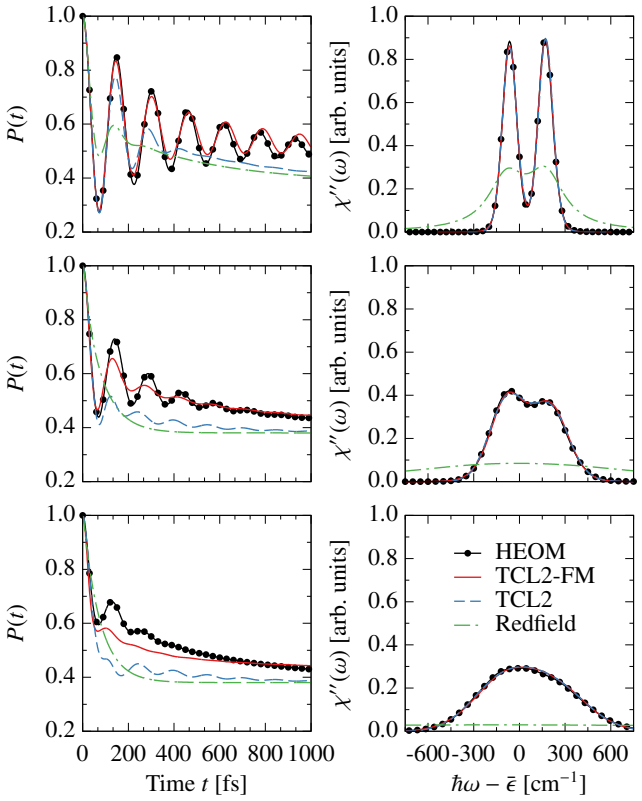

Figure 2.2. Population dynamics of the photo-excited higher-energy chromophore (left column) and linear absorption spectra (right column) with $\lambda = 10\ \mathrm{cm}^{-1}$, $50\ \mathrm{cm}^{-1}$, and $150\ \mathrm{cm}^{-1}$ (top to bottom).

This large discrepancy between two weak-coupling theories (Markovian Redfield theory and non-Markovian TCL2-based theories) is quite surprising given the perturbative nature of both approaches. In the left-hand column panels of Fig. 2.2, we show the population relaxation dynamics generated by the same methods, using the initial condition $\rho(0) = |1\rangle\langle 1|\rho_{\mathrm{b}}^{\mathrm{eq}}$. Clearly, Redfield theory and conventional TCL2 fail in a similar manner as the perturbation becomes large. The TCL2-FM approach now yields results that are quite different than vanilla TCL2, and the former predicts population dynamics that are in good agreement with the numerically exact HEOM results. These observations demonstrate one of our main conclusions: the accuracy of a given dynamical technique depends on the observable. More specifically, TCL2-based approaches are well-suited to the evolution of electronic coherences; we believe that this is because TCL2 reduces to the exact second-cumulant solution for pure-dephasing problems. Population dynamics are significantly less accurate.

The accuracy of TCL2 for linear spectroscopy is nontrivial. For example, it is unrelated to the short-time exactness of perturbative non-Markovian dynamics (compared to Markovian Redfield theory, which is not exact at short time). To demonstrate this fact, we compare TCL2 dynamics with those of the second-order time-convolution master equation (TC2), which has the form

$$\frac{d\rho(t)}{dt} = -\frac{i}{\hbar}[H_{\mathrm{s}}, \rho(t)] - \int_0^t d\tau \mathcal{K}(t-\tau)\rho(\tau), \tag{2.27}$$

and exhibits the same short-time accuracy as TCL2. The results of this comparison are shown in Fig. 2.3. For population dynamics, the two methods exhibit similar accuracy, predicting incorrect population dynamics due to the slow timescale of the bath. However, while TCL2 exhibits nearly exact spectra, the TC2 spectra are extremely poor, even at small reorganization energy.

As a final point on the topic of linear spectroscopy, we emphasize that general quantum master equation techniques, such as TCL2, are capable of using any form of the spectral density. In particular, the accuracy of TCL2 linear response spectra extends beyond the simple Ohmic-Lorentz spectral density employed so far. In Fig. 2.4, we show linear spectra of three dimers with different

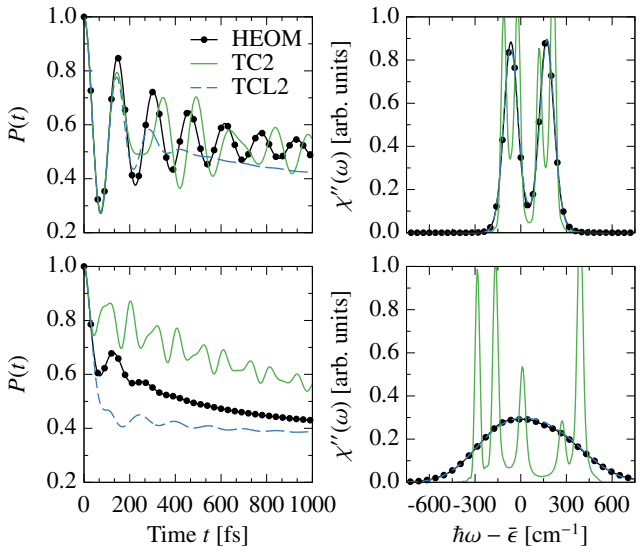

Figure 2.3. The same as in Fig. 2.2, but only for $\lambda = 10$ cm^{-1} (top) and 150 cm^{-1} (bottom), comparing different second-order non-Markovian master equations.

excited-state electronic coupling J_{12}, calculated using TCL2 for the structured spectral density,

$$J(\omega) = \frac{2\lambda\omega_c\omega}{\omega_c^2+\omega^2} + \frac{2\Lambda\Gamma\omega}{(\omega-\Omega_0)^2+\Gamma^2} + \frac{2\Lambda\Gamma\omega}{(\omega+\Omega_0)^2+\Gamma^2}. \tag{2.28}$$

We observe that despite its perturbative nature, TCL2 correctly produces the well-known phonon replica with spacing Ω_0 and additional broadening due to the smooth Ohmic-Lorentzian part of the spectral density.

2.4.3 Third-order nonlinear spectroscopy

Compared to linear response considered above, third-order nonlinear spectroscopy is a more challenging test, due to the simultaneous importance of coherence and population dynamics. As discussed in Sec. 2.2, nonlinear spectroscopy presents an additional complication for non-Markovian quantum master equations in the form of violations to the QRT.

We present two-dimensional electronic spectra, obtained by Fourier transforming over the pump (t_1) and probe (t_3) time delays, resolved by the population waiting time t_2. In particular, we simulate the photon echo spectrum, generated by six terms in the rotating wave approximation

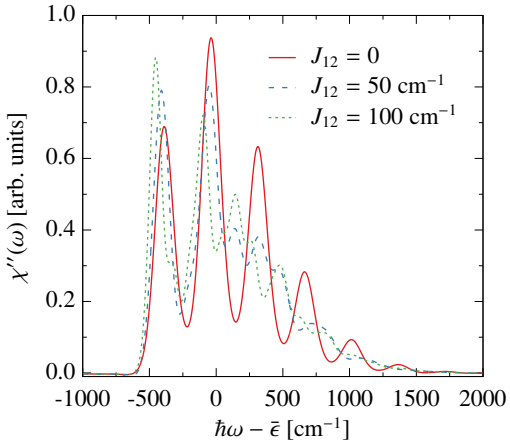

Figure 2.4. Linear spectra of dimers with a structured spectral density consisting of a smooth Ohmic-Lorentz (Debye) part and a high-frequency underdamped mode (see text). For the Debye mode, the parameters are $\omega_c^{-1} = 300$ fs and $\lambda = 50$ cm^{-1}. For the underdamped mode, the parameters are $\Omega_0 = 350$ cm^{-1}, $\Lambda = 500$ cm^{-1} and $\Gamma = 3.5$ cm^{-1}. All spectra are calculated at $T = 77$ K.

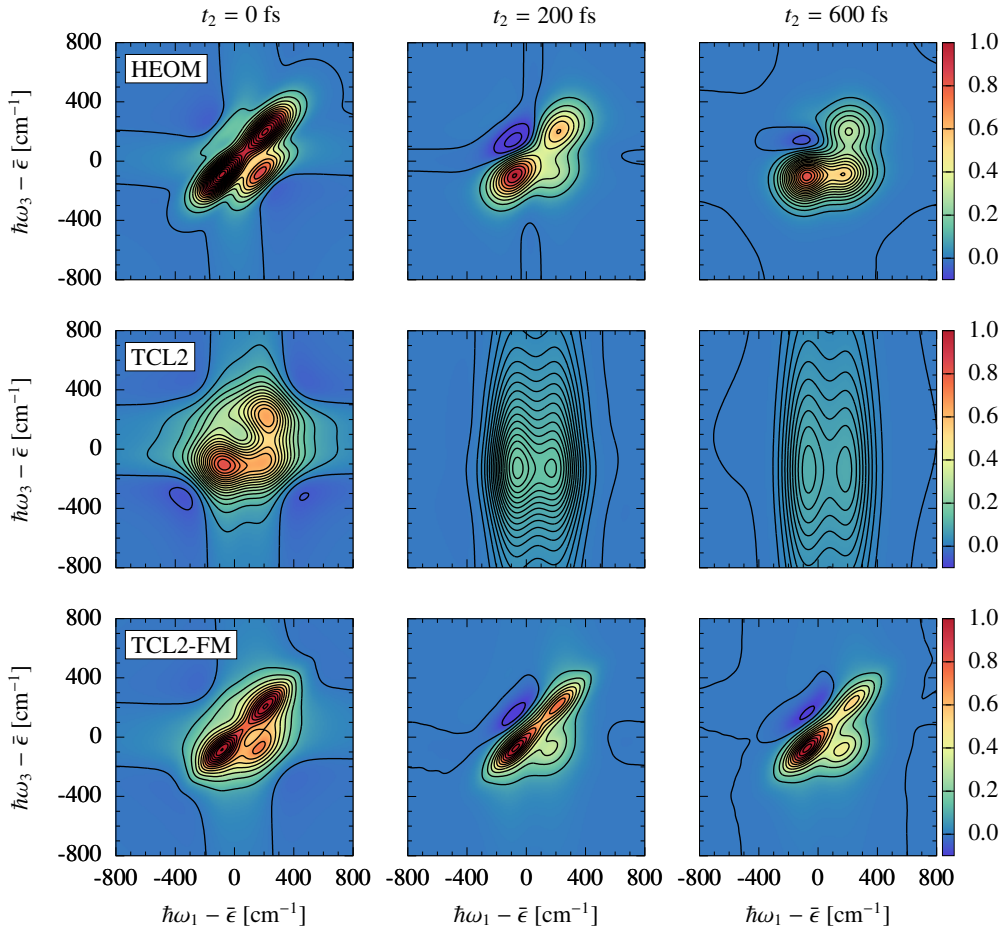

Figure 2.5. Two-dimensional photon echo spectra for a model dimer with $\lambda = 50$ cm^{-1}. Waiting times are shown and increase from left to right. Exact results (top row) are compared with the predictions of TCL2 (middle) and TCL2-FM (bottom row).

associated with rephasing (rp) and non-rephasing (nr) pathways,

$$A(\omega_3, t_2, \omega_1) = \mathrm{Re} \int_0^\infty dt_1 \int_0^\infty dt_3 \Big\{ e^{i(\omega_1 t_1 + \omega_3 t_3)} R_{\mathrm{rp}}(t_3, t_2, t_1) + e^{i(-\omega_1 t_1 + \omega_3 t_3)} R_{\mathrm{nr}}(t_3, t_2, t_1) \Big\}. \tag{2.29}$$

In the above,

$$R_{\mathrm{rp}}(t_3, t_2, t_1) = R_2(t_3, t_2, t_1) + R_3(t_3, t_2, t_1) + R_1^*(t_3, t_2, t_1), \tag{2.30a}$$

$$R_{\mathrm{nr}}(t_3, t_2, t_1) = R_1(t_3, t_2, t_1) + R_4(t_3, t_2, t_1) + R_2^*(t_3, t_2, t_1), \tag{2.30b}$$

and

$$R_1(t_3, t_2, t_1) = \mathrm{Tr}\Big\{ \mu(t_1 + t_2 + t_3) \mu(0) \rho^{\mathrm{eq}} \mu(t_1) \mu(t_1 + t_2) \Big\}, \tag{2.31a}$$

$$R_2(t_3, t_2, t_1) = \mathrm{Tr}\Big\{ \mu(t_1 + t_2 + t_3) \mu(t_1) \rho^{\mathrm{eq}} \mu(0) \mu(t_1 + t_2) \Big\}, \tag{2.31b}$$

$$R_3(t_3, t_2, t_1) = \mathrm{Tr}\Big\{ \mu(t_1 + t_2 + t_3) \mu(t_1 + t_2) \rho^{\mathrm{eq}} \mu(0) \mu(t_1) \Big\}, \tag{2.31c}$$

$$R_4(t_3, t_2, t_1) = \mathrm{Tr}\Big\{ \mu(t_1 + t_2 + t_3) \mu(t_1 + t_2) \mu(t_1) \mu(0) \rho^{\mathrm{eq}} \Big\}. \tag{2.31d}$$

For a moderate reorganization energy of $\lambda = 50$ cm^{-1}, our results are shown in Fig. 2.5 for three values of the waiting time t_2. Although TCL2 dynamics are qualitatively correct at $t_2 = 0$, this accuracy degrades with increasing waiting times. In particular, the spectra become artificially broadened along the ω_3 axis – as discussed in Ref. [74] – and completely fail to describe the four-peak structure and regions of negativity. In contrast, the TCL2-FM two-dimensional spectra are in qualitative agreement with the exact results, reproducing the appropriate peak shapes, spectral features, and timescales. The TCL2-FM results show an unphysical diagonal elongation at long waiting times due to the completely frozen modes that are unable to relax. For the same reasons, the energy transfer (reflected in the redistribution of spectral weight from the high-energy diagonal peak into the off-diagonal peak) is slightly too slow – but much more accurate than the near-

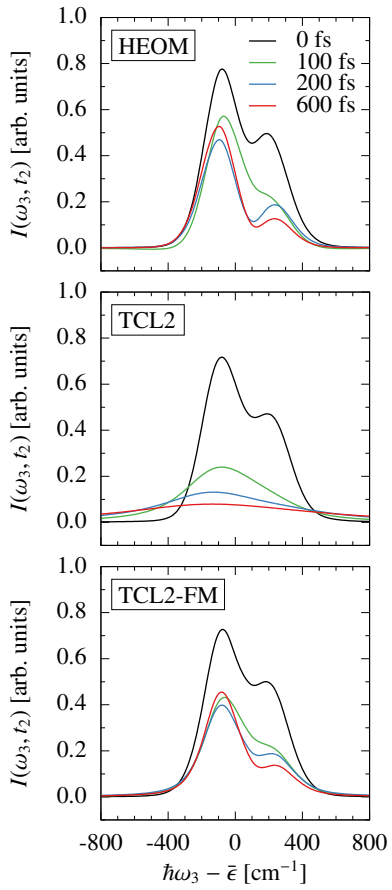

Figure 2.6. Pump-probe spectra $I(\omega_3, t_2)$ obtained from two-dimensional photon echo data presented in Fig. 2.5, via integration over the ω_1 axis. Waiting times t_2 are given in the legend.

immediate transfer predicted by TCL2. We have found that using a smaller splitting frequency (i.e. freezing fewer modes) does improve these aspects of the long-time results at the expense of short-time results. This observations suggests an interesting time-dependent frozen-modes scheme – where modes are successively unfrozen at times longer than their characteristic relaxation time – though we do not pursue this approach here. We conclude that the computationally efficient TCL2-FM approach yields accurate coherence and population dynamics, while mitigating correction terms due to violation of the QRT, leading to qualitatively correct two-dimensional spectra. Although we only show one parameter set for simplicity, we have tested other parameter sets and find that the TCL2-FM accuracy is robust over a wide range of Hamiltonians.

For a simpler representation of the third-order response, we also present the time-resolved

pump-probe spectra, obtained by setting $t_1 = 0$ (or equivalently, integrating over ω_1). We note that the correlation functions contributing to pump-probe spectroscopy are two-point nonequilibrium correlation functions, which should depend sensitively on the accuracy of excited-state population dynamics and exhibit nontrivial corrections to the QRT [61, 62]. For the same parameters as in Fig. 2.5, we present the pump-probe spectra in Fig. 2.6. Consistent with our findings for the full two-dimensional spectra, we see that TCL2 dynamics are accurate at zero waiting time, but completely wrong for nonzero waiting times; the spectra are much too broad and lacking multi-peaked structure. TCL2-FM dynamics cures these deficiencies and predicts accurate pump-probe spectra.

2.5 Conclusions

We have investigated the accuracy of the second-order time-convolutionless (TCL2) quantum master equation for the prediction of linear and third-order time-resolved spectroscopy. We have argued that TCL2 dynamics generalizes the second-cumulant approximation to problems exhibiting excited-state electronic coupling leading to non-adiabatic dynamics and population relaxation. For many contemporary problems concerning the dynamics of multichromophore systems, the bath timescales are too slow to permit classic Markovian theories of lineshapes. For such systems, the TCL2 approach generates nearly-exact linear-response spectra, even though simulations of population dynamics – using the same Hamiltonian parameters – are grossly in error.

In contrast, the TCL2 approximation breaks down away from its perturbative regime when used to simulate nonlinear spectroscopies. We have attributed this failure to two distinct effects: the greater importance of population dynamics and the violation of the quantum regression theorem (QRT). By partitioning microscopic bath degrees of freedom into fast and slow sets, and treating the latter as frozen variables sampled from a thermodynamic ensemble, we have argued that the TCL2-FM approach alleviates both of these problems. Physically, the TCL2-FM formalism treats modes responsible for highly non-Markovian dynamics as a source of inhomogeneous broadening; the resulting Hamiltonian exhibits dynamics which are consequently more Markovian and thus

well-described by weak-coupling, TCL2-type quantum master equations. It will be interesting to implement the second-order corrections to the QRT, in order to assess their relative importance in the prediction of nonlinear spectra. Work along these lines is currently in progress.

Importantly, unlike many reduced quantum dynamics techniques, the formalism of perturbative quantum master equations is not tied to specific forms of the bath Hamiltonian or the system-bath interaction, as long as multi-point equilibrium correlation functions of isolated bath operators can be computed. Nonetheless, the accuracy of such approaches remains to be assessed for more generic Hamiltonians, but the absence of numerically exact results makes this challenging.

Our findings have implications for other quantum dynamics techniques. In particular, we recall that the hierarchical equations of motion (HEOM) reduce to time-convolutionless and time-convolution quantum master equations when the hierarchy is truncated at low order [75, 76]. These low-order HEOM calculations will exhibit the same features described here. For linear spectroscopy, this observation argues strongly for the use of the time-convolutionless closure [75] of the hierarchy, in support of the numerical observations made in Refs. [77, 78]. For nonlinear spectroscopy, low-order approximations will also violate the QRT, and higher levels in the hierarchy will be needed in order to eliminate these (neglected) corrections. Alternatively, the HEOM scheme with a low-order truncation can be combined with the frozen-modes scheme to generate results completely analogous to those shown here for TCL2-FM. For the simple Ohmic-Lorentz spectral density used here, this would require an extra number of Lorentzian modes to represent the fast part of the spectral density; however, for any other spectral density, this decomposition is already required and so would incur no extra overhead.

With regards to computational cost, the TCL2-FM approach is extremely attractive. In its conventional form, presented here, it scales only as MN_{s}^4, where M is a parallel prefactor associated with frozen-mode ensemble sampling and N_{s} is size of the system Hilbert space; this scaling arises from the action of the relaxation tensor on the reduced density matrix. Because the frozen-modes approach leads to more Markovian dynamics, it is tempting to explore a stochastic unraveling of the reduced density matrix [6, 58, 79–81]. This latter approach replaces a single reduced density

matrix simulation by an average over *wavefunction* dynamics with stochastic relaxation events. This procedure would have a scaling of LMN_s^2, where L is a parallel prefactor associated with the stochastic dynamics. We thus anticipate an accurate method which only requires many parallel simulations of system-wavefunction dynamics, each scaling like N_s^2 for generically non-sparse system Hamiltonians; it is hard to imagine a more attractive computational cost with comparable qualitative accuracy over an extremely broad range of Hamiltonian parameters.

Chapter 3: A unification of the Holstein polaron and dynamic disorder pictures of charge transport in organic crystals

The material for this chapter was taken from Reference [82].

3.1 Introduction

Organic semiconductors are a promising class of soft materials with applications in photovoltaics, display technologies and plastic electronics [83–85]. In particular, ultrapure organic molecular crystals (OMCs) provide a rich test bed for the fundamental mechanisms and limitations of charge transport in soft materials [15, 86]. Exceptional room-temperature mobilities in the tens of $cm^2V^{-1}s^{-1}$ have been measured in acene single crystals such as rubrene and pentacene [87–89]. These large mobilities are generally accompanied by an apparently "band-like" power-law temperature dependence, $\mu \propto T^{-\gamma}$ ($\gamma > 0$), suggesting significant carrier delocalization over many unit cells; however controversy still exists over the microscopic mechanisms leading to this behavior, with both experimental and theoretical evidence suggesting an interplay between coherent dynamics, localization, and incoherent hopping [90, 91].

Theoretical efforts to understand electronic dynamics in OMCs has led to the development of several competing and complementary pictures that capture different limiting behaviors. For example, in the limit of weak electron-phonon coupling, Boltzmann transport theory is quite successful [17, 20, 92–94], similar to its use in simple inorganic semiconductors. However, many of the most interesting materials exhibit strong electron-phonon coupling, producing localized electronic states and invalidating the use of Boltzmann transport theory [20]. In actuality, many of the material parameters that govern charge transport in most OMCs – the electronic bandwidth, phonon energy, and electron-phonon coupling strength – exist on energy scales that are comparable to one

another and to $k_{\mathrm{B}}T$, precluding any simple perturbative treatment.

In this state of affairs, two theoretical pictures have emerged, which focus on two distinct forms of electron-phonon coupling. The first picture is that of the Holstein polaron formed by strong local coupling to intramolecular vibrations [18]. In this picture, electronic motion is generally thought of as incoherent, and nuclear tunnelling quantum effects are non-negligible [95–97]. The second picture is that of dynamic disorder or transient localization due to strong nonlocal coupling to intermolecular vibrations [19, 21, 98, 99]. In this case, the delocalized coherent evolution of the electronic wavefunction cannot be neglected, but nuclear quantum effects are considered insignificant. In many real OMCs, both forms of electron-phonon coupling are present. However, the different physical ingredients underlying these two theories prevents their straightforward unification. In this work, we achieve this goal and present a unified nonperturbative approach to calculating dynamical observables in OMCs. Our method reduces to the two powerful theories described above in their respective limits of validity, and gives insight into the relative importance of each energy scale and the crossover from one regime to another. Importantly, we identify a nontrivial behavior in the temperature-dependent transport that can only be explained by the interplay of both forms of electron-phonon coupling, demonstrating that the unified method is more than the sum of its parts. Furthermore, the method is generalizable and computationally affordable, suggesting its straightforward future application to real materials beyond model Hamiltonians.

The layout of this manuscript is as follows. In Sec. 3.2, we describe the Hamiltonian and theoretical and computational tools used to simulate dynamical properties of interest, in particular the conductivity and the spectral function. We further discuss the relation to previous works and the validity of our approximations, referring to an Appendix for a comparison to numerically exact results that we generate. In Sec. 3.3, we present the results of our simulations as a function of temperature, analyzing spectral properties and the temperature dependence of the mobility. Our results are presented at various values of the strength of both types of electron-phonon coupling. Enabled by our unified theory, we identify a mechanism by which an increase in the electron-phonon coupling strength counterintuitively yields a more delocalized wavefunction. In Sec. 3.4,

we summarize our results and discuss future directions.

3.2 Theory

3.2.1 Hamiltonian

We study the spinless Holstein-Peierls model with the Hamiltonian $H = H_{\text{el}} + H_{\text{ph}} + H_{\text{el-ph}}$ with

$$H_{\text{el}} = \sum_{ij} h_{ij} a_i^\dagger a_j, \tag{3.1a}$$

$$H_{\text{ph}} = \sum_i \left(\omega_{\text{H}} b_{i,\text{H}}^\dagger b_{i,\text{H}} + \omega_{\text{P}} b_{i,\text{P}}^\dagger b_{i,\text{P}} \right), \tag{3.1b}$$

$$\begin{aligned} H_{\text{el-ph}} = & \sum_i g_{\text{H}} \omega_{\text{H}} a_i^\dagger a_i X_{i,\text{H}} \\ & + \sum_{\langle ij \rangle} g_{\text{P}} \omega_{\text{P}} (a_i^\dagger a_j + a_j^\dagger a_i)(X_{i,\text{P}} - X_{j,\text{P}}), \end{aligned} \tag{3.1c}$$

where $a_i^\dagger$ (a_i) and $b_i^\dagger$ (b_i) are the creation (annihilation) operators on lattice site i for electrons and phonons, and $\langle ij \rangle$ indicates nearest neighbors. Here and throughout, we use $\hbar = 1$ for notational simplicity, but all results will be given with proper physical units. In Eq. (3.1a), h_{ij} are one-electron Hamiltonian matrix elements. Due to particle-hole symmetry our analysis applies equally to electron and hole doping. Although our ensuing formalism can be applied to an arbitrary electronic Hamiltonian, here we will study a nearest-neighbor tight-binding model with $h_{ij} = -\tau$ for i and j nearest neighbors and zero otherwise. This model represents one molecular orbital per lattice site and we consider two vibrational modes on each site with frequencies ω_{H} and ω_{P}. The first is a high-frequency intramolecular vibration whose dimensionless displacement $X_{i,\text{H}} \equiv (b_{i,\text{H}}^\dagger + b_{i,\text{H}})$ couples to the on-site electron density via the Holstein mechanism with dimensionless strength g_{H}. The second is a low-frequency lattice mode corresponding to the position of the molecule in the unit cell; the difference in displacements of neighboring molecules, $(X_{i,\text{P}} - X_{j,\text{P}})$, couples to the kinetic energy via the the Peierls (or Su-Schrieffer-Heeger [100]) mechanism with dimensionless

strength g_{P}. These two electron-phonon coupling mechanisms are commonly referred to as being local and nonlocal, respectively.

The Hamiltonian parameters relevant for molecular organic crystals presents a challenge to theoretical analysis. For example, the parameters we will use in this work, based on *ab initio* simulations of hole transport in rubrene, are $\tau = 100$ meV, $\omega_{\mathrm{H}} = 150$ meV, and $\omega_{\mathrm{P}} = 6$ meV [22, 23, 101, 102]. These exemplify the typical behavior $\omega_{\mathrm{H}}/\tau > 1$ and $\omega_{\mathrm{P}}/\tau < 1$, i.e. the intramolecular dynamics occur on timescale that is faster than the electronic dynamics and the intermolecular vibrational dynamics occur on a timescale that is slower than the electronic dynamics. Furthermore, the dimensionless electron-phonon coupling strengths g_{H} and g_{P} are both on the order of 1 and the temperature ranges from 1 to 40 meV. Collectively, these parameters preclude an obvious perturbative treatment of the combined electron-phonon interactions. In the remainder of this section, we will discuss our nonperturbative approach to simulating the dynamics of this Hamiltonian with the knowledge that the Holstein and Peierls components describe fundamentally different physical processes.

3.2.2 Conductivity and mobility

Our principle object of interest is the temperature-dependent AC conductivity $\sigma(\omega)$, which is obtained from the current autocorrelation function,

$$\mathrm{Re}\sigma(\omega) = \frac{1 - e^{-\beta\omega}}{2L\omega} \int_{-\infty}^{+\infty} dt\; e^{i\omega t} C_{JJ}(t), \tag{3.2a}$$

$$C_{JJ}(t) = \mathrm{Tr}[J(t)J(0)e^{-\beta H}]/Z, \tag{3.2b}$$

where $Z = \mathrm{Tr}e^{-\beta H}$ is the partition function, $\beta = 1/kT$, and L is the number of lattice sites. Although in general, the conductivity is a tensor quantity with respect to the lattice vectors, for the sake of simplicity we will focus on the one-dimensional case; the method can be applied to lattices of higher dimensionality and will exhibit identical scaling with respect to number of lattice sites. The DC conductivity, $\sigma_{\mathrm{DC}} \equiv \sigma(\omega \to 0)$, in the low-carrier-density limit, gives access to

the mobility via $\mu = \sigma_{\mathrm{DC}}/ne_0$, where $n = N/L$ is the number density of carriers and e_0 is the fundamental electric charge. The current operator is

$$J = -ia \sum_{\langle ij \rangle} (a_i^\dagger a_j - a_j^\dagger a_i)[-\tau + g_{\mathrm{P}}\omega_{\mathrm{P}}(X_{i,\mathrm{P}} - X_{j,\mathrm{P}})] \equiv \sum_{ij} J_{ij} a_i^\dagger a_j \tag{3.3}$$

and a is the lattice constant and J_{ij} is an operator in the Peierls phonons subspace. We work on a 1D lattice with periodic boundary conditions in the canonical ensemble with $N = 1$ electron, which is appropriate for the low density limit achievable in most semiconductors through doping or photoexcitation.

We treat the Peierls phonons quasi-classically, which is justified based on their relatively low frequency. Although approximate, this treatment is nonperturbative in g_{P}. Under this approximation, the Peierls phonon displacements are scalar variables that obey classical equations of motion

$$X_{i,\mathrm{P}}(t) = X_{i,\mathrm{P}}(0)\cos(\omega_{\mathrm{P}}t) + P_{i,\mathrm{P}}(0)\sin(\omega_{\mathrm{P}}t) \tag{3.4}$$

with local Hamiltonian $H_{i,\mathrm{P}} = (\omega_{\mathrm{P}}/4)\left[P_{i,\mathrm{P}}^2 + X_{i,\mathrm{P}}^2\right]$. This leads to a Holstein Hamiltonian with time-dependent electronic matrix elements,

$$\begin{aligned} H_{\mathrm{H}}(t) = \sum_{\langle ij \rangle} \Big[& \tau_{ij}(t)\left(a_i^\dagger a_j + a_j^\dagger a_i\right) + \omega_{\mathrm{H}} b_{i,\mathrm{H}}^\dagger b_{i,\mathrm{H}} \\ & + g_{\mathrm{H}}\omega_{\mathrm{H}} a_i^\dagger a_i X_{i,\mathrm{H}} \Big], \end{aligned} \tag{3.5}$$

and a time-dependent current operator

$$J(t) = -ia \sum_{\langle ij \rangle} \tau_{ij}(t)(a_i^\dagger a_j - a_j^\dagger a_i) \equiv \sum_{ij} J_{ij}(t) a_i^\dagger a_j \tag{3.6}$$

where

$$\tau_{ij}(t) = -\tau + g_{\mathrm{P}}\omega_{\mathrm{P}}\left[X_i(t) - X_j(t)\right]. \tag{3.7}$$

The current autocorrelation function is now approximately given by

$$C_{JJ}(t) = \int d\mathbf{X}_\mathrm{P} \int d\mathbf{P}_\mathrm{P}\, \mathcal{P}(\mathbf{X}_\mathrm{P}, \mathbf{P}_\mathrm{P}) \times \mathrm{Tr}\left[U_\mathrm{H}(0,t)J(t)U_\mathrm{H}(t,0)Je^{-\beta H_\mathrm{H}(0)}\right]/Z_\mathrm{H} \tag{3.8}$$

where $\mathcal{P}(\mathbf{X}_\mathrm{P}, \mathbf{P}_\mathrm{P})$ is the phase-space distribution of the classical Peierls variables, $Z_\mathrm{H} = \mathrm{Tr}_\mathrm{H}\, e^{-\beta H_\mathrm{H}(0)}$, and $U_\mathrm{H}(t,0)$ is the time-ordered evolution operator,

$$U_\mathrm{H}(t,0) = T\exp\left[-i\int_0^t dt' H_\mathrm{H}(t')\right]. \tag{3.9}$$

In order to approximately respect quantum statistics at low temperature, especially zero-point motion, the phase-space distribution $\mathcal{P}$ is a product of Gaussian Wigner distributions with $\langle X_{i,\mathrm{P}}^2\rangle = \tanh(\beta\omega_\mathrm{P}/2)$ and $\langle P_{i,\mathrm{P}}^2\rangle = 1/[\tanh(\beta\omega_\mathrm{P}/2)]$. The integral is then evaluated by Monte Carlo sampling of $\mathbf{X}_\mathrm{P}$ and $\mathbf{P}_\mathrm{P}$, and these variables are then evolve in time according to classical dynamics.

To treat the Holstein electron-phonon coupling, we use the Lang-Firsov polaron transformation [103], defined for operators O as $\tilde{O} \equiv e^S O e^{-S}$ with

$$S = g_\mathrm{H}\sum_i a_i^\dagger a_i (b_{i,\mathrm{H}}^\dagger - b_{i,\mathrm{H}}). \tag{3.10}$$

Applying the transformation to $H_\mathrm{H}(t)$ and $J(t)$ gives

$$\tilde{H}_\mathrm{H}(t) = \sum_{ij}\tau_{ij}(t)e^{C_i}e^{-C_j}a_i^\dagger a_j + \sum_i\left[\Sigma_\mathrm{H}a_i^\dagger a_i + \omega_\mathrm{H}b_{i,\mathrm{H}}^\dagger b_{i,\mathrm{H}}\right] \tag{3.11}$$

$$\tilde{J}(t) = \sum_{ij}J_{ij}(t)a_i^\dagger a_j e^{C_i}e^{-C_j} \tag{3.12}$$

where $C_i = g_\mathrm{H}\left(b_{i,\mathrm{H}}^\dagger - b_{i,\mathrm{H}}\right)$ and $\Sigma_\mathrm{H} = -g_\mathrm{H}^2\omega_\mathrm{H}$ is the polaron self-energy. We now realize a separable, finite-temperature mean-field Hamiltonian by replacing the phonon operator $e^{C_i}e^{-C_j}$ by

its thermal average,

$$\begin{aligned} e^{C_i} e^{-C_j} &\approx \mathrm{Tr}_{\mathrm{ph}} \left[e^{C_i} e^{-C_j} e^{-\beta H_{\mathrm{ph}}} \right] / Z_{\mathrm{ph}} \\ &= \exp \left[-g_{\mathrm{H}}^2 \coth(\beta\omega/2)(1 - \delta_{ij}) \right], \end{aligned} \tag{3.13}$$

where $Z_{\mathrm{ph}} = \mathrm{Tr}_{\mathrm{ph}} e^{-\beta H_{\mathrm{ph}}}$ is the partition function of the free (high-frequency) phonons. This approximation assumes that the Holstein phonons equilibrate much faster than the electrons, which is reasonable because of their high frequency $\omega_{\mathrm{H}} > \tau$. We do not make any approximation in the polaronic treatment of $\tilde{J}$.

Combining the above procedures, the total Hamiltonian has now been approximated as a sum of separable and quadratic electron and phonon terms, where the electronic Hamiltonian $\tilde{h}(t)$ is time- and temperature-dependent,

$$\tilde{h}(t) = \sum_{\langle ij \rangle} \tilde{\tau}_{ij}(t) a_i^\dagger a_j, \tag{3.14}$$

with the evolution operator

$$\tilde{u}(t, 0) = T \exp \left[-i \int_0^t dt' \tilde{h}(t') \right]. \tag{3.15}$$

The transfer integral is given by

$$\tilde{\tau}_{ij}(t) = \left\{ -\tau + g_{\mathrm{P}} \omega_{\mathrm{P}} \left[X_i(t) - X_j(t) \right] \right\} \exp \left[-g_{\mathrm{H}}^2 \coth(\beta\omega_{\mathrm{H}}/2) \right] \tag{3.16}$$

and reflects Peierls-induced dynamic disorder and Holstein-induced band narrowing. Finally, the correlation function becomes

$$C_{JJ}(t) = \sum_{ijkl} J_{ijkl}(t) F_{ijkl}(t) \tag{3.17}$$

where $J_{ijkl}(t)$ and $F_{ijkl}(t)$ are purely electronic and phononic correlation functions,

$$\begin{aligned} J_{ijkl}(t) = \int d\mathbf{X}_\mathrm{P} \int d\mathbf{P}_\mathrm{P}\, \mathcal{P}(\mathbf{X}_\mathrm{P}, \mathbf{P}_\mathrm{P}) J_{ij}(t) J_{kl}(0) \\ \times \mathrm{Tr}_\mathrm{el} \left[\tilde{u}(0,t) a_i^\dagger a_j \tilde{u}(t,0) a_k^\dagger a_l e^{-\beta \tilde{h}(0)} \right] / Z_\mathrm{el} \end{aligned} \tag{3.18}$$

and

$$\begin{aligned} F_{ijkl}(t) &= \mathrm{Tr}_\mathrm{ph} \left[e^{C_i(t)} e^{-C_j(t)} e^{C_k} e^{-C_l} e^{\beta H_\mathrm{ph}} \right] / Z_\mathrm{ph} \\ &= \exp\left[-\tfrac{1}{2} \Phi_{ijij}(0) \right] \exp\left[-\tfrac{1}{2} \Phi_{klkl}(0) \right] \\ &\quad \times \exp\left[-\Phi_{ijkl}(t) \right], \end{aligned} \tag{3.19}$$

where $Z_\mathrm{el} = \mathrm{Tr}_\mathrm{el} e^{-\beta \tilde{h}(0)}$,

$$\Phi_{ijkl}(t) = \Phi(t) [\delta_{ik} - \delta_{jk} - \delta_{il} + \delta_{jl}], \tag{3.20a}$$

$$\Phi(t) = g_\mathrm{H}^2 [\coth(\beta \omega_\mathrm{H}/2) \cos(\omega_\mathrm{H} t) - i \sin(\omega_\mathrm{H} t)]. \tag{3.20b}$$

The time dependence of $F_{ijkl}(t)$ is responsible for incoherent electron-phonon scattering and suggests a separation into static coherent and dynamical incoherent contributions [104, 105], $F(t) = F^\mathrm{coh} + F^\mathrm{inc}(t)$, with

$$F_{ijkl}^\mathrm{coh} = \exp\left[-\tfrac{1}{2} \Phi_{ijij}(0) - \tfrac{1}{2} \Phi_{klkl}(0) \right], \tag{3.21a}$$

$$F_{ijkl}^\mathrm{inc}(t) = F_{ijkl}^\mathrm{coh} \left\{ \exp\left[-\Phi_{ijkl}(t) \right] - 1 \right\}. \tag{3.21b}$$

Retaining only F^coh produces a theory of dynamically disordered transport with Holstein-induced band narrowing of the matrix elements in both the Hamiltonian and the current operator.

We have implemented an algorithm for Eq. (3.18) based on the time evolution of single-particle eigenstates which, for a general electronic Hamiltonian, scales as $L^5 N_t$ per trajectory where L is the number of lattice sites and N_t is the number of timesteps. If the electronic Hamiltonian has

only finite-range interactions, such as the nearest-neighbor interaction used here, then the scaling is reduced to $L^3 N_t$. Finally, if the incoherent phonon term is neglected, the nearest-neighbor case has a scaling of $L^2 N_t$, which is the typical cost of the nearest-neighbor semiclassical dynamic disorder approach at finite temperature: there are L single-particle eigenstates and each eigenstate trajectory has a cost that is proportional to L [106].

3.2.3 One-particle spectral function

The above approach can be straightforwardly extended to many other correlation functions. In particular, we will also present results for the inverse photoemission spectrum of the undoped parent semiconductor corresponding to a measurement of the conduction band's many-body density of states. [17] This is calculated via the electron addition Green's function of the model with $N = 0$ electrons,

$$iG^{\mathrm{R}}_{ij}(t) = \mathrm{Tr}_{(N=0)}\left[a_i(t)a^{\dagger}_j e^{-\beta H}\right]/Z, \tag{3.22}$$

using the same approximations introduced above. From this, we calculate the momentum-resolved spectral function

$$A(k,\omega) = -\frac{1}{L\pi}\sum_{ij} e^{ika(i-j)}\mathrm{Im}\int_0^{\infty} dt e^{i\omega t} G^{\mathrm{R}}_{ij}(t) \tag{3.23}$$

and the density of states $\rho(\omega) = L^{-1}\sum_k A(k,\omega)$.

3.2.4 Limiting behaviors and relation to previous works

In the limit $g_{\mathrm{P}} = 0$, i.e. without Peierls electron-phonon coupling, our approach reduces to that presented by Ortmann et al. [104] In this limit, the Hamiltonian has no time dependence and the dynamics can be re-written exactly in terms of eigenstates of $\tilde{h}$. At low temperature, this approach reduces to Boltzmann transport theory with a constant scattering time t_{s} and band-narrowed transfer integral $\tilde{\tau}$ [107]. The theory also reproduces the narrow-band and Marcus-Levich mobility in the limit of large polaron binding energy (large g_{H} or ω_{H}), and ultimately Marcus theory in the limit of large polaron binding energy and high T [108]. A major distinguishing feature of

our approach, in comparison to previous studies that have combined Holstein polaron approach with dynamic disorder [97], is that we make no narrow-band approximation, which means that we recover the exact unitary electronic dynamics in the absence of Holstein coupling.

In the limit that $g_{\mathrm{H}} = 0$, i.e. without Holstein electron-phonon coupling, this approach is analogous to the "dynamic disorder" picture of Troisi and co-workers [19] or the transient localization scenario of Ciuchi, Fratini and Mayou [21, 99]. In previous work [19, 98, 101, 109], the evolution operator Eq. (4.16) is used to propagate a localized electronic state and the mean squared displacement (MSD) is calculated; in the long-time limit, the slope of the MSD is used to determine the diffusion coefficient and the electron mobility. This approach commonly includes feedback of the electronic system on the classical phonons at a mean-field level (Ehrenfest dynamics). We neglect this force, resulting in the analytical solution for the phonon dynamics in Eq. (3.4). We have tested the role of feedback in calculations of the MSD. In the regimes studied here, feedback modifies the mobility by around 10% at most, in qualitative agreement with previous studies [98].

Ignoring this back-reaction, our Kubo approach has three advantages. First, quasiclassical dynamics deteriorates in the long-time limit, approaching a behavior that is similar to that at infinite temperature [21, 110]. Compared to the MSD, the current autocorrelation function is less sensitive to the long-time dynamics because it decays to zero. Second, our approach naturally gives access to the full frequency-resolved conductivity rather than just the DC conductivity (the mobility). Third, the incorporation of a fully quantum Holstein electron-phonon interaction and its treatment by a similarity transformation is natural for the correlation function but much harder for the wavefunction dynamics.

Although a number of previous theoretical works have studied simultaneous Holstein-Peierls coupling [101, 111, 112], they typically treat both couplings with the same approximate method. We emphasize that the use of two different methods in our approach is motivated by the different frequency scales of the phonons, and not strictly on the form of the coupling (Holstein or Peierls); it happens to be the case that in most OMCs, the important Holstein coupling is to high-frequency vibrations and the important Peierls coupling is to low-frequency vibrations. We note that pre-

vious work on OMCs that have also recognized this frequency disparity have generally involved additional approximations such as static low-frequency phonons [113, 114] or a zero-bandwidth perturbative treatment of high-frequency phonons [97].

3.2.5 Discussion of approximations

The accuracy of our approach ultimately relies on a separation of timescales between the two types of phonons and the electronic system. A semiclassical treatment of low-frequency Peierls modes in molecular crystals has been shown to be well-justified and highly accurate [21, 115]. The ratio of energy scales, $\omega_{\mathrm{P}}/\tau = 0.06$, indicates a strongly adiabatic regime, while the temperature $k_{\mathrm{B}}T \gg \omega_{\mathrm{P}}$ in typical experimental conditions further justifies the use of classical phonons.

With respect to the Holstein modes, while the criterion of $\omega_{\mathrm{H}}/\tau > 1$ is satisfied, this ratio (1.5 in our case) indicates that the system is only weakly anti-adiabatic, which would limit the accuracy of our approach; many OMCs will have a smaller bandwidth than considered here, and thus $\omega_{\mathrm{H}}/\tau \gg 1$ may be more strongly satisfied. To the best of our knowledge, no systematic and detailed study has been performed that compares the Lang-Firsov approach to numerically exact results for the Holstein model in this regime. Therefore, in the Appendix, we give a detailed analysis of the accuracy of the Lang-Firsov treatment compared to numerically exact calculations obtained via exact diagonalization over the variational Hilbert space (EDVHS) [116, 117]. The comparison is performed at zero temperature, which is useful to assess accuracy even at finite temperatures, since $\omega_{\mathrm{H}} \gg k_{\mathrm{B}}T$ for the temperature range of interest. We find that despite application to a challenging parameter regime, the approximate Lang-Firsov approach captures the essential physical effects of the Holstein polaron in the form of coherent band-narrowing and the incoherent electron-phonon interaction, although the spectral structure at high energies is only qualitatively correct. Nevertheless, the accuracy of the Lang-Firsov approach holds in the limits of both weak and strong electron-phonon coupling, demonstrating its nonperturbative nature. Crucially, the physics enabled by our approach go beyond those of perturbation theory and the common narrow-band approximation.

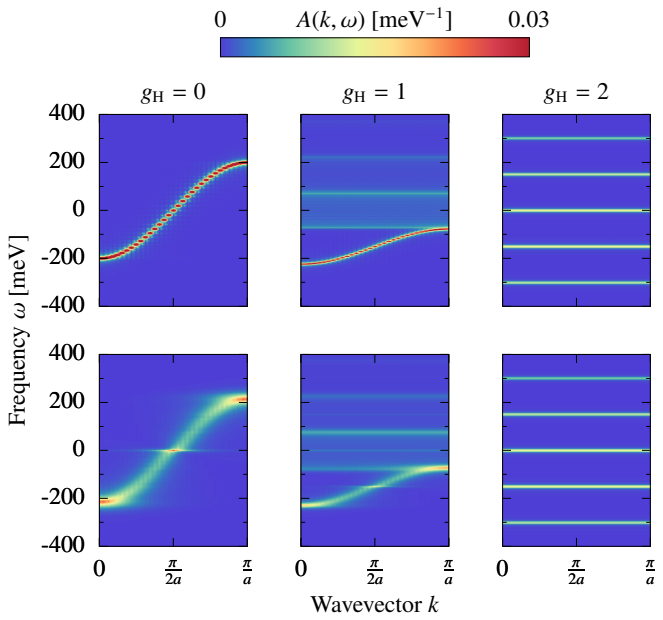

Figure 3.1. Momentum-resolved spectral function $A(k,\omega)$ at $T = 300$ K with no dynamic disorder (top row) and strong dynamic disorder ($g_P = 2$, bottom row) at different values of Holstein coupling g_H. Calculated with electronic transfer integral $\tau = 100$ meV, phonon frequencies $\omega_P = 6$ meV and $\omega_H = 150$ meV, and a Lorentzian broadening with $\eta = 2.5$ meV.

Validation of the unified scheme presented here is of course challenging because numerically exact treatments of the Hamiltonian we consider are unavailable. However, the idea of combining a classical treatment of low-frequency modes with an exact or perturbative quantum treatment of high-frequency modes has been successful in the past in studies of the nonadiabatic dynamics of few-level systems coupled to harmonic oscillator baths, for which numerically exact results are available [31, 65, 69, 118–121]. These previous works partially inspired the approach taken here for extended systems and give us confidence to expect semiquantitative accuracy at an affordable computational cost.

3.3 Results

3.3.1 Simulation Details

Numerical simulations were performed for a 1D periodic lattice with $L = 64$ sites for the full theory and $L = 128$ sites for the pure Holstein polaron and Peierls theories, which testing confirms is sufficient for convergence with respect to system size. Phonons frequencies are $\omega_P = 6$

meV and $\omega_{\mathrm{H}} = 150$ meV and the electronic nearest-neighbor transfer integral is $\tau = 100$ meV. These parameters were chosen to simulate the high-mobility crystallographic axis of an anisotropic organic single crystal such as rubrene or pentacene, particularly when using a coupling strength of $g_{\mathrm{H}} = 1$ and $g_{\mathrm{P}} = 1 - 2$ [22, 23, 101, 102]. In keeping with this, we also use the lattice constant for the b-axis of rubrene, 7.2 Å. In addition to being representative of OMCs, these parameters satisfy the conditions necessary to ensure the accuracy of the method presented in this work, $\omega_{\mathrm{H}} > \tau > \omega_{\mathrm{P}}$, as discussed above. Numerical propagation was performed using the fourth-order Runge-Kutta algorithm with a timestep set to be a factor of ten smaller than the shortest timescale in the problem, $dt = 0.1^{*} \min(\hbar/(4\tilde{\tau}),\ 1/\omega_{\mathrm{H}})$, which in practice varies between 0.05 and 0.4 fs. For DC transport properties, to ensure convergence at zero frequency in a finite system, we apply a Gaussian damping to the correlation functions, simulating a weak dispersionless Drude scatterer such as neutral impurity [107]. We use a scattering time of $\hbar/t_{\mathrm{s}} = 0.25$ meV, which is smaller than any energy scale of the problem by more than an order of magnitude. The choice of t_{s} affects the absolute magnitude of the mobility in cases where the current autocorrelation does not decay to zero naturally (when T or g_{P} is small or g_{H} is large), but our choice has no effect on the overall temperature dependence above about 100 K. While the spectrally-resolved quantities are obtained from the same calculation, we instead apply an exponential damping in time corresponding to a Lorentzian broadening in energy with half-width at half maximum $\eta = 2.5$ meV to produce smooth spectra. Convergence with respect to the ensemble sampling of the classical Peierls modes required averaging of up to $10,000$ trajectories.

3.3.2 Spectral functions

Before exploring transport, it is informative to look at the one-particle spectral properties of the Holstein-Peierls Hamiltonian within our approach, as described in Sec. 3.2.3. In Fig. 3.1, we show the momentum-resolved spectral function $A(k, \omega)$ at 300 K, with and without Peierls dynamic disorder and with various Holstein coupling values. In the absence of any electron-phonon coupling (top left), the spectral function has sharp quasiparticle peaks following the expected noninteracting

dispersion relation $E(k) = -2\tau\cos(ka)$. When moderate Holstein coupling is added (top center), we see a mixture of coherent and incoherent features in the spectral function. The zero-phonon transition is shifted by the self-energy $\Sigma_{\mathrm{H}} = -g_{\mathrm{H}}^2\omega_{\mathrm{H}}$ and has a dispersion whose bandwidth is narrowed to $4\tilde{\tau}$. Furthermore, satellite peaks now appear with a spacing of ω_{H}, as seen in previous results [122–124]. With strong Holstein coupling (top right), the renormalized electronic bandwidth is very small, leading to a dispersionless vibronic progression with a spacing of ω_{H} and intensities determined by g_{H} and T.

In the case with Peierls coupling only (lower left), we see a broadened version of the purely electronic band structure, but with an anomalous peak at the band center. This peak arises in models with purely off-diagonal disorder [125] and has been shown to disappear with the addition of infinitesimal diagonal disorder [126, 127]. Although the peaks acquire a linewidth, the quasiparticle picture is maintained. Dynamic disorder also yields states outside of the undisordered band and the onset of the band edge is softened. We recall that in the static (Anderson localization) limit, all states are localized in one dimension; however the localization lengths of states near the band edge are much smaller than those in the band center [20]. We will return to this point in Sec. 3.3.4 when we analyze our mobility results in terms of localization properties.

For the case of simultaneous Peierls and moderate Holstein coupling (bottom center), we see that the dispersion and satellite structure largely depend on the Holstein coupling g_{H}, whereas the Peierls dynamic disorder contributes a broadening in frequency and momentum (as well as the spurious peak at the band center, which is now present in the phonon replica structures). These effects of dynamic disorder become less pronounced as the band narrows, and in the case with renormalized bandwidth approaching zero (bottom right), the Peierls disorder has no discernible effect.

3.3.3 Optical conductivity

We now turn our attention to the primary focus of this work, the conductivity. In Fig. 3.2 we present the AC conductivity at different temperatures for the pure Holstein model ($g_{\mathrm{P}} = 0$,

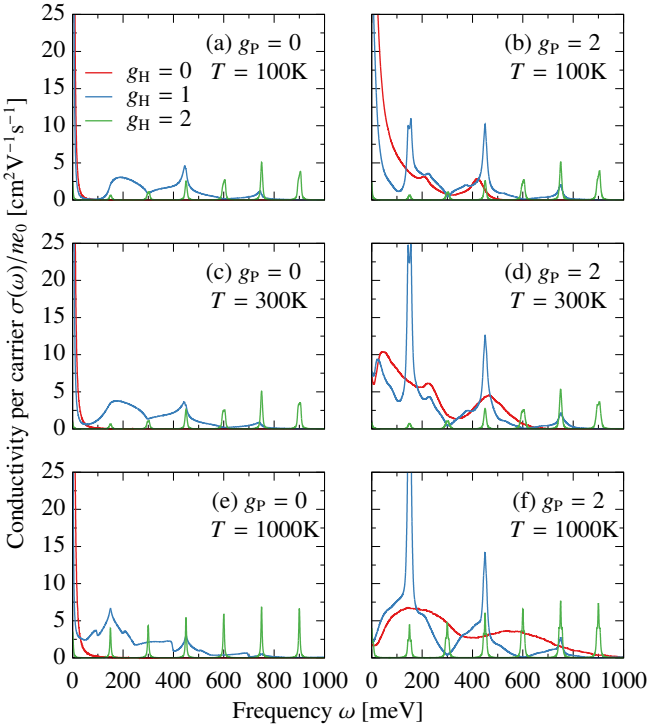

Figure 3.2. The per-carrier optical conductivity of the Holstein-Peierls model at different temperatures T = 100, 300 and 1000 K. Results are shown for the Holstein-only case with $g_P = 0$ ((a), (c) and (e)), and strong dynamic disorder similar to that of high-mobility OMCs, $g_P = 2$ ((b), (d) and (f)). All other parameters are the same as in Fig. 3.1. Note that in panels (a), (b), (c), and (e), the zero-frequency conductivity is too large to show on the same scale as the other spectral features. See Fig. 3.3 for details of the zero-frequency conductivity.

left column) and for the full Holstein-Peierls model with strong dynamic disorder ($g_P = 2$, right column). For the pure Holstein model, due to the aforementioned condition $\omega_H \gg k_B T$, we see little qualitative difference between the $T = 100$ K and $T = 300$ K cases, Fig. 3.2(a) and (c), and indeed little difference from the zero-temperature result in Fig. 3.7(a). In order to see qualitative changes in the pure Holstein optical conductivity, we need to go to much higher temperatures ($T = 1000$ K), at which point the phonon peaks associated with the incoherent terms in Eq. (3.21b) become more pronounced; although these temperatures are unrealistic for OMCs, this behavior may be observable in other classes of soft semiconductors with different energy scales.

The full Holstein-Peierls model shows significantly different behavior. As also seen in the one-particle spectral function, spectra with strong Holstein coupling ($g_H = 2$, green curves) are largely

unaffected by Peierls disorder. The only qualitative change is the appearance of weak side peaks at $\pm\omega_{\mathrm{P}}$ at $T = 1000$ K. In all cases with $g_{\mathrm{H}} = 1$ (blue curves), the addition of dynamic disorder significantly broadens and suppresses the zero-frequency peak, while shifting weight toward finite frequency peaks, particularly enhancing those located at odd multiples of ω_{H}. The absence of even-numbered peaks is a coincidental destructive interference effect, because these phonon frequencies coincide with odd multiples of τ. In the presence of dynamic disorder with no Holstein coupling (red curves in Fig. 3.2(b), (d) and (f)), structure is observed at $\omega = 2\tau$ and 4τ, while the $\omega = 0$ peak is suppressed, in agreement with previous studies [128].

Summarizing our results on the finite-temperture AC conductivity of the Holstein-Peierls Hamiltonian, the low-frequency features, which determine transport, are most strongly affected by Peierls-induced dynamic disorder and are virtually unaffected by the presence of moderate Holstein coupling. However, the Holstein coupling significantly modifies the high-frequency structure, which can be probed spectroscopically.

3.3.4 DC mobility

We now turn to a study of the DC mobility, which is the observable of greatest practical interest for device performance, presented in Fig. 3.3. First, we recall the single-carrier ($N = 1$) mobility in the absence of any electron-phonon coupling, corresponding to the Boltzmann transport equation [17, 104, 107]

$$\mu_{\mathrm{el}} = \frac{\sqrt{\pi} t_{\mathrm{s}}}{e_0 k_B T Z_{\mathrm{el}}} \mathrm{Tr}\left\{J^2 e^{-\beta h}\right\} = \frac{\sqrt{\pi} e_0 t_{\mathrm{s}}}{k_{\mathrm{B}} T Z_{\mathrm{el}}} \sum_k v_k^2 e^{-\varepsilon(k)/k_{\mathrm{B}}T}, \tag{3.24}$$

where t_{s} is a Drude scattering time and $v_k = \nabla_k \varepsilon(k)$. At low temperatures over which the band is effectively parabolic, a single electron in the canonical ensemble obeys ideal statistics $\langle v^2 \rangle = k_{\mathrm{B}}T/m^*$, producing a constant value

$$\mu_{\mathrm{el}}(T \ll \tau) = \frac{\sqrt{\pi} e_0 t_{\mathrm{s}}}{m^*} = 2\sqrt{\pi} e_0 a^2 t_{\mathrm{s}} \tau, \tag{3.25}$$

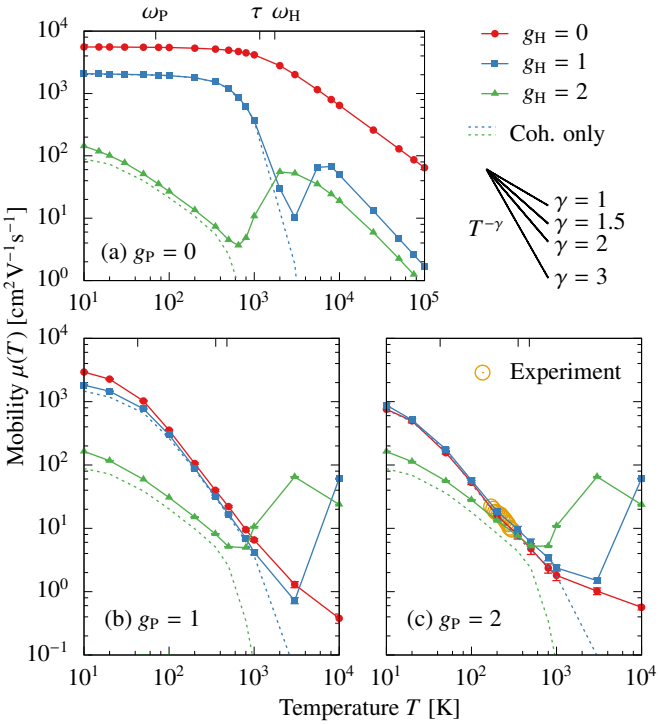

Figure 3.3. DC (zero-frequency) mobility with zero ($g_P = 0$, (a)) Peierls coupling, moderate Peierls coupling ($g_P = 1$, (b)), and strong Peierls coupling ($g_P = 2$, (c)) and various Holstein coupling. The top axis marks the major energies scales of the model, i.e. Peierls frequency ω_P, Holstein frequency ω_H, and the bare nearest-neighbor hopping τ. The dashed lines show the coherent component of the mobility, where the Holstein coupling is only evident through the renormalized electronic energy $\tilde{\tau}$. Panel (c) compares to rubrene b-axis Hall effect hole mobility measurements from Ref. [88]. A Gaussian broadening of 0.25 meV was used in all calculations to converge the conductivity at zero frequency; all other parameters are the same as in Fig. 3.1. Below the key on the top right, we plot idealized power laws $T^{-\gamma}$ for visual reference.

which is the Drude mobility. At high temperatures, $k_B T \gg \tau$, the average over the finite bandwidth is constant, $\langle J^2 \rangle \approx 4\pi e_0^2 \tau^2 a^2$, giving

$$\mu_{el}(T \gg \tau) = 4\pi^{3/2} e_0 a^2 t_s \frac{\tau^2}{k_B T}, \tag{3.26}$$

i.e. decaying like T^{-1}. The crossover between these two behaviors clearly occurs at $k_B T \approx \tau$, as can be seen in Fig. 3.3(a), with $g_H, g_P = 0$ (red data).

With the addition of Holstein coupling, our theory of the mobility reduces to that of Ortmann et al. [104] and our analysis is correspondingly similar. The coherent contribution to the mobility has the same form as above, but with the temperature-dependent renormalized $\tilde{\tau}(T)$. Thus the low-

temperature constant value is reduced by a factor of $e^{-g_H^2}$, the crossover temperature is reduced, and the high-temperature decay is faster than T^{-1}. The mobility has an additional incoherent contribution that yields activated behavior (increasing mobility with increasing temperature) at intermediate temperature, where the activation temperature decreases with increasing g_H. At very high temperatures $k_B T \gg g^2 \omega_H$, we see the well-known $T^{-3/2}$ power-law dependence of Marcus theory [9]. In Fig. 3.3(a), we extend our results to unrealistically high temperatures $T \sim 10^5$ K only to show this asymptotic behavior.

Aside from the effects of band-narrowing – an overall reduction of mobility and faster than T^{-1} decay – the major signature of a high-frequency Holstein phonon is the presence of an activated regime However, our numerical results indicate that for parameters relevant to a high-mobility OMC, the activated regime is only observed at temperatures exceeding 1000 K. This is due to the high frequency of the intramolecular vibrations, on the order of $150-200$ meV. Therefore, we conclude that an intrinsic activated regime associated with polaron formation may not be observable in high-mobility OMCs. Other authors have drawn similar conclusions based on ab-initio Holstein phonon parameters in pentacene and naphthalene [15, 129], but to our knowledge this is the first time the activation temperature has been quantified for Holstein-Peierls mobility with quantum-mechanical phonons. However, the lack of activation at experimentally accessible temperatures does not indicate the absence nor irrelevance of strong intramolecular electron-phonon coupling.

Lastly, we analyze the DC mobility in the presence of both Holstein and Peierls electron-phonon couplings, which is only enabled by the new theory developed here. In comparing Fig. 3.3(b) and (c) (moderate and strong Peierls coupling, $g_P = 1$ and $g_P = 2$) to (a) (no Peierls coupling), it is clear that the temperature dependence of the mobility is dramatically affected by dynamic disorder, except for the case of very strong Holstein coupling (green data). The reason for this latter insensitivity is illustrated in Fig. 3.4(a), which shows the mean value (solid lines) and standard deviation of the renormalized transfer integral under moderate ($g_P = 1$) and strong ($g_P = 2$) Peierls coupling (dark and light shaded regions, respectively). We see that for $g_H = 2$, the mean value is nearly zero and, concomitantly, the fluctuations with these values of g_P are

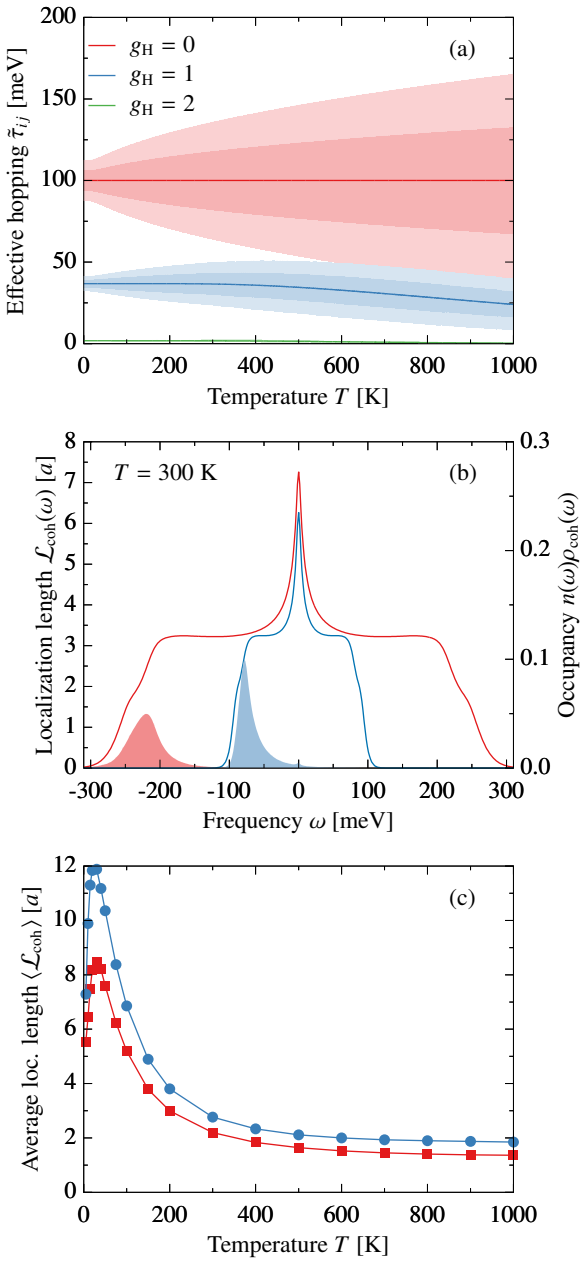

Figure 3.4. (a) Band-narrowed nearest-neighbor hopping $\tilde{\tau}$ (solid lines), for which the bare value is τ = 100 meV. Shaded regions represent one standard deviation in the distribution of values that $\tilde{\tau}$ can take under Peierls disorder with moderate coupling (g_P = 1, darker shading) and strong coupling (g_P = 2, lighter shading). (b) Energy-dependent localization length (solid lines) for zero Holstein coupling (g_H = 0, red) and moderate Holstein coupling (g_H = 1, blue) and thermally occupied density of states (shaded regions). Results are shown for T = 300 K and Peierls coupling g_P = 2. (c) Temperature-dependent average localization length with Peierls coupling g_P = 2. All other parameters are the same as in Fig. 3.1.

negligible.

Having seen that Peierls dynamic disorder has little effect in the large g_H limit, we will mainly

compare the $g_H = 0$ and $g_H = 1$ cases. As previously stated, $g_H = 1$ corresponds most closely to the estimated coupling strength in rubrene [22, 23, 101, 102], whereas the $g_H = 0$ case reduces to the dynamic disorder/transient localization picture that has so successfully captured the transport behavior of high-mobility OMCs in the past [19, 21]. In the temperature range of interest (10^2-10^3K), the $g_H = 0$ and $g_H = 1$ Holstein-Peierls mobilities are remarkably similar, exhibiting the well-known $\mu \propto T^{-\gamma}$ behavior, with $\gamma \approx 2$ characteristic of dynamic disorder-induced transient localization [20, 21, 99]. For $g_P = 2$ and $g_H = 0$ or 1, our extracted value of $\gamma \approx 1.8$ is slightly smaller than that determined from the slope of the mean-squared displacement in Refs. [19, 101]. This effect is potentially related to the spurious heating of quasiclassical dynamics [99, 110] and which is significantly less influential in our formulation based on the Kubo formalism.

The only major qualitative change induced by Holstein coupling is the activated behavior, which again occurs at unrealistically high temperatures exceeding 1000 K. In the dotted lines of Fig. 3.3, we show the mobility calculated in the absence of incoherent phonon effects, which is completely sufficient for experimentally relevant temperatures. This observation argues that the mobility of many OMCs should be simulated by a computational approach where the transfer integrals undergo a static but temperature-dependent renormalization due to the Holstein coupling to high-frequency intramolecular vibrations. These parameters are then used in a quasiclassical, time-dependent simulation of the electronic dynamics, following the usual prescriptions of dynamic disorder [19, 98, 101] or transient localization [20, 21, 99]. In Fig. 3.3(c), we compare our theoretical results to experimental Hall mobility data of the rubrene b-axis via Ref. [88]. Both the $g_H = 0$ and $g_H = 1$ data show excellent agreement in terms of the absolute magnitude and temperature dependence of the mobility.

Before concluding, we seek to understand the origin of the mobility's insensitivity to the Holstein coupling strength g_H, when $g_P \geq 1$ and $g_H \leq 1$. Figure 3.4(a) clearly shows that the magnitude of the renormalized transfer integral is significantly affected by g_H, which would suggest a strong dependence. However, Fig. 3.4(a) also demonstrates that the band-narrowing reduces the variance of the transfer integrals, which lessens the degree of localization. To test the proposal, we

analyze the localization properties of the electronic wavefunction averaged over disorder realizations and with statically renormalized transfer integrals. The energy-resolved coherent localization length, $\mathcal{L}_{\text{coh}}(\omega)$ can be obtained via the Thouless formalism [130, 131],

$$\mathcal{L}_{\text{coh}}^{-1}(\omega) = \frac{1}{L}\sum_{\alpha}\frac{l_{\alpha}^{-1}\delta(\omega-\tilde{\varepsilon}_{\alpha})}{\rho_{\text{coh}}(\omega)} \tag{3.27a}$$

$$l_{\alpha}^{-1} = \frac{1}{(L-1)a}\left(\sum_{\beta\neq\alpha}\ln|\tilde{\varepsilon}_{\beta}-\tilde{\varepsilon}_{\alpha}| - \sum_{i=1}^{L-1}\ln|\tilde{\tau}_{i,i+1}|\right) \tag{3.27b}$$

$$\rho_{\text{coh}}(\omega) = \frac{1}{L}\sum_{\alpha}\delta(\omega-\tilde{\varepsilon}_{\alpha}) \tag{3.27c}$$

where $\tilde{\varepsilon}_{\alpha} = \tilde{\varepsilon}_{\alpha}(\mathbf{X}_{\text{P}}, \mathbf{P}_{\text{P}})$ are eigenvalues of the band-narrowed and statically disordered electronic Hamiltonian. The above quantities $\mathcal{L}_{\text{coh}}(\omega)$ and $\rho_{\text{coh}}(\omega)$ are thermally averaged over the phonon degrees of freedom by Monte Carlo sampling as done in Eq. (3.8).

In Fig. 3.4(b), we show this disorder-averaged energy-dependent localization length $\mathcal{L}_{\text{coh}}(\omega)$ without and with Holstein electron-phonon coupling ($g_{\text{H}} = 0$ and $g_{\text{H}} = 1$) at an example temperature of $T = 300$ K. We observe three main features: highly localized states at the band edges, states with a constant localization length of a few lattice constants in the middle of the band, and an unphysical delocalized state at the band center due to the purely off-diagonal nature of the disorder. Crucially, in the case with Holstein electron-phonon coupling ($g_{\text{H}} = 1$), all of these features are compressed into a narrower energy spacing. The shaded region of Fig. 3.4(b) shows the thermally occupied density of states $n(\omega)\rho_{\text{coh}}(\omega)$, where $n(\omega) = e^{-\beta\omega}/Z_{\text{el}}$ is the thermal occupancy of single-particle electronic states. We see that the $g_{\text{H}} = 1$ occupied density of states extends much further into the band, giving added weight to the more delocalized states (similar to the effect of an increased electronic temperature). This yields a *larger* average localization length, which is defined by $\langle\mathcal{L}_{\text{coh}}\rangle = \int d\omega n(\omega)\rho_{\text{coh}}(\omega)\mathcal{L}_{\text{coh}}(\omega)$ and plotted in Fig. 3.4(c). Indeed, at all temperatures we see that the average localization length for a system with $g_{\text{H}} = 1$ is *larger* than that with $g_{\text{H}} = 0$. In other words, the addition of Holstein electron-phonon coupling yields electronic states that are, on average, *more* delocalized. This parameter-specific effect increases the mobility and

partially compensates for the decreased magnitude of the renormalized transfer integrals, producing a mobility that is relatively insensitive to the value of g_{H}, as seen in Fig. 3.3. This effect can qualitatively be understood by the fact that the ratio of the standard deviation of Peierls fluctuations to the average transfer integral is independent of g_{H} in the Lang-Firsov treatment, as can be seen in Eq. 3.16. However, while important, clearly this ratio is not the sole determinant of transport behavior over all values of g_{P} and g_{H}, as Fig. 3.3 demonstrates.

More broadly, at all values of g_{H}, we observe a maximum delocalization at low temperature and exponential decay with increasing temperature, as previously observed by Ciuchi and Fratini [20]. In our model, maximum delocalization does not occur at zero temperature because we include zero-point energy in the Peierls phonons by sampling from the Wigner distribution, which allows for localized states even at zero temperature. Interestingly, at these low temperatures $k_{\mathrm{B}}T < \omega_{\mathrm{P}}$ (with Wigner sampling), the degree of disorder is temperature-independent. The temperature dependence of the localization length only comes from the thermal average over electronic states, where higher energy states have a larger localization length, causing the average localization length to increase with increasing temperature up to $k_{\mathrm{B}}T \approx \omega_{\mathrm{P}}$. To summarize, we have seen that the temperature-dependent mobility is determined by a subtle competition between a Holstein-induced renormalization of electronic parameters and their variance, the finite-temperature dynamics of quasiclassical Peierls modes, and the thermal occupancy of electronic states with different localization lengths.

3.4 Conclusions

We have introduced a new approach to solving the Holstein-Peierls Hamiltonian for electron-phonon coupling in organic molecular crystals. We exploit the quasi-adiabatic nature of the intermolecular Peierls modes and treat them semiclassically. The lattice motions create a dynamically disordered landscape with broken translational symmetry that localizes the polaronic wavefunction. The intramolecular Holstein modes are accounted for by performing a Lang-Firsov polaron transformation, and separating the electron and Holstein phonon degrees of freedom through an

anti-adiabatic finite-temperature mean-field approximation. The resulting dynamics are nonperturbative in both the electronic and electron-phonon interactions. The polaronic dynamics exactly capture the limit of strong electron-phonon coupling, while reducing to the exact unitary electronic dynamics in the weak-coupling limit. We calculated the frequency-resolved spectral function and conductivity, as well as the zero-frequency DC mobility.

We found that finite-frequency observables such as the spectral function and optical conductivity are strongly affected by Holstein phonons even at moderate coupling strengths, especially at frequencies corresponding to multiples of the phonon energy. These features correspond to incoherent electron-phonon interactions, and are only enabled by a quantum mechanical treatment such as that presented here. Peierls disorder contributes peak-broadening and shifts spectral weight toward incoherent peaks. DC transport, in contrast to finite-frequency observables, is largely determined by dynamic disorder-induced localization of the coherent wavefunction [19, 21, 98, 99]. The DC mobility is only weakly affected by the Holstein interaction in the form of temperature-dependent band-narrowing, i.e. effective mass renormalization. An incoherent activated regime due to Holstein phonons is observed, but only at experimentally irrelevant temperatures, at least for the frequency of intramolecular vibrations considered here and relevant for most OMCs. We further support this conclusion by showing that including only Holstein band-narrowing, and excluding incoherent features, can reproduce the total mobility to high accuracy up to temperatures of around 1000 K.

Interestingly, we find that coherent band-narrowing due to Holstein coupling has less of an effect on overall transport than might be expected, because the bandwidth reduction is accompanied by a reduction in the variance and thus a reduction in the nonlocal dynamic disorder. Such an observation is only made possible by the unified theory presented in this work. This finding further indicates that the success of theories with purely nonlocal electron-phonon coupling may be partially due to a serendipitous cancellation of effects which makes local coupling to intramolecular vibrations appear less significant. Previous studies have shown that dynamic disorder enhances hopping transport in 1D, but the mechanism was due to completely incoherent pathways and there-

fore unrelated to localization [97]. Because localization properties are strongly dependent on dimensionality and potential anisotropy [132], the interplay of localization and band-renormalization may be significantly different in higher dimensions, which we consider an interesting topic for future study.

Perhaps most importantly, the relative simplicity of our approach enables application to more complex models and realistic materials, where numerically exact techniques struggle. Because the theory leads to a time-dependent Hamiltonian with separable electronic and phononic degrees of freedom, we imagine the straightforward inclusion of electronic interactions, treated using conventional methods of electronic structure theory in the absence of phonons. This extension would be important in semiconductors at higher doping densities or in metals with strong electron-phonon interactions. Furthermore, a more sophisticated treatment of the electron-phonon interaction, for example via variational optimization of the Lang-Firsov transformation, is also possible [133–135]. Finally, we emphasize that the quasiclassical treatment of low-frequency nuclear motion is not limited to the study of linear electron-phonon coupling or to harmonic nuclear degrees of freedom. Fully atomistic and anharmonic nuclear dynamics can be straightforwardly included; anharmonic effects are most important for low-frequency motions, which is precisely where the approach is valid. For example, in addition to OMCs [136], nonlinear electron-phonon coupling and anharmonic effects have been shown to be important in the electronic properties of lead-halide perovskites [137, 138] and for "phononic" control of nonequilibrium material properties [139, 140]. Work along all of these directions is underway and will enable nonperturbative treatment of electron-nuclear interactions in realistic, complex materials.

3.5 Appendix: Validity of the approximate Lang-Firsov treatment

In this appendix, we seek to benchmark the accuracy of the approximate Lang-Firsov treatment of the Holstein model by comparison with numerically exact results, using the same material parameters as considered in the main text. A large number of works have been devoted to the numerically exact treatment of electron-phonon problems, especially the Holstein model. In par-

ticular, variational techniques [141], the density matrix renormalization group [142, 143], exact diagonalization of small clusters [116, 117] and diagrammatic techniques [144] have been used to predict highly accurate or exact spectral properties for modestly sized 1D systems. Higher dimensional extensions have been explored within exact diagonalization [145] and dynamical mean field theory [146]. The later has been extended to finite doping and symmetry-broken phases [147, 148]. Here, we employ exact diagonalization over the variational Hilbert space (EDVHS), which is described in the next section.

3.5.1 Exact diagonalization over variational Hilbert space

EDVHS can be used to obtain a numerically exact solution of the Holstein polaron ground state [116], response functions [117] and nonequilibrium dynamics [149, 150]. The construction of the variational space starts from an electron in a translationally invariant state with no phonon excitations. We generate new parent states by applying the Hamiltonian, Eqs. (3.1a) and (3.1c). By choosing the number of Hamiltonian operations N_{H}, we control the maximal number of phonon quanta and the spatial extent of the polaron, which can be increased for convergence. After solving the ground state problem, the dynamical properties are evaluated using the continued fraction method [151].

All EDVHS calculations are converged with $N_{\mathrm{H}} = 20$ generations creating a Hilbert space with over 3×10^6 basis states. Lorentzian broadening with $\eta = 10$ meV for spectral functions and 15 meV for optical conductivity spectra were used in the presentation of spectra.

3.5.2 Spectral functions

The momentum-resolved spectral function for the Holstein model at zero temperature is presented in Fig. 3.5. We compare the numerically exact EDVHS results (top row) to the approximate Lang-Firsov treatment (bottom row). For intermediate coupling ($g_{\mathrm{H}} = 1$) we see good agreement, particularly in the dispersion of the quasiparticle peak and in the satellite structure near $k = 0$. These features are most relevant to the transport properties, which rely on the $k = 0$ contribution of

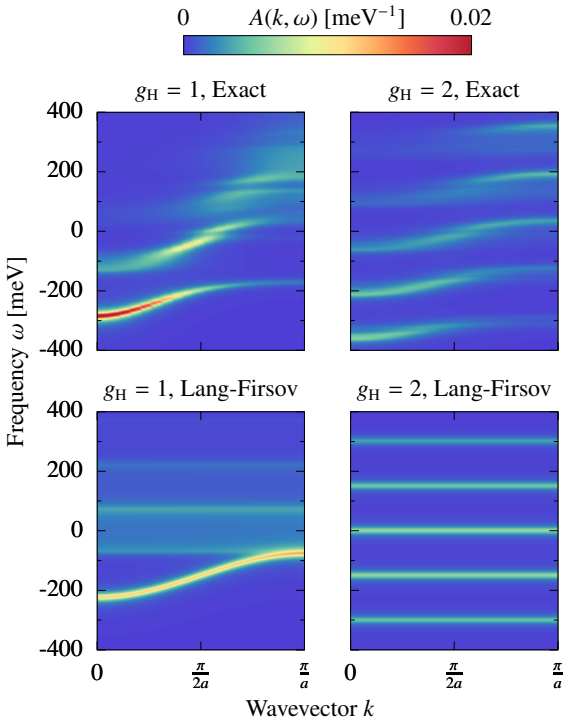

Figure 3.5. Momentum-resolved spectral function $A(k,\omega)$ at zero temperature obtained by numerically exact EDVHS results (top row) and approximate Lang-Firsov treatment (bottom row) at two different values of the Holstein electron-phonon coupling constant g_H. Results are calculated with the electronic transfer integral $\tau = 100$ meV, Holstein phonon frequency $\omega_H = 150$ meV, and a Lorentzian broadening with $\eta = 10$ meV.

the two-particle Green's function [17]. The satellite peaks, which are strictly dispersionless in the Lang-Firsov treatment, inherit some of the electronic dispersion in the exact results. At stronger electron-phonon coupling ($g = 2$), we see better agreement in the vibronic replica structure at all values of k; however the exact result again has slight dispersion in the peaks that is absent in the approximate result.

The positions of the spectral peaks are slightly shifted in the approximate result, which is due to an inaccurate ground-state energy of the $N = 1$ polaron problem. We examine this ground-state energy as a function of coupling strength g_H in Fig. 3.6(a), which shows that the Lang-Firsov approach is accurate and both weak and strong coupling; the intermediate-coupling regime of $g_H = 1 - 2$ is most challenging, but is qualitatively captured. We also note that a constant energy shift is not relevant for the conductivity, which depends only on energy differences at fixed electron number.

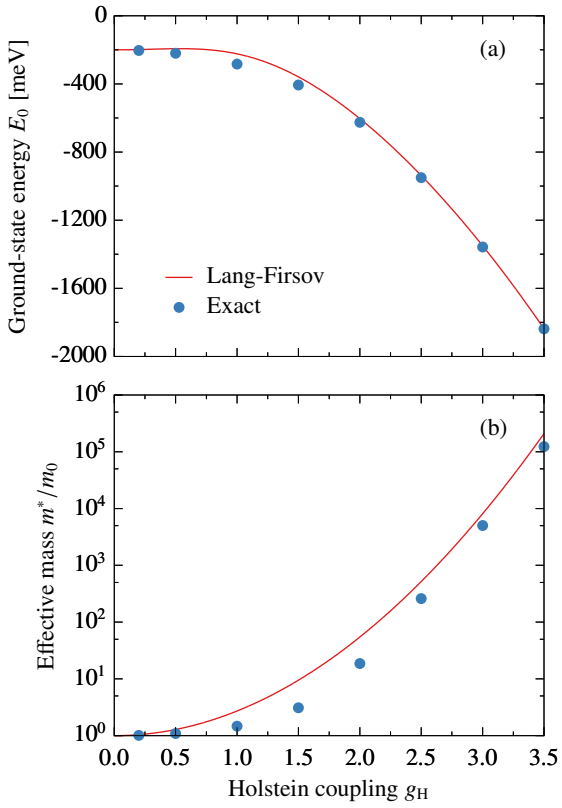

Figure 3.6. (a) Ground-state energy E_0 and (b) effective mass enhancement m^*/m_0 of the Holstein polaron at zero temperature, calculated via approximate Lang-Firsov and exact EDHVS. Calculated for the weakly anti-adiabatic case where $\tau = 100$ meV and $\omega_H = 150$ meV.

More important for transport is the quasiparticle effective mass at the bottom of the band. In Fig. 3.6(b) we look at the effective mass enhancement

$$\frac{m^*}{m_0} = \left[\frac{1}{2\tau}\nabla_k^2 E(k)\Big|_{k=0}\right]^{-1}, \tag{3.28}$$

which, within the Lang-Firsov approximation, is the inverse of the band-narrowing factor; at zero temperature, $m^*/m_0 = \tau/\tilde{\tau} = e^{g_H{}^2}$. Again we see that the Lang-Firsov approach is accurate at small and large values of the coupling constant but overestimates the mass enhancement at intermediate coupling.

Overall, we see good agreement between the approximate and exact spectral functions even in the weakly anti-adiabatic, intermediate-coupling regime relevant to high-mobility organic semiconductors. The approximate method is particularly accurate for the low-momentum, low-energy

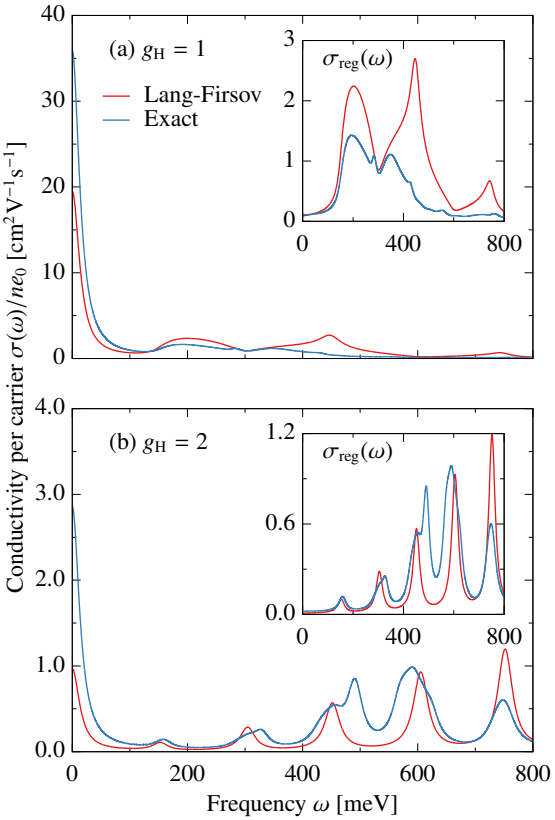

Figure 3.7. The per-particle optical conductivity $\sigma(\omega)/ne_0$ of the Holstein model at zero temperature obtained by numerically exact EDVHS and approximate Lang-Firsov treatment. Insets show the non-Drude regular conductivity, $\sigma_{\text{reg}}(\omega) = \sigma(\omega) - D\delta(\omega)$. Parameters are the same as in Fig. 3.5 except the broadening is $\eta = 15$ meV. Note that the vertical scales of (a) and (b) differ by a factor of 10.

features that are relevant for conductivity and DC transport at low density.

3.5.3 Optical conductivity

Next we examine the frequency-dependent optical conductivity, $\sigma(\omega)$, which is presented in the main panels of Fig. 3.7. The conductivity can be separated into a zero-frequency Drude contribution $D\delta(\omega)$ and a regular finite-frequency contribution $\sigma_{\text{reg}}(\omega)$; the latter is shown in the insets. Overall, the structure of the conductivity is well-reproduced by the Lang-Firsov treatment, including peak locations and lineshapes. The exact results show a complex mixture of coherent and incoherent features that contributes fine structure, which is absent in the approximate spectrum. The approximate Lang-Firsov approach predicts a structure that is dominated by regularly spaced

vibronic replicas similar to that seen in the single-site limit [17].

The low-frequency behavior, which determines transport properties, is qualitatively reproduced by the approximate treatment. For the case with moderate coupling ($g_{\mathrm{H}} = 1$), the Drude weights are in satisfactory agreement: $D = 0.68$ (exact) and $D = 0.37$ (approximate). At strong coupling ($g_{\mathrm{H}} = 2$), the agreement is slightly worse: $D = 0.054$ (exact) and $D = 0.018$ (approximate). At low density, the Drude weight is related to the effective mass via $D \propto 1/m^*$ and the underestimation of the Drude weight is consistent with the overestimation of the mass enhancement seen in Fig. 3.6(b).

To summarize our comparison of the conductivity at zero temperature, the low-frequency features show reasonable accuracy, including the zero-frequency Drude contribution and the locations and lineshapes of the first few excited-state peaks. Crucially, the nonperturbative Lang-Firsov approach captures exactly the weak- and strong-coupling limits, enabling far richer physics than those of the historically prevalent narrow-band approximation.

Chapter 4: Conductivity of electrons coupled to anharmonic phonons

The material in this chapter was taken from a manuscript currently being written with Petra Shih and Timothy C. Berkelbach.

4.1 Introduction

Design of efficient molecular semiconductors requires a detailed microscopic understanding of the charge transport mechanism. In recent years, low-frequency dynamic disorder has been shown to have a dominant role in the carrier dynamics of soft semiconductors such as organic molecular crystals and lead halide perovskites [19, 21, 82, 138]. The microscopic picture of dynamic disorder is often predicated on linear coupling of carriers to harmonic phonons; however, experimental and theoretical work suggests that the low-frequency phonon modes in organic molecular crystals exhibit significant anharmonicity [136, 137, 152–155].

Anharmonicity most commonly manifests in vibrational spectroscopies as two well-known effects: A frequency shift away from the harmonic value (*softening* or *hardening*), and a finite vibrational lifetime which introduces a spectral linewidth. Due to their temperature-dependent nature, anharmonic effects are critical in understanding and modeling the finite-temperature nuclear dynamics of a material. In solids, anharmonic effects are implicated in thermal expansion, thermal transport and structural phase transitions among other important nuclear effects [156, 157].

By modulating the lattice structure and dynamics, anharmonicity can also influences the electronic states of materials. For example, a structural phase transition associated with anharmonic mode-coupling has been shown induce an insulator-metal transition cuprates [158, 159]. Anharmonic modes are implicated in the band-gap renormalization of several materials such as halide perovskites [138, 160] and strontium titanite [161]. Soft modes in strontium titanite were also

shown to be responsible for the temperature dependence of the carrier mobility [162]. The aforementioned study made use of the perturbative Boltzmann transport equation with a temperature-dependent effective potential; however, many "soft" materials have strong electron-phonon coupling to low-frequency modes, which precludes the use of perturbative methods. The effect of vibrational anharmonicity on electronic transport in this context is not systematically known. Previous theoretical studies on organic molecular crystals have demonstrated that the details of the phonon dynamics, such as dispersion and symmetry, will lead to qualitative differences in the carrier dynamics, particularly for temperature-dependent mobilities [131, 163, 164]. In this paper, we introduce a nonperturbative semiclassical quantum dynamics approach to study the motion of charge carriers coupled to phonons with anharmonicity.

4.2 Theory

We study a single electron interacting with anharmonic phonons on a one-dimensional lattice at fixed volume with N sites and periodic boundary conditions. Each lattice site n has a single electronic orbital with creation operator $c_n^\dagger$ and a single nuclear degree of freedom with momentum p_n and displacement u_n. The Hamiltonian can be written as $H = H_{\text{el}} + H_{\text{ph}} + H_{\text{el-ph}}$ with

$$H_{\text{el}} = -\tau_0 \sum_n c_n^\dagger c_{n+1} + \text{H.c.} = \sum_k \varepsilon_k c_k^\dagger c_k, \tag{4.1}$$

$$\begin{aligned} H_{\text{ph}} &= \sum_n \frac{p_n^2}{2m} + V(u_1, u_2, \ldots, u_N) \\ &= \sum_k \left[\frac{p_k^2}{2} + \frac{1}{2}\omega_k^2 u_k^2 \right] + V^{\text{an}}(u_{k_1}, u_{k_2}, \ldots, u_{k_N}), \end{aligned} \tag{4.2}$$

where ω_k are the phonon frequencies and V^{an} is the anharmonic part of the potential energy surface. For the model considered here, the electronic bands and phonons are trivially defined by symmetry,

$$c_k^\dagger = N^{-1/2} \sum_n e^{-ikna} c_n^\dagger, \tag{4.3}$$

$$u_k = N^{-1/2} \sum_n e^{-ikna} u_n, \tag{4.4}$$

Here, we assume a linear Peierls form of the electron-phonon coupling

$$\begin{aligned} H_{\text{el-ph}} &= G \sum_n \left(c_n^\dagger c_{n+1} + \text{H.c.} \right) (u_{n+1} - u_n) \\ &= \sum_{kq} G_{kq} c_{k+q}^\dagger c_k u_{-q} = \sum_{kq} g_{kq} c_{k+q}^\dagger c_k (b_{-q}^\dagger + b_q) \end{aligned} \tag{4.5}$$

where

$$G_{kq} = \frac{2iG}{N^{1/2}} \{\sin(ka) - \sin[(k-q)a]\} \tag{4.6a}$$

$$g_{kq} = \left(\frac{\hbar}{2\omega_q} \right)^{1/2} G_{kq} \tag{4.6b}$$

The second-order perturbation theory scattering rates are

$$\Gamma_{k,k+q}(T) = \frac{|G_{kq}|^2}{\hbar^2} \int_{-\infty}^{\infty} dt e^{i(\varepsilon_k - \varepsilon_{k+q})t/\hbar} \langle u_q(t) u_{-q}(0) \rangle_{\text{ph}} \tag{4.7}$$

where $\langle O \rangle_{\text{ph}} = \text{Tr}_{\text{ph}}\{O e^{-\beta H_{\text{ph}}}\}/Z_{\text{ph}}$ is a thermal average over phonon degrees of freedom, $Z_{\text{ph}} = \text{Tr}_{\text{ph}}\{e^{-\beta H_{\text{ph}}}\}$ is the phonon partition function, and time-dependence is determined by the free phonon Hamiltonian $O(t) = e^{-iH_{\text{ph}}t/\hbar} O e^{iH_{\text{ph}}t/\hbar}$. In the absence of phonon-phonon interactions, the thermal correlation function can be evaluated analytically, leading to the familiar expression

$$\begin{aligned} \Gamma_{k,k+q}(T) = \frac{2\pi}{\hbar} |g_{kq}|^2 \Big\{ &[n_q + 1] \delta(\varepsilon_k - \varepsilon_{k+q} - \omega_q) \\ &+ n_q \delta(\varepsilon_k - \varepsilon_{k+q} + \omega_q) \Big\} \end{aligned} \tag{4.8}$$

and $\tau_k^{-1}(T) = \Gamma_k(T) = \sum_q \Gamma_{k,k+q}(T)$. In the limit of low ω_q, the quasielastic approximation can be made giving

$$\Gamma_{k,k+q}(T) = 2\pi\omega_0 k_\mathrm{B} T \left|\frac{g_{kq}}{\hbar\omega_q}\right|^2 \delta(\varepsilon_k - \varepsilon_{k+q}) \Big\{1 - \cos\big(\theta_{k,k+q}\big)\Big\}, \tag{4.9}$$

where $\omega_q = \omega_0$ for optical and $2\omega_q = \omega_0|\sin(qa/2)|$ for acoustic phonons, and $1 - \cos\big(\theta_{k-q,k}\big) = 1 - (k-q)/k$ in one dimension. Within linearized Boltzmann transport theory with the above state-dependent relaxation times, the charge conductivity in one dimension is given by

$$\sigma_\mathrm{DC} = \frac{e^2}{Nak_\mathrm{B}T} \sum_k v_k^2 \tau_k e^{-\varepsilon_k/k_\mathrm{B}T} / Z_\mathrm{el} \tag{4.10}$$

where $Z_\mathrm{el} = \sum_k e^{-\varepsilon_k/k_\mathrm{B}T}$ is the electronic partition function, $v_k = \hbar^{-1}\partial\varepsilon_k/\partial k$ is the band velocity and we have enforced concentration $c = (Na)^{-1}$. The mobility is $\mu = \sigma_\mathrm{DC}/(ec)$.

The above theory makes two independent approximations: it is strictly harmonic and it is perturbative. The former can be relaxed if the time correlation function of the phonons in Eq. (4.7) can be evaluated exactly. Throughout this work, we assume phonon frequencies and temperatures that justify a classical treatment of the nuclei so that the correlation function can be evaluated by standard molecular dynamics. An alternative but approximate route for treating the anharmonicity is through the use of an effective, temperature-dependent harmonic model, i.e.

$$V \approx \frac{1}{2} \sum_k \tilde{\omega}_k^2(T)\, u_k^2 \equiv \tilde{V} \tag{4.11}$$

The effective phonon frequencies $\tilde{\omega}_k(T)$ can be determined by a number of methods, including mean-field theory, perturbation theory, the self-consistent harmonic approximation, and the temperature-dependent effective potential method. Motivated by the anharmonic result Eq. (4.7), here we propose to determine the effective frequencies by matching the zero-time value of the correlation function, i.e. $\langle|u_k|^2\rangle$. This approximation is good if the phonon lifetime is long compared to the electronic lifetime and will simply give rates of the form of Eq. (**??**) with temperature-

dependent frequencies $\tilde{\omega}_k(T)$. This matching yields

$$\tilde{\omega}_k^2 = k_B T / \langle |u_k|^2 \rangle_{an}. \tag{4.12}$$

Clearly, this criterion, motivated by perturbation theory in the electron-phonon coupling, is equivalent to finding a harmonic potential with the same variance as the anharmonic potential, i.e., it is a mean-field type treatment of the phonon anharmonicity.

In order to avoid perturbation theory in the electron-phonon coupling, we appeal to the quasi-classical Ehrenfest approach. Specifically, we let the nuclear degrees of freedom evolve according to Newtonian dynamics on the anharmonic potential energy surface,

$$m\ddot{u}_i = -\frac{dV}{du_i}. \tag{4.13}$$

From the nuclear trajectories $u_i(t)$, we define a time-dependent electronic Hamiltonian

$$\begin{aligned} H_{el}(t) &= \sum_n \{-\tau_0 + G[u_{n+1}(t) - u_n(t)]\} \left(c_n^\dagger c_{n+1} + \text{H.c.} \right) \\ &= \sum_{kq} \left[\varepsilon_k \delta_{kq} + G_{kq} u_{-q}(t) \right] c_{k+q}^\dagger c_k \end{aligned} \tag{4.14}$$

which is used in a mixed quantum-classical evaluation of the electronic current-current correlation function,

$$C_{jj}(t) = \int d\boldsymbol{u} \int d\boldsymbol{p}\, \mathcal{P}(\boldsymbol{u}, \boldsymbol{p}) \langle U_{el}(0,t)\, j(t)\, U_{el}(t,0)\, j \rangle_{el} \tag{4.15}$$

where $\mathcal{P}(\boldsymbol{u}, \boldsymbol{p})$ is the phase-space distribution of the classical nuclear degrees of freedom, $U_{el}(t,0)$ is the time-ordered evolution operator,

$$U_{el}(t,0) = T \exp\left[-i \int_0^t dt' H_{el}(t') \right], \tag{4.16}$$

and the current operator is

$$j(t) = -ia \sum_n \{-\tau_0 + G[u_{n+1}(t) - u_n(t)]\} \left(c_n^\dagger c_{n+1} - \text{H.c.}\right), \tag{4.17}$$

where a is the lattice constant. From this, the AC conductivity is readily obtained

$$\text{Re}\sigma(\omega) = \frac{1 - e^{-\beta\omega}}{2L\omega} \int_{-\infty}^{+\infty} dt\ e^{i\omega t} C_{jj}(t). \tag{4.18}$$

with the DC component obtained by taking the zero-frequency limit, $\sigma_{\text{DC}} \equiv \sigma(\omega \to 0)$.

4.3 Results and Discussion

4.3.1 Simulation Details

As a starting point for our transport model, we use the parameters from Ref. [101] for the b-axis of single-crystal rubrene. These parameters represent an idealized model for a 1D high mobility axis of a molecular crystal and have been used in numerous studies [21, 82, 128]. The parameters are $\tau_0 = 143$ meV, $\omega_0 = 6.2$ meV and $G = 493.5$ meV/Å ($g = 12.4$ meV). The lattice constant $a = 7.2$ Å. For the dynamical Kubo formula, we used a lattice size of 100 sites with periodic boundary conditions; we tested the mobility calculations with larger lattice sizes to confirm convergence with respect to finite size. For the static Kubo formula results we increased the lattice to 200 sites. We sampled up to 50 000 trajectories for each calculation to converge all results with respect to phonon ensemble sampling.

4.3.2 Optical Phonon Anharmonicity

In order to understand the effect of potentials beyond harmonic order, we choose $V(u_1, u_2, ..., u_N)$ on a truncated expansion up to fourth order,

$$V(u_1, u_2, \ldots, u_N) = \sum_{n=1}^{N} \frac{1}{2}\omega_0^2 u_n^2 + c_3 u_n^3 + c_4 u_n^4. \tag{4.19}$$

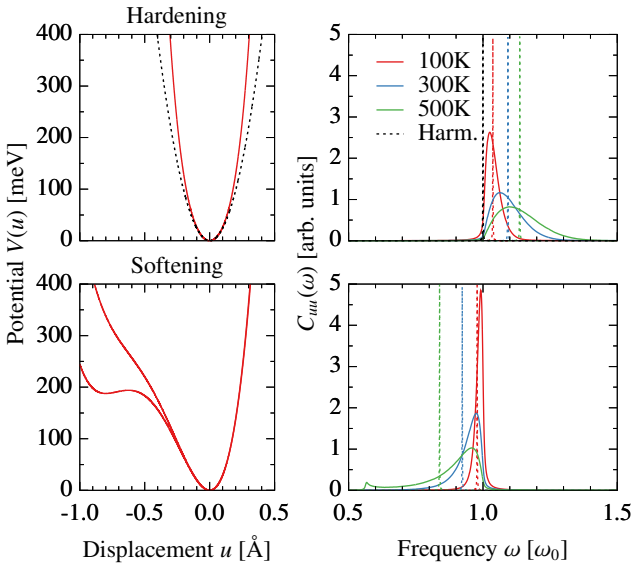

Figure 4.1. Potential $V(u)$ (left) and power spectrum $C_{uu}(\omega)$ (right) for optical phonons. The phonon potential is of the form in Eq. 4.19 with hardening (top left, red) corresponding to $c_3 = 0$ and $c_4 = 4\omega_0^2$. The phonon softening potentials (bottom left) both use $c_4 = 0.5\omega_0^2$ with $c_3 = 0.9\omega_0^2$ and $0.95\omega_0^2$ for the single and double well, respectively. The dashed black curve is the harmonic potential with $c_3 = c_4 = 0$ (top left). The power spectrum $C_{uu}(\omega)$ is shown at different temperatures using the hardening parameters (top right) and the single-well softening parameters (bottom right). The dashed lines correspond to the effective harmonic frequencies $\tilde{\omega}(T)$ obtained using Eq. 4.12.

Aside from the trivial harmonic limit with $c_3 = c_4 = 0$, we consider two main cases. First is the quartic potential where $c_3 = 0$ and $c_4 \neq 0$. This results in a symmetric potential with "harder" walls than the harmonic case, resulting in an increase in frequency with temperature and with increasing $|c_4|$. We will refer to this case as "phonon hardening". On the top left of Fig. 4.1 we show the single-mode potential $V(u)$ vs. u with $c_4 = 4\omega_0$ and $c_3 = 0$ (solid red line) compared to the harmonic potential (black dashed line). The top right shows the power spectrum $C_{uu}(\omega) = \int dt^{i\omega t} C_{uu}(t)$, where $C_{uu}(t) = \langle u(t)u(0)\rangle_{\text{an}}$, the displacement autocorrelation function. In the harmonic limit, $C_{uu}(t) = \langle u^2\rangle_{\text{harm}} \cos(\omega_0 t) = [k_B T/\omega_0^2] \cos(\omega_0 t)$, which of course results in a $C_{uu}(\omega)$ that is simply a delta function at ω_0 (black dashed line). The true anharmonic spectra (red, blue and green solid lines) show an upward shift in frequency and natural linewidth, both of which increase with temperature.

The second case we consider is that of "phonon softening", for which we use the a potential with $|c_3| > |c_4| > 0$ (bottom left panel of Fig. 4.1). The inclusion of a quartic term (or any even

term as the highest truncation order) is necessary to maintain a bounded potential. Depending on c_3, this potential can present as an asymmetric single well or double well. The crossover from single to double well $|c_3| > 0.94\omega_0\sqrt{2c_4}$, with a degenerate double well occurring at $|c_3| = \omega_0\sqrt{2c_4}$. Throughout the paper, for "soft" phonon parameters we use $c_4 = 0.5\omega_0^2$ and $c_3 = 0.9\omega_0^2$ and $0.95\omega_0^2$ corresponding to the asymmetric single well and double well shown on the bottom left of Fig. 4.1, respectively.

In the lower right hand panel of Fig. 4.1 we show the power spectrum $C_{uu}(\omega)$ for the asymmetric single well case. The spectra show a shift to lower frequency and greater linewidth with increasing temperature. A small peak appears between 0.5 and $0.6\omega_0$ which gains intensity but does not shift with temperature; the spectral tail does not extend to frequencies below this peak. To illustrate the phonon softening effects, we only show the single well example; the double well parameters produce qualitatively similar effects with slightly larger frequency shift and broadening.

4.3.3 Carrier Dynamics with Optical Phonons

On the left hand side of Fig. 4.2 we present the mobility of a carrier coupled to an optical phonon, using three different levels of approximation: two versions of the Kubo formula, and the perturbative Boltzmann transport equation (BTE). Previous studies of conductivity performed via the Kubo formula have generally been done in the adiabatic limit such that Eq. 4.18 reduces to

$$\mathrm{Re}\sigma(\omega) = \frac{1 - e^{-\beta\omega}}{2L\omega} \sum_{mn} |\langle m|j|n\rangle|^2 \delta(\varepsilon_m - \varepsilon_n + \omega), \tag{4.20}$$

where m and n are eigenstates of the now time-independent electronic Hamiltonian. Like Eq. 4.18, Eq. 4.20 is performed over many realizations sampling the phonon phase space. One major drawback of the adiabatic approach is that the delta function in Eq. 4.20 must be given some artificial linewidth η to obtain a zero-frequency mobility for the finite system. This is equivalent to imposing an artificial decay to the current autocorrelation function $C_{jj}(t)$. This procedure is nearly identical to the procedure termed the "relaxation time approximation" in the transient localization

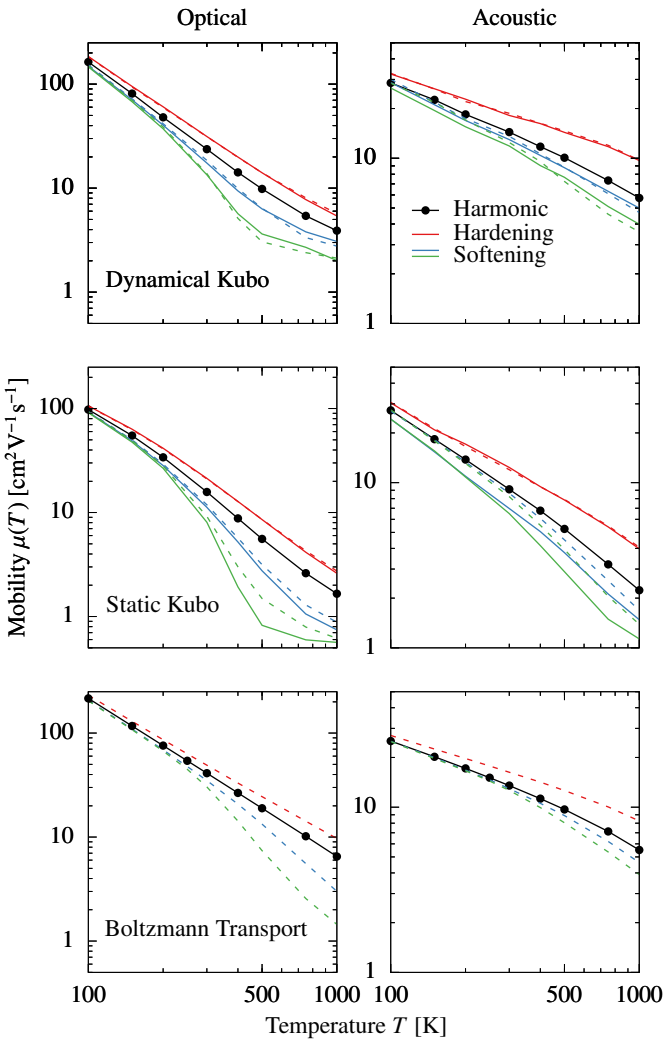

Figure 4.2. Log-log plot of temperature-dependent mobility $\mu(T)$ for a carrier coupled to an optical phonon (left) or acoustic phonon (right). Mobility is calculated with the dynamical Kubo formula (top), the static Kubo formula with $\eta = \hbar\omega_0/2$ (middle) and the Boltzmann transport equation (bottom). In addition to the mobility with harmonic phonons (black dotted lines), we show mobility with hard modes (solid red) and soft modes (blue and green). The dashed data correspond to mobility calculated using harmonic phonons with a temperature-dependent effective frequency via Eq. 4.12, while solid lines use the full anharmonic potential.

literature, except in that case, the current anticommutator correlation function is used[21]. The use of artificial broadening makes the approximation that $C_{jj}(t)$ decays exponentially with a fixed time constant $1/\eta$, and changes in η have been shown to dramatically qualitatively affect the temperature dependence of the mobility [128]. This ambiguity is avoided in the dynamical Kubo approach, as $C_{jj}(t)$ decays naturally due to the dynamic nature of the disorder.

We will first briefly discuss the behavior of a carrier coupled to a harmonic optical phonon for the three different methods presented on the left hand side of Fig. 4.2 (black dotted lines). The top left panel shows results of the full dynamical Kubo formula, Eq. 4.13-4.18. Below 500 K we observe a power-law relationship of roughly $\mu \propto T^{-1.8}$, consistent with other Kubo formula calculations [21, 128, 131, 163] and Ehrenfest-style mixed quantum-classical diffusion models [19, 101, 109, 165]. We see that the "band-like" power law behavior extends to low temperatures, but the mobility begins to saturate above around 500 K, a well-known feature of the nonperturbative semiclassical models equivalent to resistivity saturation in metals [20, 166]. In the static disorder limit with $\eta = \omega_0/2$, the Kubo formula produces similar features (left center panel); however, there are a few key differences. First, static Kubo formula predicts a different power law exponent, and in general this exponent can be changed with the choice of η. Secondly, the band-like behavior does not extent to low temperature, but rather starts to plateau below 300 K. This is again due to the fixed broadening for all temperatures; in general, the *dynamical* Kubo formula produces less broadening of $C_{jj}(\omega)$ at lower temperature. Finally, we compare to the quasielastic BTE (bottom left panel). This theory predicts a power law of $T^{-1.5}$ at low-temperature and T^{-2} at high-temperature. It fails to capture high-temperature mobility saturation, which is a well-known failing of weak-coupling perturbation theory. The mobility saturation regime occurs near the Mott-Ioffe-Regel limit where the mean free path of the carrier is less than the lattice constant, at which point the BTE breaks down [20, 21].

Now that we have introduced the features of temperature dependent mobility for carriers with harmonic phonons, we will explore the effect of adding phonon anharmonicity. Phonon hardening has a rather prosaic effect of increasing the overall mobility and slightly decreasing the power

law exponent (solid red line). This change must be due to the two main features of anharmonic phonons – the frequency shift and the finite lifetime. To separate these effects and explore the validity of an effective harmonic treatment, we find an effective harmonic frequency, $\tilde{\omega}(T)$, at each temperature via Eq. 4.12. The effective frequencies at a few temperatures are shown on the right hand side of Fig. 4.1 (dashed lines). The condition in Eq. 4.12 guarantees that the disorder of the transfer integral, quantified as $\langle\tau^2\rangle/\langle\tau\rangle$, matches between the anharmonic and effective harmonic models. We see that for phonon hardening, the mobility in Fig. 4.2 matches extremely well between the fully anharmonic model (solid red) and the effective harmonic model (dashed red data). In other words, phonon lifetime has no appreciable effect on the mobility. This is not overly surprising given the separation of timescale; the current correlation function decays in a matter of hundred of fs, whereas phonon lifetimes are thousands of fs even at high temperature. Because of this timescale separation, the effect of phonon hardening is qualitatively identical between the dynamical and static implementation of the Kubo formula. Within the BTE framework, we can only use the effective harmonic approximation; phonon hardening has qualitatively the same effect, and for optical phonons, within this framework the mobility is just scaled by a factor of $\tilde{\omega}(T)/\omega_0$.

Phonon softening has the effect of reducing the mobility and pushing the high-temperature regime (ie mobility saturation for Kubo, $\mu \propto T^{-2}$ for BTE) to lower temperature. We show the mobility for two different soft mode cases discussed in the previous section: an asymmetric single well (blue data) and double well (green data). The anharmonic peak shift, and thus the reduction in mobility with temperature, is more precipitous with for the double well. The static Kubo formula overstates the effect of phonon softening compared to the dynamical Kubo formula; this is especially true for the fully anharmonic case (solid lines). Within the dynamical Kubo results, the effective harmonic and fully anharmonic results show good agreement, with the fully anharmonic results slightly *under*-estimating the mobility at high temperature. The opposite is true for the static Kubo formula, in which case the effective harmonic potential *over*-estimates the high temperature mobility. Within the static Kubo framework, discrepancies between mobilities with the effective harmonic and with fully anharmonic potential are entirely due to the shape of the disorder distri-

bution. While both cases have precisely the same electronic disorder variance $\langle\tau^2\rangle/\langle\tau\rangle$, the fully anharmonic potential produces a highly non-gaussian disorder profile while the effective harmonic potential produces a precisely gaussian distribution. We conclude that while the transfer integral variance $\langle\tau^2\rangle/\langle\tau\rangle$ is still a qualitative indicator of the reduction in transport due to disorder, highly anharmonic potentials may have nongaussian disorder profiles that render this metric less accurate, as evidenced by the disagreement between the effective harmonic and full potential. Aside from disorder, the other contributor to mobility is the electronic lifetime η^{-1}. We used a constant $\eta = \hbar\omega_0/2$ regardless of the effective frequency $\tilde{\omega}(T)$ for the static Kubo results. Using $\eta = \hbar\tilde{\omega}/2$ produces an even larger discrepancy with the dynamical Kubo results and a large overstatement of the effect of phonon softening on carrier mobility. In the dynamical Kubo formula, the finite phonon lifetime may slightly alleviate the impact of the phonon softening on mobility, which is why we see the harmonic approximation (where phonon lifetimes are infinite) *under*-estimate mobility. Phonon softening accentuates the disagreement between BTE and the nonperturbative Kubo formula results, since it precipitates the onset of the high-temperature regime where the BTE is invalid. For example, while the onset of the the Mott-Ioffe-Regel regime occurs around 400-500 K for the regular harmonic potential, the shift in frequency causes the crossover to occur close to 200-300 K in the case of the double well potential. In summary, the DC mobility of an electron coupled to an anharmonic phonon is fairly well-characterized by an effective harmonic potential within the full dynamical Kubo formula; this approximation becomes less accurate for static disorder models. This harmonic approximation is the only way to apply BTE, which retains its pathologies at high temperature and strong electron-phonon coupling strength.

Having examined the DC mobility for optical phonons, we will now discuss the full AC conductivity for the same systems. Fig. 4.3 shows the AC conductivity calculated via the dynamical Kubo formula with optical phonons (left side) at three different temperatures. The top left panel shows the harmonic behavior. We see the characteristic features of asymmetric (Su-Schrieffer-Heeger-type) electron-phonon coupling to optical phonons [128, 163, 167]. Peaks appear at low frequency (below 50 meV), and at multiples of the half bandwidth $2\tau_0$ (around 300 and 600 meV).

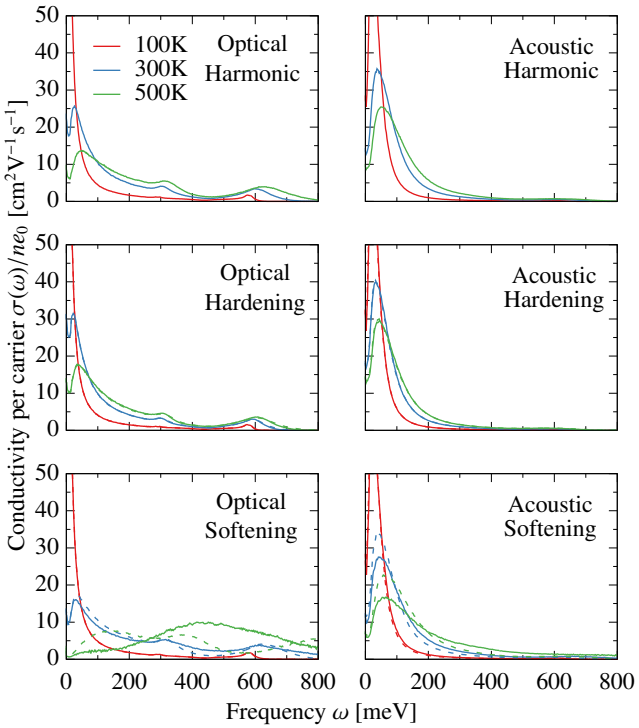

Figure 4.3. Per-carrier AC conductivity $\sigma(\omega)/ne_0$ for particles coupled to optical (left) and acoustic phonons (right). Conductivity shown at different temperatures for harmonic phonons (top), hard modes (middle) and double-well soft modes (bottom) and are calcualted using the dynamical Kubo formula. Dashed lines use an effective harmonic potential with $\tilde{\omega}$ from Eq. 4.12 whereas solid lines use the full anharmonic potential.

At 100 K most of the spectral weight is on the low-frequency peak that intersects with the zero-frequency axis. As temperature increases, spectral weight shifts to the higher energy peaks, and away from the zero-frequency intercept (corresponding to a reduction in DC mobility).

Hardening of optical phonons produces an effect like a reduced effective temperature - intensity increases at low frequency and decrease at high frequency (center left panel). The effective harmonic model (dashed lines) produces near-exact agreement, as it does for mobility in Fig. 4.2. The bottom left panel shows softening with the double-well potential ($c_3 = 0.95\omega_0^2$). This has the opposite effect, creating an effect similar to an increased temperature. Although the zero-frequency intercepts are fairly close between the effective harmonic and fully anharmonic model, the lineshapes and locations are qualitatively different, with the fully anharmonic model producing substantially broader peaks. This is primarily due to the inability to replicate the asymmetric, non-gaussian disorder profile with a harmonic potential.

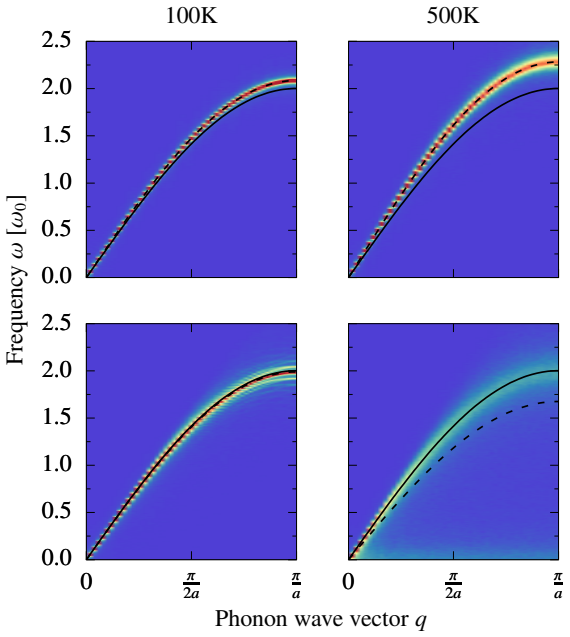

Figure 4.4. Momentum-resolved power spectrum $C_{uu}(q,\omega)$ for acoustic phonons. The color map data show the spectra for the hard mode potential (top) and double-well soft mode potential (bottom) at two different temperatures. The solid black line shows the harmonic dispersion $2\omega_0|\sin(qa/2)|$, while the dashed black line shows the effective harmonic dispersion $2\tilde{\omega}(T)|\sin(qa/2)|$.

4.3.4 Acoustic Phonon Anharmonicity

To get a better picture of real interactions in materials, we will also examine the effect of anharmonicity on dispersive phonons. It has been demonstrated that acoustic phonons lead to qualitatively different transport behavior compared to optical phonons [131, 164]. The real-space acoustic lattice Hamiltonian is

$$\begin{aligned} V(u_1,u_2,\ldots,u_N) &= \sum_{n=1}^{N} \frac{1}{2}\omega_0^2(u_n-u_{n+1})^2 \\ &+c_3(u_n-u_{n+1})^3 + c_4(u_n-u_{n+1})^4, \end{aligned} \tag{4.21}$$

where the first line is the regular harmonic Hamiltonian for acoustic phonons and the subsequent two lines are the anharmonic terms. We truncate the potential in real space, allowing only nearest-neighbor interactions up to fourth order. Because of this choice, the anharmonic part of the k-space Hamiltonian $V^{\text{an}}(u_{k_1},u_{k_2},\ldots,u_{k_N})$ will potential be nonzero up to infinite order. For

convenience we use the same force parameters (ω_0, c_3 and c_4) as the optical phonons, but note this definition means the maximum harmonic frequency will be $2\omega_0$ with harmonic dispersion $\omega_q = 2\omega_0|\sin(qa/2)|$. Momentum-resolved power spectra $C_{uu}(q,\omega)$ are shown in Fig. 4.4, compared to the harmonic dispersion (solid black line). For phonon hardening, we see that there is a is a well-defined positive shift is the peak that increases with temperature. The dispersion of this hardened peak also lies directly on top of the effective harmonic frequency $2\tilde{\omega}(T)|\sin(qa/2)|$ (dashed black line). While there is an increase in linewidth, it is not as substantial as in optical phonons for similar parameters. The opposite is true in the case of soft acoustic phonons (bottom panels, with $c_3 = 0.95\omega_0^2$). While the spectrum acquires a substantial linewidth, the downward shift in frequency is not visually obvious even at high temperature (lower right panel), although the effective harmonic frequency (dash line) predicts it is occurring.

4.3.5 Carrier Dynamics with Acoustic Phonons

We now will examine the dynamics of a carrier coupled to anharmonic acoustic phonons. The right hand side of Fig. 4.2 shows the temperature dependent mobility. For harmonic acoustic phonons, the dynamical Kubo formula predicts a power law of roughly $\mu \propto T^{-1/2}$ below around 500 K. In the regime where saturation occurs for optical phonons, the mobility has the opposite behavior for acoustic phonons, showing an increase in the power law exponent. Static Kubo and BTE calculation show similar behavior, with BTE predicting $\mu \propto T^{-1/2}$ at low temperature at $\mu \propto T^{-2}$ at high temperature. Just as for optical phonons, the static Kubo formula gives a temperature dependence which is sensitive to the chosen broadening parameter, which here we keep as $\eta = 0.5\hbar\omega_0$.

Acoustic phonon hardening produces the expected behavior based on our previous analysis. It simply shifts the mobility up for all temperatures, and reduces the power-law exponent. The fully anharmonic and effective harmonic model (solid and dashed lines) agree almost exactly, which is not surprising given the well-defined shifted spectrum in Fig. 4.4. While the disorder associated with the hard mode will be non-gaussian, the distribution is still symmetric and therefore is well-

approximated by gaussian disorder. With hard modes, we see good agreement in mobilities across all methods, with slight differences in the overall magnitude and temperature dependence due to the underlying approximations.

For phonon softening, we see much more disagreement between methods and between the fully anharmonic and effective harmonic models. Just as for optical phonons, there is always a reduction in mobility. For the dynamical Kubo formula, there is decent agreement between fully anharmonic and effective harmonic mobility for both single- and double-well potentials (top right panel, solid and dashed blue and green lines). The effective harmonic model does, however, overestimate mobility at low temperature and underestimate it at high temperature. Disagreement is much more pronounced for the static Kubo formula, where the fully anharmonic potential predicts much lower mobilities than the harmonic model for all temperatures. BTE mobility, which can only be calculated with effective harmonic phonons, agrees fairly well with the dynamical Kubo mobility predictions for soft modes. Frequency-resolved AC conductivity with acoustic phonons is shown in the right hand side of Fig. 4.3. Acoustic phonons result in a single low-frequency peak with no band-edge to band-edge and band-edge to band-center transitions present for optical modes. Otherwise, we see similar results for AC conductivity, with the effective harmonic model working well for phonon hardening but underestimating the linewidth for soft modes.

To understand why an effective harmonic approximation may be inadequate to capture the temperature-dependent mobility, we examine the underlying disorder profile. The bottom panel of Fig. 4.5 shows the distribution of electronic coupling τ for three different potentials with identical mean $\langle\tau\rangle$ and variance $\langle\tau\rangle$ – one effective harmonic, producing a gaussian distribution, and two anharmonic with $c_3 = 0.95\omega_0$ and $c_3 = -0.95\omega_0$. While the overall mean and variance are the same, the anharmonic distributions are asymmetric in energy; however, they both result in identical approximate harmonic potentials. The top panel shows the static Kubo mobility for each of these potentials; we observe that the magnitude and temperature-dependence of the mobility differs depending on the sign of c_3, an effect that cannot be captured by harmonic models. While asymmetric potentials are difficult to capture using a harmonic model for optical modes, the issue

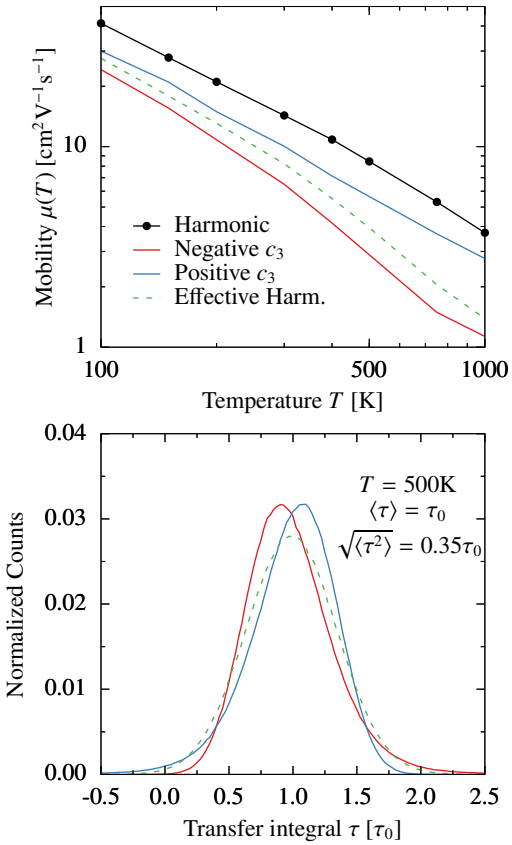

Figure 4.5. Static Kubo formula mobility with $\eta = 0.5\hbar\omega_0$ (top panel) and example distributions of transfer integral τ at 500K (bottom panel) for carriers coupled to a soft acoustic mode. All distributions in the bottom panel share the same average transfer integral $\langle\tau\rangle$ and variance $\langle\tau^2\rangle$, with the red and blue curves differing only in the *sign* of the cubic coefficient $c_3 = \pm 0.95\omega_0^2$. Both potentials lead to the same effective harmonic distribution of τ and mobility (dashed lines).

of asymmetric distributions of τ is not present. This is because $\tau_n = -\tau_0 + G[u_{n+1}(t) - u_n(t)]$, so if u_{n+1} and u_n are uncorrelated (as is the case for dispersionless phonons), we will have a symmetric distribution for τ even for asymmetric potentials. Correlated modes, like those in acoustic phonons, produce an asymmetric distribution of τ and thus creates the ambiguity shown in the top panel of Fig. 4.5.

4.4 Conclusions

We have introduced a nonperturbative semiclassical procedure for studying the impact of low-frequency lattice anharmonicity on electronic transport in soft materials. We also devised a criterion for creating an effective harmonic model from a given anharmonic potential by matching the variance and therefore the electronic disorder. This criterion allows us to compare with the perturbative Boltzmann transport equations, which requires harmonic phonons. For all methods we see a change in the magnitude and temperature dependence of mobility based on the extent and form of the anharmonicity (mode hardening or softening). Within the dynamical Kubo formula, changes to the mobility are well-characterized by a shifted harmonic potential, especially for optical phonons. The Kubo formula with static phonons overestimates the impact of anharmonicity, and in particular overestimates the increased disorder caused by mode softening. The effective harmonic potential is also less accurate within the static phonon approximation for the Kubo formula. This discrepancy is especially apparent for acoustic phonons, where the correlated phonon motion due to mode-coupling can lead to complex asymmetric disorder profiles that cannot be unambiguously modeled by a harmonic potential. Using a shifted harmonic potential with the Boltzmann transport equation is only useful in the regime where the BTE is valid (at temperatures below the Mott-Ioffe-Regel limit), and even in that case it underestimates the impact of anharmonicity on transport compared to nonperturbative methods.

In the future, this work could be extended to include thermal expansion of the lattice, which is important in real materials. Our approach could also be used to gain insight into the electronic response to lattice strain, which has thus for been mostly limited to harmonic models [168, 169].

The conclusions of this study suggest that minimizing soft modes and engineering "hard" lattice interactions in new materials will increase performance. This adds new microscopic insight to the growing list of design principles aiding in the suppression of dynamic disorder [16, 170, 171]. Our work also suggests that explicit inclusions of anharmonic dynamics may be important for accurate prediction of electronic transport, and that models with gaussian static disorder will qualitatively fail for sufficiently soft modes.

Chapter 5: Vibrational heat-bath configuration interaction

The material for this chapter was taken from Reference [172].

5.1 Introduction

Precise computational predictions of the vibrational structure of molecules and solids requires the inclusion of anharmonic effects, which correspond to interactions between harmonic normal modes. When treated quantum mechanically, this requires the accurate solution of the vibrational Schrödinger equation on a high-dimensional potential energy surface. Like in electronic structure theory, a hierarchy of wavefunction-based methods are commonly employed to avoid the exponential cost associated with an exact quantum solution; such methods include vibrational self-consistent field (VSCF) theory [26, 173–177] vibrational perturbation theory[24, 25, 178], vibrational coupled-cluster theory [29, 179, 180], and vibrational configuration interaction (VCI)[28, 181, 182]. These methods rely on the accuracy of the harmonic approximation and alternative methods have recently been developed to achieve quantitative accuracy for strongly anharmonic vibrations. Such methods include the nonproduct quadrature approach[183], reduced rank block power method (RRBPM), which uses a tensor factorization of the vibrational wavefunction [184], and adaptive VCI (A-VCI), which accelerates the VCI process using nested basis functions [185].

For strongly correlated electronic systems, the past two decades have seen the development of powerful computational methods that could be brought to bear on strongly anharmonic vibrational systems. For example, a vibrational density matrix renormalization group approach was recently developed and applied to systems with up to sixteen atoms [30]. In this work, we are primarily interested in selected configuration interaction [186–188], which began in the 1970s with CI by perturbatively selecting iteratively (CIPSI) [186] and has experienced renewed interest in the form

of adaptive configuration interaction [189], adaptive sampling CI (ASCI) [190, 191], and heat-bath CI (HCI) [192–195], among others. In CIPSI, many-body basis states are added to the variational CI space based on a first-order approximation of their wavefunction coefficients. Unlike CIPSI, which considers all states belonging to the first-order interacting space, ASCI only considers connections from the variational basis states that have sufficiently large wavefunction amplitudes. HCI uses a different selection criterion that allows it to exploit the fact that many Hamiltonian matrix elements are identical in magnitude; a presorting of these matrix elements (the two-electron repulsion integrals) enables fast and efficient identification of new basis states. In almost all selected CI calculations, once the variational space is suitably converged, a second-order perturbation theory (PT2) correction is added to the variational energy. Numerous recent studies have demonstrated their power: HCI was selected as the most accurate method among twenty for a study of transition metal atoms and their oxides [196], HCI was used to provide almost exact energies of the Gaussian-2 dataset [197], and both HCI and ASCI have been used in a recent comparative study of the ground-state energy of benzene [198].

A variety of selected CI approaches have been developed for vibrational problems [199–202], including a vibrational CIPSI [203] and a recent vibrational ASCI (VASCI) [204]. Motivated by HCI's strong performance and computational efficiency, in this work we present a vibrational HCI (VHCI). The differences between electronic and vibrational problems, especially their Hilbert spaces and Hamiltonian forms, necessitate a number of new developments in order for VHCI to enjoy the same advantages as electronic HCI; we describe these developments in Sec. 5.2. In Sec. 5.3, we present VHCI plus perturbation theory results for molecules containing between 12 and 48 degrees of freedom, calculating tens to hundreds of excited state energies for fourth- and sixth-order truncated potentials. By comparing to other literature results for these potentials, we demonstrate that VHCI is a highly accurate and efficient approach for large molecular systems with strong anharmonicity, typically achieving sub-wavenumber accuracy with modest computational resources.

5.2 Theory

5.2.1 Vibrational heat-bath configuration interaction

Expressed in terms of mass-weighted normal mode coordinates Q_i with frequencies ω_i, the nuclear Hamiltonian is given by

$$H = \frac{1}{2}\sum_{i=1}^{D}\left[-\frac{\partial^2}{\partial Q_i^2} + \omega_i^2 Q_i^2\right] + V_{\text{an}}(Q_1, Q_2, \ldots, Q_D), \tag{5.1}$$

where $D = 3N - 6$ is the number of normal mode degrees of freedom and V_{an} is the anharmonic part of the electronic ground state potential energy surface (PES). For comparison with previous works, here we neglect the Coriolis rotational coupling, but such a term can be straightforwardly included.

In vibrational HCI, we choose to work in the basis of Hartree product states $|\boldsymbol{n}\rangle = |n_1, n_2, \ldots, n_D\rangle$ formed from the harmonic oscillator orbitals $\phi_{n_i}(Q_i) = \langle Q_i | n_i \rangle$, leading to the wavefunction

$$|\Psi\rangle = \sum_{\boldsymbol{n}\in\mathcal{V}} c_{\boldsymbol{n}} \, |\boldsymbol{n}\rangle \, . \tag{5.2}$$

In VCI, the variational space $\mathcal{V}$ is commonly truncated by excitation level, for example by limiting the number of vibrational quanta per product state or per mode. However, this approach is not always efficient and may lead to a large Hilbert space with many product states that contribute minimally to the VCI solution. This issue of inefficient addition of states is addressed by selected VCI methods, which select states for inclusion in $\mathcal{V}$ by criteria other than excitation level as discussed in the Introduction, and here we focus on the HCI criterion.

We briefly recall that in the variational stage of HCI, basis state $|\boldsymbol{m}\rangle$ is added to $\mathcal{V}$ if $|H_{\boldsymbol{mn}} c_{\boldsymbol{n}}| \geq \varepsilon_1$, where ε_1 is a user-defined convergence parameter. In electronic structure, the matrix elements $H_{\boldsymbol{mn}}$ arising from double excitations depend only on the identity of the four orbitals involved. Therefore, many of the Hamiltonian matrix elements are identical in magnitude. This is not true in vibrational structure and the explicit enumeration and testing of connected $H_{\boldsymbol{mn}}$ matrix elements is

expensive. In order to devise an analogous VHCI screening criterion, we consider an approximate Hamiltonian $\tilde{H}$ obtained from a truncated normal mode expansion of the anharmonic part of the PES,

$$\begin{aligned} V_{\text{an}}(\boldsymbol{Q}) &= \sum_{i\le j\le k} V_{ijk} Q_i Q_j Q_k + \sum_{i\le j\le k\le l} V_{ijkl} Q_i Q_j Q_k Q_l + \dots \\ &= \sum_{i\le j\le k} W_{ijk} \bar{Q}_i \bar{Q}_j \bar{Q}_k + \sum_{i\le j\le k\le l} W_{ijkl} \bar{Q}_i \bar{Q}_j \bar{Q}_k \bar{Q}_l + \dots \end{aligned} \tag{5.3}$$

where the anharmonic force constants are partial derivatives of the PES, e.g. $V_{ijk} = (\partial^3 V_{\text{an}}/\partial Q_i \partial Q_j \partial Q_k)_{\boldsymbol{Q}=0}$. In the second line of Eq. (5.3), we define $\bar{Q}_i = (a_i^\dagger + a_i)$ and

$$W_{ijk\dots} = \frac{V_{ijk\dots}}{\sqrt{2^p \omega_i \omega_j \omega_k \dots}}, \tag{5.4}$$

where p is the order of the anharmonicity. We emphasize that while we limit ourselves to using $\tilde{H}$ throughout this study,cin principle this normal mode expansion is only necessary for the screening criterion used to identify important basis states; any representation of the anharmonic PES could be used for the subsequent evaluation of Hamiltonian matrix elements within this space.

To illustrate the diversity of nonzero Hamiltonian matrix elements, consider an anharmonic PES expanded to include cubic and quartic terms. The Hamiltonian matrix elements between product states $|\boldsymbol{m}\rangle$ and $|\boldsymbol{n}\rangle$ that differ in their occupancy by one quantum in mode i, by two quanta in modes i and j (including $i = j$), and so on, are given by

$$\tilde{H}^{(i)}_{\boldsymbol{mn}} = \sum_j W_{ijj} \langle \boldsymbol{m}| \bar{Q}_i \bar{Q}_j^2 |\boldsymbol{n}\rangle \tag{5.5a}$$

$$\tilde{H}^{(i,j)}_{\boldsymbol{mn}} = \sum_k W_{ijkk} \langle \boldsymbol{m}| \bar{Q}_i \bar{Q}_j \bar{Q}_k^2 |\boldsymbol{n}\rangle \tag{5.5b}$$

$$\tilde{H}^{(i,j,k)}_{\boldsymbol{mn}} = W_{ijk} \langle \boldsymbol{m}| \bar{Q}_i \bar{Q}_j \bar{Q}_k |\boldsymbol{n}\rangle \tag{5.5c}$$

$$\tilde{H}^{(i,j,k,l)}_{\boldsymbol{mn}} = W_{ijkl} \langle \boldsymbol{m}| \bar{Q}_i \bar{Q}_j \bar{Q}_k \bar{Q}_l |\boldsymbol{n}\rangle. \tag{5.5d}$$

The factors $\langle \boldsymbol{m}|\bar{Q}_i \ldots |\boldsymbol{n}\rangle$ that are not zero are products of terms of the form $\sqrt{n_i}$ and these factors are responsible for the differentiation of most matrix elements in the Hamiltonian, precluding an efficient evaluation of the usual HCI criterion. For example, if the product states $|\boldsymbol{m}\rangle$ and $|\boldsymbol{n}\rangle$ differ in the occupancy of three modes (i, j, k), then

$$\tilde{H}^{(i+,j+,k+)}_{\boldsymbol{mn}} = W_{ijk}\sqrt{m_i m_j m_k} \tag{5.6a}$$

$$\tilde{H}^{(i+,j+,k-)}_{\boldsymbol{mn}} = W_{ijk}\sqrt{m_i m_j n_k} \tag{5.6b}$$

$$\tilde{H}^{(i+,j-,k-)}_{\boldsymbol{mn}} = W_{ijk}\sqrt{m_i n_j n_k} \tag{5.6c}$$

and so on, where the notation indicates that the occupation of a given mode in $|\boldsymbol{m}\rangle$ is bigger or smaller than in $|\boldsymbol{n}\rangle$. Therefore, in addition to the *identity* of the modes with different occupations, the VCI matrix elements of a truncated PES depend on (1) whether the occupations are bigger/smaller on the bra/ket side, and (2) the overall excitation level. However, because these latter factors $\langle \boldsymbol{m}|\bar{Q}_i \ldots |\boldsymbol{n}\rangle$ are products of terms of the form $\sqrt{n_i}$, they are of order unity (at least when the excitation level is reasonably low) and can be reasonably neglected for the purpose of estimating the magnitude of the Hamiltonian matrix element. Doing so leads to a significant reduction in the number of unique numbers to be considered.

Specifically, let us define $W_i = \sum_j (2 + \delta_{ij}) W_{ijj}$ and $W_{ij} = \sum_k (2 + \delta_{jk} + \delta_{ij}\delta_{jk}) W_{ijkk}$, which approximately account for single and double mode excitations. Then, given an approximate wavefunction of the form (5.2) expanded over some space $\mathcal{V}$, we propose to add state $|\boldsymbol{m}\rangle$ to the variational space if $|\boldsymbol{m}\rangle$ and $|\boldsymbol{n}\rangle$ differ in their occupancy by one quantum in mode i, by two quanta in modes i and j (including $i = j$), and so on, and

$$\left|W_{ijk\ldots} c_{\boldsymbol{n}}\right| \geq \varepsilon_1. \tag{5.7}$$

The above criterion can be implemented very efficiently by pre-sorting the matrix elements $W_{ijk\ldots}$, of which there are at most a polynomial number, e.g. $O(D^4)$ for a quartic PES.

The ground-state VHCI algorithm is performed as follows:

1. Sort the list of $W_{ijk\ldots}$, largest to smallest.

2. Initialize the space $\mathcal{V}$ according to a small total number of quanta.

3. Build the Hamiltonian matrix in $\mathcal{V}$ and calculate its ground-state eigenvalue and eigenvector.

4. Add states to $\mathcal{V}$ via the criterion (5.7), as follows. For each state $|\boldsymbol{n}\rangle$, traverse the sorted list of $W_{ijk\ldots}$.

   (a) If $|W_i c_{\boldsymbol{n}}| \geq \varepsilon_1$, add all states $|\boldsymbol{m}\rangle$ that are included in $Q_i |\boldsymbol{n}\rangle$.

   (b) If $|W_{ij} c_{\boldsymbol{n}}| \geq \varepsilon_1$, add all states $|\boldsymbol{m}\rangle$ that are included in $Q_i Q_j |\boldsymbol{n}\rangle$.

   (c) If $|W_{ijk\ldots} c_{\boldsymbol{n}}| \geq \varepsilon_1$, add all states $|\boldsymbol{m}\rangle$ that are included in $Q_i Q_j Q_k \ldots |\boldsymbol{n}\rangle$. At anharmonic order p, there are $O(2^p)$ such states to add.

   (d) If $|W_{ijk\ldots} c_{\boldsymbol{n}}| < \varepsilon_1$, break and go on to the next $|\boldsymbol{n}\rangle$.

   Return to step 3 until the calculation is converged.

A number of possible convergence criteria can be devised; here, following the original HCI paper [192], we consider the calculation converged when the total number of states added in step 4 is less than 1% of the current number of variational states. Importantly, most elements of $\tilde{H}_{\boldsymbol{mn}}$ are zero due to the properties of harmonic oscillators; the states $|\boldsymbol{m}\rangle$ and $|\boldsymbol{n}\rangle$ can only differ by a few quanta, depending on the maximum anharmonic order of the PES. The same would not be true in the basis of product states obtained after a vibrational self-consistent field procedure [26, 173–177], which is why we intentionally work in the noninteracting normal mode basis. However, future work will be dedicated to the development of VHCI in alternative mean-field basis sets such as the one generated by the VSCF procedure.

Crucially, the presorting of scaled and/or summed anharmonic force constants ($W_i, W_{ij}, W_{ijk\ldots}$) combined with the criterion (5.7) means that *most states* $|\boldsymbol{m}\rangle$ *are never even tested for addition*. Just like in electronic structure theory, this construction is the key to the efficiency of VHCI. Unlike in electronic structure theory, the ground state of the vibrational Schrödinger equation, referred to

here as the zero-point energy (ZPE), is rarely of interest by itself. Following Ref. [193], we can straightforwardly modify the above VHCI algorithm to allow the simultaneous calculation of many excited states. In step 3, we find all eigenstates of interest (typically the N_s lowest in energy). Then we perform the addition step 4 for each of those states, combining all of their added basis states $|\boldsymbol{m}\rangle$ in the updated $\mathcal{V}$. Clearly, this adds many more basis states at each iteration, but many of them are duplicates and so the overall variational space is observed to grow sublinearly with N_s.

The above procedure can be applied based on an arbitrary-order expansion of the PES. However, high-order anharmonic interactions with repeated mode indices will contribute to lower-order excitations beyond the single and double excitations described in Eqs. (5.5a) and (5.5b) for the case of a quartic PES. For example, a sixth-order PES will yield triple excitations due to cubic anharmonicity *and* fifth-order anharmonicity (when a mode index is repeated), and similarly quadruple excitations due to quartic and sixth-order anharmonicity. In this work, we only test one sixth-order PES in Sec. 5.3.4; although we could define new effective force constants for the screening procedure, e.g. $W'_{ijk} = W_{ijk} + \sum_k W_{ijkll}$, instead we make the approximation $\sum_l W_{ijkll} \approx \max_l W_{ijkll}$. In other words, we allow fifth-order anharmonicities to propose triple excitations, but only based on the magnitude of individual anharmonic force constants and not the sum of all such constants contributing to a given triple excitation. Our testing suggests that the error incurred is negligible.

5.2.2 Epstein-Nesbet perturbation theory

To the variational energy of each state E_{var} we add the second-order perturbation theory (PT2) correction

$$\Delta E_2 \approx \sum_{\boldsymbol{m}}^{(\varepsilon_2)} \frac{\left(\sum_{\boldsymbol{n}} H_{\boldsymbol{mn}} c_{\boldsymbol{n}}\right)^2}{E_{\text{var}} - H_{\boldsymbol{mm}}}. \tag{5.8}$$

In exact PT2, the summation over $\boldsymbol{m}$ includes all basis states that are connected to the variational space $\mathcal{V}$. For large variational spaces, this perturbative space is enormous and the cost of the PT2 correction is prohibitive. To address this, HCI uses the same screening procedure as in the variational stage to efficiently include only the most important perturbative states [192]. For VHCI, we again use criterion (5.7), with a cutoff $\varepsilon_2 < \varepsilon_1$, to determine whether basis state $|\boldsymbol{m}\rangle$ should be

included in the perturbative space. When $\varepsilon_2 = 0$, the PT2 calculation is exact within the first-order interacting space.

Throughout this work, we calculate the PT2 correction deterministically as described above, which ultimately limits the size of the systems that we can accurately study. In the future we will pursue the stochastic or semistochastic evaluation of Eq. (5.8), as is now common practice in HCI [194], in order to study the vibrational structure of even larger systems.

5.3 Results

5.3.1 Software and simulation details

All simulations besides those on naphthalene were performed on a 4-core (8-thread) Intel Core i7-6700 3.4 GHz desktop CPU using up to 16 GB of RAM. Naphthalene calculations were performed on a cluster with up to two 12-core Intel Xeon Gold 6126 2.6 GHz CPUs and using up to 768 GB of RAM.

Our code is based on the Ladder Operator Vibrational Configuration Interaction package [205] with extensive modifications. Our VHCI code is available on GitHub [206]. The Hamiltonian matrix is stored in a sparse format using the Eigen linear algebra library [207]. The eigenvalues and eigenvectors of interest are calculated with the Lanczos algorithm as implemented in the SPECTRA linear algebra library [208]. We verified our code by comparing to the literature and to results obtained with the PyVCI software package [202].

All VHCI calculations were initialized with a basis of all states containing up to two vibrational quanta in order to ensure that two-quantum overtones and combination bands, which account for many of the low-lying target states, are present from the first iteration. Our preliminary testing indicates that using a larger initial basis does not qualitatively improve the convergence of the results.

In order to fairly and directly compare to previous works, we use the exact same PES as used in those works. Moreover, these previous works used truncated forms of the PES and thus the true Hamiltonian H used in the final calculations is the same as the approximate Hamiltonian $\tilde{H}$ used

Table 5.1. The twenty lowest-energy states from a calculation of the first 70 eigenstates of acetonitrile, with excitation energies given relative to the ZPE. Mode assignments are given based on the character of the basis state with the largest absolute CI coefficient, using mode-numbering from Ref. [183, 204]. We also include the total vibrational angular momentum superscript and symmetry label for each mode. VHCI results are shown for two different values of ε_1, which determines the number of variational basis states, $N_\mathcal{V}$, and shown with and without the PT2 correction to the energies ("Var" and "Full PT2", respectively). We compare to exact reference values from A-VCI [185] and to VASCI with full PT2 correction and $N_\mathcal{V}$ comparable to our $\varepsilon_1 = 1.0$ cm^{-1} case [204]. The maximum absolute error (Max. AE) and root mean squared error (RMSE) relative to A-VCI were calculated across all 70 states. All energies are in cm^{-1}.

Method:		$\varepsilon_1 = 1.0$		$\varepsilon_1 = 0.1$		VASCI	A-VCI
$N_\mathcal{V}$:		29 900		125 038		30 038	2 488 511
Assign.	Sym.	Var	Full PT2	Var	Full PT2	Full PT2	Var
ZPE		9837.43	9837.41	9837.41	9837.41	9837.41	9837.41
$\omega_{11}^{\pm1}$	E	361.01	360.99	360.99	360.99	361.01	360.99
		361.01	360.99	360.99	360.99	361.01	360.99
$2\omega_{11}^{\pm2}$	E	723.22	723.18	723.18	723.18	723.22	723.18
		723.25	723.19	723.18	723.18	723.23	723.18
$2\omega_{11}^{0}$	A_1	723.90	723.84	723.83	723.83	723.89	723.83
$\omega_{4}^{\pm1}$	A_1	900.70	900.66	900.66	900.66	900.68	900.66
$\omega_{9}^{\pm1}$	E	1034.18	1034.13	1034.13	1034.12	1034.14	1034.12
		1034.19	1034.13	1034.13	1034.12	1034.14	1034.13
$3\omega_{11}^{\pm3}$	A_1	1086.65	1086.56	1086.56	1086.55	1086.64	1086.55
$3\omega_{11}^{\pm3}$	A_2	1086.66	1086.56	1086.56	1086.55	1086.64	1086.55
$3\omega_{11}^{\pm1}$	E	1087.88	1087.79	1087.78	1087.78	1087.88	1087.77
		1087.88	1087.79	1087.78	1087.78	1087.88	1087.77
$\omega_4 + \omega_{11}^{\pm1}$	E	1259.89	1259.82	1259.81	1259.81	1259.86	1259.81
		1259.94	1259.83	1259.82	1259.81	1259.86	1259.81
ω_3	A_1	1389.10	1388.99	1388.98	1388.97	1388.99	1388.97
$\omega_{9}^{\pm1} + \omega_{11}^{\pm1}$	E	1394.86	1394.71	1394.69	1394.68	1394.76	1394.68
		1394.89	1394.71	1394.70	1394.68	1394.79	1394.68
$\omega_{9}^{\pm1} + \omega_{11}^{\mp1}$	A_2	1395.08	1394.93	1394.91	1394.90	1395.00	1394.90
$\omega_{9}^{\pm1} + \omega_{11}^{\mp1}$	A_1	1397.83	1397.70	1397.69	1397.68	1397.77	1397.68
Max. AE(70):		0.61	0.14	0.05	0.01	0.50	–
RMSE(70):		0.34	0.05	0.03	0.00	0.20	–

in the VHCI screening criterion. The truncation of the PES, neglect of Coriolis terms, and various levels of electronic structure theory used to parameterize the PES preclude direct comparison to experiment.

5.3.2 Acetonitrile: A standard benchmark

We first present results for acetonitrile, CH_3CN, a 6-atom, 12-dimensional system that has become one of the canonical benchmarks for new methods in vibrational structure theory [30,

184, 204, 209, 210]. We use the quartic PES described in Refs. [184, 211], for which normal mode frequencies were calculated using CCSD(T)/cc-pVTZ and higher-order force constants were calculated using B3LYP/cc-pVTZ. This PES was also used in highly accurate reference calculations [183, 212]. All PESs used in this study are available as input files on our GitHub repository [206].

We calculated the energies of the first 70 states of acetonitrile, of which the first 20 are reported in Table 5.1. Data for all 70 states can be found in the supplementary material. We compare our results to those obtained using A-VCI [212], which we consider to be numerically exact (similar to those obtained with the nonproduct quadrature approach [183]); for reference, the A-VCI results are obtained with approximately 2.5 million variational states. Mode assignments here and throughout indicate the character of the product state with the largest weight in the VCI eigenvector; for acetonitrile, we use the mode-numbering convention of Ref. [183, 204]. Because acetonitrile contains several degeneracies, we also include labels for the total vibrational angular momentum and symmetry group. To quantitatively assess the accuracy of our results, we report the maximum absolute error and the root mean squared error of the lowest 70 states. In addition to the numerically exact A-VCI results, we also compare to results obtained recently using VASCI [204], which is a selected CI technique that is similar in spirit to VHCI.

We report results for variational VHCI ("Var"), as well as VHCI+PT2 without VHCI screening of the perturbative space ("Full PT2"); these results are given for two values of the variational energy cutoff ε_1 that controls the number of variational states $N_{\mathcal{V}}$. Using $\varepsilon_1 = 1$ cm^{-1} results in a variational space with $N_{\mathcal{V}} = 29\,900$ basis states, which enables comparison to the largest reported VASCI calculation, with $N_{\mathcal{V}} = 30\,038$. We find that VHCI+PT2 achieves a maximum absolute error and a root mean squared error that is less than half that of VASCI, which is somewhat surprising because the CIPSI-style selection criterion used in VASCI is typically thought to more rigorously identify important states. However, the precise variational space generated by both VHCI and VASCI can be tuned by their parameters (ε_1 and the number of core/target states, respectively), so a direct comparison is not straightforward. In any event, the accuracy of VHCI is remarkable given

Table 5.2. The sixteen lowest-energy states from a calculation of the first 100 eigenstates of ethylene, with excitation energies given relative to the ZPE. Calculations were performed using fourth- and sixth-order truncations of the PES normal mode expansion. Both VHCI+PT2 calculations were converged with respect to variational and perturbative basis size. We compare to vDMRG[30] for both truncations and to VCI[202] with up to 8 quanta per product state for the sixth-order truncation. We also compare to a calculation from Ref. [213] which uses an untruncated version of the PES solved using VCI with a pruned basis set containing up to 13 quanta per product state. Assignments are given using the mode-numbering convention of Ref. [213]. All energies are in cm^{-1}.

PES:	Fourth-order		Sixth-order			Untruncated
Method:	VHCI+Full PT2	vDMRG	VHCI+PT2 ($\varepsilon_2 = 0.01$)	vDMRG	VCI (PyVCI)	Pruned VCI
Assign.	$\varepsilon_1 = 0.75$		$\varepsilon_1 = 0.5$		$N_{\text{tot}} = 8$	$N_{\text{tot}} = 13$
ZPE	11006.11	11006.19	11011.61	11016.15	11011.63	11014.91
ω_{10}	808.61	809.03	819.99	831.17	820.11	822.42
ω_8	914.87	915.29	926.33	933.47	926.45	934.29
ω_7	927.87	928.31	941.65	948.26	941.78	949.51
ω_4	1006.74	1007.13	1017.45	1018.26	1017.56	1024.94
ω_6	1216.94	1217.17	1222.16	1227.05	1222.23	1224.96
ω_3	1338.46	1338.87	1341.95	1343.46	1342.01	1342.96
ω_{12}	1429.93	1430.47	1438.31	1441.52	1438.39	1441.11
ω_2	1606.41	1622.11	1622.78	1629.04	–	1624.43
$2\omega_{10}$	1631.47	1625.56	1655.21	1682.18	–	1658.39
$\omega_8 + \omega_{10}$	1718.27	1722.77	1748.05	1770.02	–	1757.70
$\omega_7 + \omega_{10}$	1733.98	1729.53	1766.19	1786.99	–	1778.34
$\omega_4 + \omega_{10}$	1809.39	1810.47	1837.68	1852.60	–	1848.61
$2\omega_8$	1821.71	1826.01	1858.36	1878.42	–	1873.73
$\omega_7 + \omega_8$	1821.96	1827.96	1871.42	1886.16	–	1885.12
$2\omega_7$	1850.39	1852.23	1887.03	1906.02	–	1901.61

the modest computational cost; for example, the $\varepsilon_1 = 1$ cm^{-1} calculation reported here took less than 3 minutes for the variational stage and less than 6 minutes for the full PT2 correction (on an 8-core desktop CPU).

In Table 5.1, we also present results of a larger calculation with $\varepsilon_1 = 0.1$ cm^{-1}, resulting in $N_{\mathcal{V}} = 125\,038$. We obtain an extremely accurate spectrum even without the PT2 correction, with a maximum absolute error well below 0.1 cm^{-1}. This variational calculation took less than 30 minutes on the same 8-core desktop CPU. This larger calculation still benefits from minor corrections with PT2, which takes about 90 minutes and produces a spectrum in which no value differs from the exact result by more than 0.01 cm^{-1} across all 70 states. In summary, we have shown that VHCI can produce near-exact results for a 12-dimensional system with an extremely small computational effort.

5.3.3 Ethylene: Sixth-order potential

Next, we study ethylene, C_2H_4, which is the same size as acetonitrile (6 atoms, 12 dimensions), but here we use a more realistic *ab initio* potential energy surface and consider anharmonic expansions up to sixth order. Specifically, we use the PES of Ref. [213], which was calculated entirely using CCSD(T)/cc-pVQZ, and we use the PyPES software package [214] to convert from internal to cartesian normal mode coordinates and generate an anharmonic expansion up to sixth order. In contrast to the quartic PES of acetonitrile that contains 299 nonzero anharmonic force constants, this sixth-order PES for ethylene contains 2651 force constants, 2375 of which are fifth or sixth order. Here, we compare results and performance when the potential is truncated at fourth order and at sixth order. We calculated the first 100 states; results for the first sixteen states are shown in Table 5.2 and those for the additional 84 states can be found in the supplementary material.

Through testing, we confirmed that our VHCI+PT2 results are converged with $\varepsilon_1 = 0.75$ cm^{-1} for the quartic case (with full PT2) and $\varepsilon_1 = 0.5$ cm^{-1} for the sixth-order case (with $\varepsilon_2 = 0.01$ cm^{-1}), resulting in $N_\mathcal{V} = 153\,935$ and $161\,338$ basis states, respectively. In fact, it was not possible to go to larger variational spaces for the quartic case because of unphysical divergences in the truncated PES. Similar behavior of truncated PESs studied at high excitation levels has been observed before [202, 213, 215].

In Table 5.2, we also compare our results to those obtained with the vibrational density-matrix renormalization group (vDMRG) [30] using the same fourth- and sixth-order truncated PES. As discussed in the Introduction, DMRG and selected CI are similarly competitive methods in electronic structure theory. Surprisingly, we find that for both truncations, our energies are noticeably lower than the vDMRG results. For the quartic potential, our zero-point energy is 0.8 cm^{-1} lower than the vDMRG result, while for the sixth-order potential it is 4.5 cm^{-1} lower. Figure 5.1 shows the convergence of the ZPE as a function of the size of the variational space, $N_\mathcal{V}$. We see that VHCI (obtained with $N_\mathrm{s} = 1$) converges smoothly and quickly; for the fourth-order potential it exceeds the accuracy of vDMRG with about 5000 basis states. We also show results obtained with our own VCI code, which includes basis states according to their total number of vibrational

quanta. For both the fourth- and sixth-order potentials, VCI converges to the same ZPE as VHCI, although it requires significantly more basis states for comparable accuracy. The discrepancy with vDMRG may come from the latter using insufficient bond dimension, getting trapped in local minima during sweeps, or simply due to slight differences in the PES. As a check on the latter, we have also included in Table 5.2 the VCI excitation energies previously reported by the authors of the PyPES software package [202] from which the PES parameters were obtained. The results are in excellent agreement with our own VHCI+PT2 results, indicating that we are using the exact same PES as those authors.

In Fig. 5.1, we also plot the percent sparsity of the Hamiltonian matrix as function of number of variational basis states. We present the sparsity for VHCI (optimized for the ground state) and conventional VCI. For both the fourth-order and sixth-order potentials, VHCI produces a much sparser Hamiltonian matrix than VCI. These results indicate that VHCI is extremely effective at capturing the connectivity between important basis states (as demonstrated by the accurate ground-state energy) while also ignoring the connectivity to less important basis states (as demonstrated by the increased sparsity).

In the final column of Table 5.2, we also show results obtained in Ref. [213] using a pruned VCI basis with up to 13 vibrational quanta for the untruncated PES. As can be seen, the agreement improves significantly when going from the fourth-order PES to the sixth-order PES. For low-lying states, the disagreement at fourth order is on the order of 10-20 cm^{-1} and at sixth order is on the order of 5 cm^{-1}, indicating that the normal mode expansion is sensible and systematically improvable. Nonetheless, this error incurred due to the truncated potential is comparable to the difference in methods presented here, and thus future work will focus on incorporating more accurate representations of the potential into the VHCI method.

5.3.4 Ethylene oxide: Convergence and extrapolation

Next, we study ethylene oxide, C_2H_4O, a molecule with 7 atoms and 15 normal mode degrees of freedom. Compared to the two previous molecules, the three additional degrees of freedom

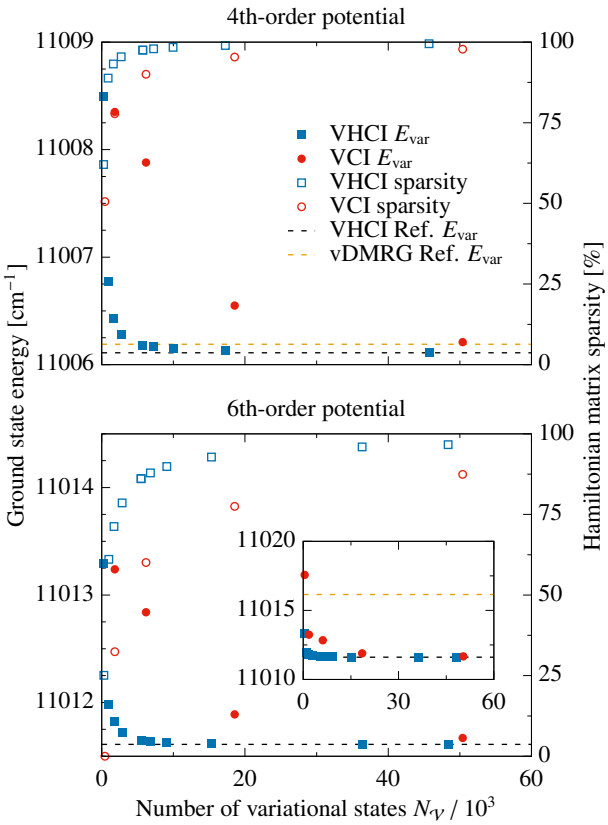

Figure 5.1. The variational ground-state energy of ethylene as a function of number of basis states $N_{\mathcal{V}}$. We compare the ground state energies of conventional VCI (solid red circles) and VHCI (solid blue squares) using a fourth-order (top) and sixth-order (bottom) truncation of the potential. VHCI calculations were performed by optimizing for the ground state ($N_s = 1$) and the VCI space was truncated by limiting the total number of quanta per product state. The blue dashed lines represent the converged VHCI ground-state energy, which we consider to be exact. The orange dashed lines are the vDMRG values from Ref. [30]. We also present the sparsity of the Hamiltonian matrix (right axis) as a function of $N_{\mathcal{V}}$ for conventional VCI (open red circles) and VHCI (open blue squares).

make numerically exact VCI calculations much more difficult. We use the quartic PES of Bégué et al.[216], with normal mode frequencies calculated at the CCSD(T)/cc-pVTZ level and anharmonic force constants calculated using B3LYP/6-31+G(d,p). We use the same version of the PES as Refs. [185, 204, 209, 210], which is available along with our source code on our GitHub repository [206]. Like acetonitrile, ethylene oxide represents a well-studied system that is suitable for benchmarking new approaches to solving the vibrational structure problem. In Table 5.3, we present results for the ten lowest and ten highest states from a VHCI calculation targeting $N_s = 200$ states. We performed the calculations with two different variational cutoff values $\varepsilon_1 = 2$ cm^{-1} and 1 cm^{-1}, producing variational spaces with 132 163 and 259 070 basis states, respectively. We present results with just the variational stage ("Var") and with heat-bath screened PT2 correction with $\varepsilon_2 = 0.01$ cm^{-1}.

On the left-hand side of Fig. 5.2 we plot the energy of the first, 50th, and 200th state with respect to the variational cutoff ε_1, for a variety of values of the perturbative screening parameter ε_2. We see that the curves with $\varepsilon_2 = 1$ cm^{-1}, 0.1 cm^{-1}, and 0.01 cm^{-1} agree very closely for all ε_1, with $\varepsilon_2 = 0.1$ cm^{-1} and 0.01 cm^{-1} being indistinguishable, confirming convergence with respect to ε_2. In Table 5.3 and Fig. 5.2, we compare our results to A-VCI calculations [185] that were obtained from an optimized variational space containing over 7 million basis states, which we take to be numerically exact. In Fig. 5.2, we see that all variational calculations tend monotonically toward the exact energies as ε_1 becomes small. Addition of the PT2 correction leads to more rapid convergence with respect to ε_1. For example, for the ground state we see that results obtained with $\varepsilon_1 = 20$ cm^{-1} and converged PT2 gives an answer that is closer to exact than that with $\varepsilon_1 = 5$ cm^{-1} and no PT2 correction. The benefits of perturbation theory become less pronounced in high-lying excited states, due to their large multiconfigurational character. In fact, for the 200th state, our calculation only produces the correct band assignment for $\varepsilon_1 \leq 1$ cm^{-1}. Table 5.3 shows the band assignment (obtained from the variational calculation) following the mode labeling convention of Ref. [185] and we leave the energy blank if we do not have an assignment that corresponds to the exact result. The 200th state is omitted for all methods except VHCI at $\varepsilon_1 = 1$ cm^{-1} and the A-VCI

Table 5.3. Ten lowest- and ten highest-energy states from the first 200 eigenstates of ethylene oxide, with excitation energies given relative to the ZPE. VHCI results are shown for two different values of ε_1 with no PT2 correction (Var) and with PT2 at $\varepsilon_2 = 0.01$ cm^{-1}. We also show the first 10 extrapolated energies obtained by a linear fit of E_{tot} vs. ΔE_2, as shown in Fig. 5.2. We compare all results to numerically exact reference values from A-VCI [185] and to VASCI with full PT2 correction and $N_{\mathcal{V}}$ roughly comparable to our $\varepsilon_1 = 2$ cm^{-1} case [204]. We report the maximum absolute error (Max. AE) and root mean squared error (RMSE) of the first 50 states for all methods. We show the same error metrics for all 200 states for VHCI with $\varepsilon_1 = 1$ cm^{-1} which is the only case for which all mode assignments match the exact result. Assignments use the mode-numbering convention of Ref. [185]. All energies are in cm^{-1}.

Method:	$\varepsilon_1 = 2.0$		$\varepsilon_1 = 1.0$		Linear ΔE_2	VASCI	A-VCI
$N_{\mathcal{V}}$:	132 163		259 070		Extrap.	150 000	7 118 214
Assign.	Var	$\varepsilon_2 = 0.01$	Var	$\varepsilon_2 = 0.01$	$\varepsilon_2 = 0.01$	Full PT2	Var
ZPE	12461.63	12461.50	12461.55	12461.48	12461.47	12461.6	12461.47
ω_1	793.11	792.73	792.88	792.69	792.65	792.8	792.63
ω_2	822.30	821.98	822.07	821.94	821.91	822.2	821.91
ω_3	878.62	878.33	878.41	878.30	878.28	878.4	878.27
ω_4	1017.70	1017.24	1017.42	1017.20	1017.15	1017.4	1017.14
ω_6	1121.87	1121.30	1121.53	1121.24	1121.19	1120.8	1121.17
ω_5	1124.37	1123.75	1124.00	1123.70	1123.65	1123.8	1123.62
ω_7	1146.42	1145.84	1146.08	1145.78	1145.73	1146.0	1145.72
ω_8	1148.68	1148.07	1148.31	1148.02	1147.97	1148.3	1147.96
ω_9	1271.43	1270.89	1271.06	1270.83	1270.78	1271.3	1270.78
$\omega_1 + \omega_5 + \omega_9$	3175.50	3170.13	3172.33	3169.19	–	3170.9	3167.97
$\omega_1 + \omega_6 + \omega_9$	3178.91	3173.60	3175.76	3172.68	–	3173.9	3171.53
$2\omega_4 + \omega_8$	3181.83	3177.51	3179.28	3176.82	–	3178.0	3175.93
$\omega_2 + \omega_3 + \omega_{11}$	3187.19	3182.12	3183.76	3181.06	–	3182.1	3180.16
$3\omega_1 + \omega_2$	3197.27	3191.75	3192.18	3187.44	–	3190.7	3184.85
$\omega_1 + \omega_8 + \omega_9$	3198.00	3189.61	3193.89	3190.78	–	3192.7	3189.65
$\omega_2 + \omega_5 + \omega_9$	3205.08	3200.30	3202.16	3199.48	–	–	3198.56
$\omega_2 + \omega_6 + \omega_9$	3206.11	3201.03	3202.96	3200.15	–	3200.9	3199.21
$\omega_1 + \omega_7 + \omega_9$	3210.44	3205.96	3207.74	3205.19	–	3206.7	3204.35
$2\omega_1 + 2\omega_2$	–	–	3218.48	3214.59	–	–	3212.77
Max AE(50):	4.00	0.98	2.09	0.50	0.06	2.2	–
RMSE(50):	2.40	0.51	1.22	0.26	0.03	0.8	–
Max. AE(200):	–	–	7.33	3.23	–	–	–
RMSE(200):	–	–	2.96	0.84	–	–	–
Core hours:	5.9	18.9	23.3	54.4	–	67.1	1756.4
Cores:	8	8	8	8	–	2	24

reference; several of the other ten highest excitations are also omitted from the VASCI results [204]. Because the incorrect band assignments of high-lying states prevents us from comparing level-by-level with exact results, we include statistics on just the first 50 states. Variational VHCI produces good agreement for the first 50 states, with a RMSE on the order of 1-2 cm^{-1} and maximum AE below 5 cm^{-1}; the addition of PT2 yields accuracy better than 1 cm^{-1} for both $\varepsilon_1 = 1$ cm^{-1} and 2 cm^{-1}. In comparison, VASCI+Full PT2 produces a maximum AE of 2.2 cm^{-1} and RMSE of

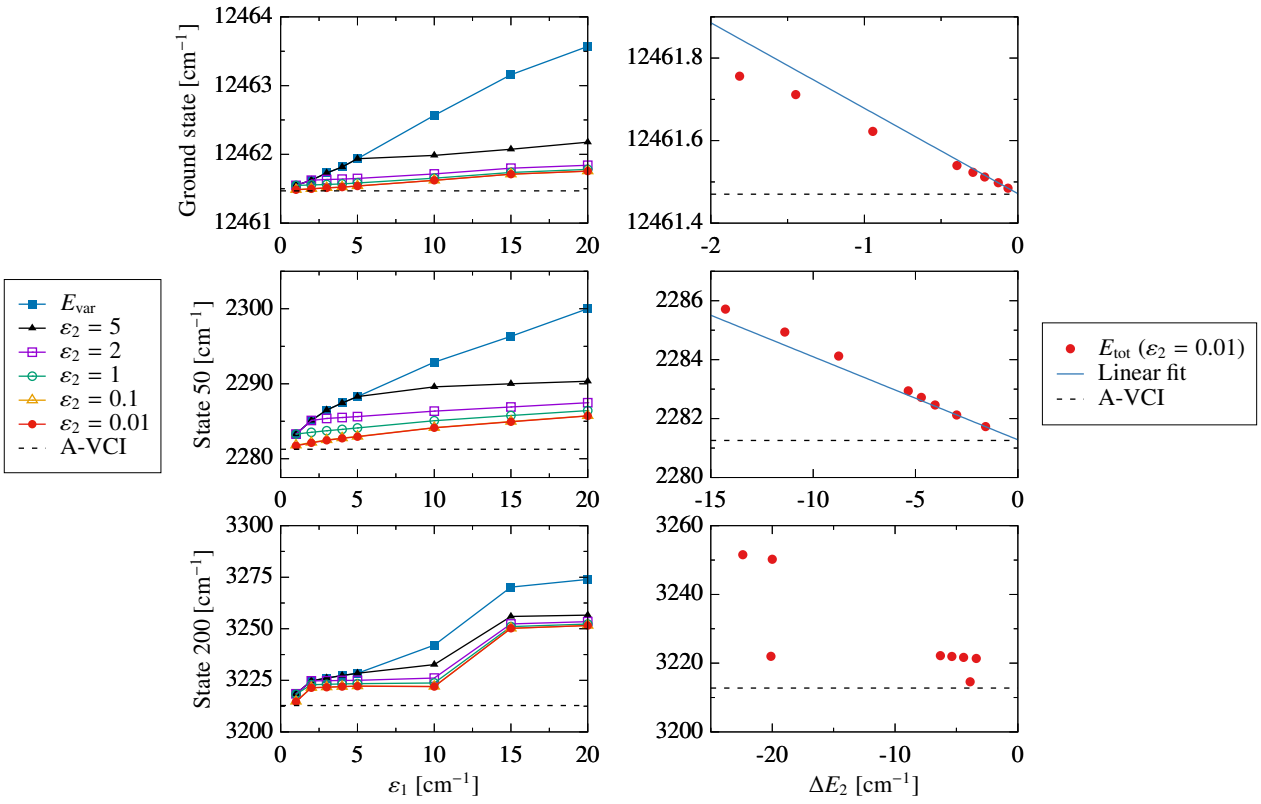

Figure 5.2. VHCI energy of the ground state (top row), the 50th state (middle row) and 200th state (bottom row) of ethylene oxide. The left-hand column shows the energy as a function of the variational heat-bath cutoff parameter ε_1 and includes the variational energy E_{var} (blue squares) and the total energy $E_{\text{tot}} = E_{\text{var}} + \Delta E_2$ for various values of the perturbative heat-bath screening parameter ε_2. The black dashed lines are the converged A-VCI values for each state, which can be considered to be exact. In the right-hand column, we present the total energy E_{tot} (red circles) with converged PT2 ($\varepsilon_2 = 0.01$ cm^{-1}) as a function of the perturbative correction ΔE_2. Note that we use a smaller y-range because the energy varies less with respect to ε_1 when the PT2 stage is converged. We also show the linear fits (blue lines) of the most accurate two points ($\varepsilon_1 = 1$ and 2 cm^{-1}) for the ground state and state 50, which were used to find the extrapolated energies presented in Table 5.3.

0.8 cm^{-1} for the first 50 levels compared to the exact results. All of the correct band assignments are present in the first 50 states of both VHCI and VASCI at $N_{\mathcal{V}} = 150\,000$, but the closely-spaced states 47 and 48 have the wrong energetic ordering for VASCI and for VHCI with $\varepsilon_1 = 2$ cm^{-1}. For $\varepsilon_1 = 1$ cm^{-1}, we obtain all 200 states with the correct assignments, enabling direct comparison to A-VCI. We see very good agreement over all states and VHCI+PT2 has a maximum AE around 3 cm^{-1} and RMSE below 1 cm^{-1}. Remarkably, this entire calculation took less than 7 hours on an 8-core desktop CPU. As a rough comparison to other methods, we also present the timings for all calculations in Table 5.3.

Finally, following standard HCI practice in electronic structure, we attempt to approximate the exact energies via extrapolation. On the right-hand side of Fig. 5.2, we plot the VHCI+PT2 energy of each state as a function of the PT2 correction ΔE_2 seeking to extrapolate to $\Delta E_2 = 0$, following Ref. [193]. We see that extrapolation is reasonable and successful for low-lying states, but not for high-lying states. In general, extrapolation of high-lying states is difficult because the level spacing becomes very small and the states are highly multiconfigurational, such that tracking a single level as ε_1 changes is challenging. We performed extrapolation for the first 50 states using a linear fit to results obtained with $\varepsilon_1 = 1$ cm^{-1} and 2 cm^{-1}, as shown graphically in the right-hand sides of Fig. 5.2 for the first and 50th states; we tested other polynomial fits and found linear extrapolation to be the simplest and best perfoming, although other schemes could be considered in the future. In Table 5.2, we present the extrapolated energies of the first ten states as well as the statistics of the first 50 states; all energies can be found in the supplementary material. The results are nearly exact, with a maximum AE below 0.1 cm^{-1} for all 50 states, and obviously require no additional computing effort. We conclude that linear extrapolation of high-quality VHCI+PT2 energies is a powerful way to achieve nearly exact energies for the ground state and many low-lying excited states.

5.3.5 Naphthalene: A 48-dimensional system

As a final test of VHCI, we consider naphthalene, $C_{10}H_8$, with 18 atoms and 48 normal modes, making it more than three times larger than any of the previous test systems. We use the quartic PES of Cané et al. [217], which was calculated at the B97-1/TZ2P level of theory, and includes 4125 nonzero anharmonic force constants. Large variational calculations were previously performed with this PES using the Hierarchical Intertwined Reduced-Rank Block Power Method (HI-RRBPM) [210]. We compare to the affordable HI-RRBPM (A) results and the most expensive HI-RRBPM (G) results, which we consider to be the most accurate. Finally, we compare to variational VASCI calculations from Ref. [204] with 1 million and 1.5 million basis states, obtained using 25 000 and 15 000 core states, respectively. Following Refs. [204, 210], we calculate

Table 5.4. Ten lowest- and ten highest-energy states from a calculation of the first 128 eigenstates of naphthalene, with excitation energies given relative to the ZPE. VHCI results are shown for two different values of ε_1 with no PT2 correction (Var) and with PT2 at $\varepsilon_2 = 0.2$ cm^{-1}. We compare to reference values from the smallest and largest HI-RRBPM calculations in Ref. [210] ("A" and "G" respectively) as well as to VASCI [204] with no PT2 correction and $N_\mathcal{V}$ similar to our $\varepsilon_1 = 1.5$ cm^{-1} case. Assignments are given using the mode-numbering convention of Ref. [217]. All energies are in cm^{-1}

Method:	$\varepsilon_1 = 1.5$		$\varepsilon_1 = 1.0$		VASCI		HI-RRBPM	
$N_\mathcal{V}$:	1 322 334		2 270 672		1 000 000	1 500 000	A	G
Assign.	Var	$\varepsilon_2 = 0.2$	Var	$\varepsilon_2 = 0.2$	Var	Var	Var	Var
ZPE	31772.71	31764.77	31769.90	31764.34	31774.4	31773.6	31782.20	31766.03
ω_{48}	168.17	165.20	166.89	164.63	166.4	166.3	165.84	164.60
ω_{13}	182.57	179.28	181.28	178.79	179.9	179.9	184.90	178.18
$2\omega_{48}$	335.22	329.48	333.17	328.69	336.4	336.1	338.21	329.41
$\omega_{13} + \omega_{48}$	349.25	342.84	346.48	341.76	349.5	349.4	365.68	342.02
ω_{24}	358.59	356.26	357.83	355.97	361.4	363.8	372.86	354.44
$2\omega_{13}$	362.91	357.23	360.75	356.49	363.4	366.6	397.32	357.66
ω_{16}	392.38	389.05	391.19	388.64	394.1	396.3	405.35	387.71
ω_{28}	468.62	464.50	467.08	463.93	470.9	475.3	468.20	463.47
ω_{47}	477.41	472.97	475.83	472.45	479.7	483.1	477.10	472.41
$3\omega_{48}$	503.57	493.98	499.45	492.38	502.5	501.8	506.60	495.50
$\omega_{13} + \omega_{23}$	978.99	972.19	976.88	971.60	991.6	1007.1	1091.20	974.99
$\omega_{24} + \omega_{36}$	982.41	977.49	981.37	977.64	1006.6	1015.4	1099.87	982.87
$\omega_{12} + \omega_{24}$	984.01	978.50	982.39	977.99	1002.2	1015.7	1100.56	985.06
$\omega_9 + \omega_{28}$	984.89	978.67	982.83	978.03	997.7	1010.7	1098.74	981.31
$\omega_{44} + \omega_{47}$	986.66	979.81	984.23	979.12	1001.8	1013.3	1106.07	987.92
$\omega_9 + \omega_{47}$	993.93	987.08	991.49	986.44	–	–	1121.57	994.66
ω_{35}	1013.18	1008.63	1011.79	1008.21	–	–	1134.08	1011.99
$\omega_{16} + \omega_{36}$	1017.62	1011.96	1015.91	1011.51	–	–	1138.09	1013.55
$2\omega_{44}$	1017.51	1012.86	1016.19	1012.70	–	–	1138.46	1015.09
$\omega_9 + \omega_{44}$	1024.79	1020.17	1023.43	1019.82	–	–	1148.79	1018.96
Max AE(25):	11.78	2.85	6.32	3.69	16.1	–	54.64	–
RMSE(25):	6.62	1.35	4.18	1.68	9.0	–	30.44	–
Core hours:	1234.4	2088.0	2620.8	3874.8	1584.7	1834.9	1167.4	63590.4
Cores:	20	20	20	20	40	40	128	64

the 128 lowest states of naphthalene, of which the ten lowest and ten highest are presented in Table 5.4; results for all states can be found in the supplementary material. We show results with VHCI variational cutoff values $\varepsilon_1 = 1.5$ cm^{-1} and 1 cm^{-1}, producing approximately 1.3 million and 2.3 million basis states, respectively. Although a fully converged PT2 correction is intractable, we calculate an approximate PT2 correction with heat-bath screening; we used $\varepsilon_2 = 0.2$ cm^{-1}, producing a perturbative space containing approximately 15 million states.

For low-lying states, the agreement between variational VHCI and HI-RRBPM (G) is very good. At comparable computational cost, the accuracy of variational VASCI and VHCI is similar.

The PT2 correction to VHCI produces a significant improvement of low-lying energies, which now match HI-RRBPM (G) to an accuracy of about 1 cm^{-1}.

We calculated the maximum absolute error and RMSE with respect to HI-RRBPM for the first 25 eigenstates. We matched the states to Ref. [210] and Ref. [204] according to their mode assignments. Variational VHCI achieves marginally closer agreement to the large HI-RRBPM(G) calculation than VASCI. Perturbation theory provides a noticeable improvement over the variational result. Curiously, VHCI+PT2 produces a more accurate result for the smaller variational space, indicating that the calculation is probably not converged with respect to ε_2. Indeed, ideally the PT2 correction should be calculated with $\varepsilon_2 \ll \varepsilon_1$, but even $\varepsilon_2 = 0.2$ cm^{-1} produces an accurate result for low-lying states. As a convergence test, we also performed a large VHCI calculation that optimizes only the ground state (not shown), and obtained a variational ZPE that is at least 4 cm^{-1} lower than the HI-RRBPM (G) answer; therefore, some of our VHCI results that are lower than HI-RRBPM (G) may actually be more accurate, which would explain some of the discrepancies seen in the comparison.

For the high-lying states, which are much harder to converge as we discussed above, we only present results for those states that match the mode assignment from HI-RRBPM (G) and we do not attempt to calculate error statistics. For states with matching assignments, we see good agreement between variational VHCI and HI-RRBPM (G), especially at $\varepsilon_1 = 1$ cm^{-1}. The PT2 correction is not as helpful for high-lying states as it is for low-lying ones, because the variational space of the low-lying states is tightly converged and additional corrections are well-captured by perturbation theory. In some cases, the PT2 correction worsens the agreement with HI-RRBPM (G), although this may be a result of an incorrect mode assignment inside a dense spectrum of excited states. We do not attempt any extrapolation because $\varepsilon_2 = 0.2$ cm^{-1} is not small enough to converge the PT2 correction; a stochastic PT2 implementation [194] would be clearly beneficial. Overall, we are confident that the eigenvalue spectrum obtained from our VHCI calculations is accurate enough to be useful in real-world applications. Comparison of the overall CPU times, presented at the bottom of Table 5.4, underscores the competitiveness of VHCI as a means of accurately solving

the vibrational Schrödinger equation on high-dimensional anharmonic potentials.

5.4 Conclusions

We have introduced vibrational heat-bath configuration interaction based on the original principles of HCI [192], but with adaptations for vibrational Hamiltonians. VHCI+PT2 performed well on our four test molecules, achieving quantitative accuracy for the 12-dimensional systems acetonitrile and ethylene, while outperforming VASCI and vDMRG. VHCI also performed well on larger systems, especially for low-lying states. High-lying states are a challenge due to their highly multi-configurational character and dense energetic spacing. Convergence of high-lying states could be improved by implementing a state-specific algorithm [199–201].

In future work, the implementation of semistochastic PT2 [193–195] will be critical for studying even larger systems. Extension of VHCI to alternative representations of the PES will be needed in order to eliminate error due to truncation and allow direct comparison to experiment; the efficiency of the algorithm in this context remains to be seen. Additionally, work is in progress to use VSCF single-mode basis functions within VHCI, which should greatly reduce the size of the configuration space needed to converge the variational stage. Furthermore, VHCI can be straightforwardly extended to efficiently calculate spectroscopic intensities based on the dipole moment surface [201, 218, 219]. Consideration of spectroscopic activity can also be used to target eigenstates more efficiently, as recently implemented in A-VCI [220]. Finally, it will be interesting to apply VHCI to more strongly anharmonic systems, such as molecular clusters [27, 221] or floppy molecules [177, 222, 223], where truncated expansions of the PES will not be sufficient.

References

[1] G. D. Scholes, G. R. Fleming, L. X. Chen, A. Aspuru-Guzik, A. Buchleitner, D. F. Coker, G. S. Engel, R. van Grondelle, A. Ishizaki, D. M. Jonas, J. S. Lundeen, J. K. McCusker, S. Mukamel, J. P. Ogilvie, A. Olaya-Castro, M. A. Ratner, F. C. Spano, K. B. Whaley, and X. Zhu, "Using coherence to enhance function in chemical and biophysical systems," Nature, vol. 543, no. 7647, pp. 647–656, 2017.

[2] S. Mukamel, Principles of Nonlinear Optical Spectroscopy. Oxford University Press, 1995.

[3] T. Brixner, J. Stenger, H. M. Vaswani, M. Cho, R. E. Blankenship, and G. R. Fleming, "Two-dimensional spectroscopy of electronic couplings in photosynthesis," Nature, vol. 434, no. 7033, pp. 625–628, 2005.

[4] G. S. Engel, T. R. Calhoun, E. L. Read, T.-K. Ahn, T. T. Mancal, Y.-C. Cheng, R. E. Blankenship, and G. R. Fleming, "Evidence for wavelike energy transfer through quantum coherence in photosynthetic systems," Nature, vol. 446, no. Copyright (C) 2012 American Chemical Society (ACS). All Rights Reserved. Pp. 782–786, 2007.

[5] R. Tempelaar, T. L. C. Jansen, and J. Knoester, "Vibrational Beatings Conceal Evidence of Electronic Coherence in the FMO Light-Harvesting Complex," J. Phys. Chem. B, vol. 118, no. 45, pp. 12 865–12 872, 2014.

[6] H.-P. Breuer and F. Petruccione, The Theory of Open Quantum Systems. Oxford University Press, 2007.

[7] A. Ishizaki and G. R. Fleming, "On the adequacy of the Redfield equation and related approaches to the study of quantum dynamics in electronic energy transfer," J. Chem. Phys., vol. 130, no. 23, p. 234 110, 2009.

[8] V. May and O. Kühn, Charge and Energy Transfer Dynamics in Molecular Systems. Weinheim, Germany: Wiley-VCH Verlag GmbH & Co. KGaA, 2011, pp. 213–261, ISBN: 9783527633791.

[9] R. A. Marcus, "On the Theory of Oxidation-Reduction Reactions Involving Electron Transfer. I," J. Chem. Phys., vol. 24, no. 5, pp. 966–978, 1956.

[10] J. C. Tully and R. K. Preston, "Trajectory surface hopping approach to nonadiabatic molecular collisions: The reaction of h+ with d2," The Journal of Chemical Physics, vol. 55, no. 2, pp. 562–572, 1971.

[11] J. C. Tully, "Molecular dynamics with electronic transitions," The Journal of Chemical Physics, vol. 93, no. 2, pp. 1061–1071, 1990.

[12] Y Tanimura and R. K. Kubo, "Time Evolution of a Quantum System in Contact with a Nearly Gaussian-Markoffian Noise Bath," J. Phys. Soc. Jpn., vol. 58, no. 1, p. 101, 1989.

[13] A. Ishizaki and G. R. Fleming, "Unified treatment of quantum coherent and incoherent hopping dynamics in electronic energy transfer: reduced hierarchy equation approach," J. Chem. Phys., vol. 130, no. 23, p. 234 111, 2009.

[14] I. S. Dunn, R. Tempelaar, and D. R. Reichman, "Removing instabilities in the hierarchical equations of motion: Exact and approximate projection approaches," J. Chem. Phys., vol. 150, no. 18, p. 184 109, 2019.

[15] V. Coropceanu, J. Cornil, D. A. da Silva Filho, Y. Olivier, R. Silbey, and J. L. Brédas, "Charge transport in organic semiconductors," Chem. Rev., vol. 107, no. 4, pp. 926–952, 2007.

[16] T. Nematiaram and A. Troisi, "Strategies to reduce the dynamic disorder in molecular semiconductors," Mater. Horizons, vol. 7, no. 11, pp. 2922–2928, 2020.

[17] G. D. Mahan, Many-Particle Physics, 12. Boston, MA: Springer US, 2000, vol. 58, pp. 7250–7257, ISBN: 978-1-4419-3339-3.

[18] T. Holstein, "Studies of polaron motion," Ann. Phys. (N. Y)., vol. 8, no. 3, pp. 325–342, 1959.

[19] A. Troisi and G. Orlandi, "Charge-transport regime of crystalline organic semiconductors: Diffusion limited by thermal off-diagonal electronic disorder," Phys. Rev. Lett., vol. 96, no. 8, p. 086 601, 2006.

[20] S. Fratini and S. Ciuchi, "Bandlike motion and mobility saturation in organic molecular semiconductors," Phys. Rev. Lett., vol. 103, no. 26, p. 266 601, 2009.

[21] S. Fratini, D. Mayou, and S. Ciuchi, "The Transient Localization Scenario for Charge Transport in Crystalline Organic Materials," Adv. Funct. Mater., vol. 26, no. 14, pp. 2292–2315, 2016.

[22] A. Girlando, L. Grisanti, M. Masino, I. Bilotti, A. Brillante, R. G. Della Valle, and E. Venuti, "Peierls and Holstein carrier-phonon coupling in crystalline rubrene," Phys. Rev. B, vol. 82, no. 3, p. 035 208, 2010.

[23] P. Ordejón, D. Boskovic, M. Panhans, and F. Ortmann, "Ab initio study of electron-phonon coupling in rubrene," Phys. Rev. B, vol. 96, no. 3, p. 035 202, 2017.

[24] O. Christiansen, "Møller-Plesset perturbation theory for vibrational wave functions," J. Chem. Phys., vol. 119, no. 12, pp. 5773–5781, 2003.

[25] V. Barone, "Anharmonic vibrational properties by a fully automated second-order perturbative approach," J. Chem. Phys., vol. 122, no. 1, 2005.

[26] S. Carter, J. M. Bowman, and N. C. Handy, "Extensions and tests of "multimode": a code to obtain accurate vibration/rotation energies of many-mode molecules," Theor. Chem. Accounts Theory, Co vol. 100, no. 1-4, pp. 191–198, 1998.

[27] Q. Yu and J. M. Bowman, "Classical, Thermostated Ring Polymer, and Quantum VSCF/VCI Calculations of IR Spectra of H 7 O 3 + and H 9 O 4 + (Eigen) and Comparison with Experiment," J. Phys. Chem. A, vol. 123, no. 7, pp. 1399–1409, 2019.

[28] J. M. Bowman, K. Christoffel, and F. Tobin, "Application of SCF-SI theory to vibrational motion in polyatomic molecules," J. Phys. Chem., vol. 83, no. 8, pp. 905–920, 1979.

[29] O. Christiansen, "Vibrational coupled cluster theory," J. Chem. Phys., vol. 120, no. 5, pp. 2149–2159, 2004.

[30] A. Baiardi, C. J. Stein, V. Barone, and M. Reiher, "Vibrational Density Matrix Renormalization Group," J. Chem. Theory Comput., vol. 13, no. 8, pp. 3764–3777, 2017.

[31] J. H. Fetherolf and T. C. Berkelbach, "Linear and nonlinear spectroscopy from quantum master equations," J. Chem. Phys., vol. 147, no. 24, p. 244 109, 2017.

[32] C. H. Mak and D. Chandler, "Solving the sign problem in quantum Monte Carlo dynamics," Phys. Rev. A, vol. 41, no. 10, pp. 5709–5712, 1990.

[33] D. E. Makarov and N. Makri, "Path integrals for dissipative systems by tensor multiplication. Condensed phase quantum dynamics for arbitrarily long time," Chem. Phys. Lett., vol. 221, no. 5-6, pp. 482–491, 1994.

[34] M Beck, A Jackle, G. A. Worth, and H.-D. Meyer, "The multiconfiguration time-dependent Hartree (MCTDH) method: a highly efficient algorithm for propagating wavepackets," Phys. Rep., vol. 324, no. 1, pp. 1–105, 2000.

[35] M. Thoss, H. Wang, and W. H. Miller, "Self-consistent hybrid approach for complex systems: Application to the spin-boson model with Debye spectral density," J. Chem. Phys., vol. 115, no. 7, p. 2991, 2001.

[36] E. R. Dunkel, S. Bonella, and D. F. Coker, "Iterative linearized approach to nonadiabatic dynamics," J. Chem. Phys., vol. 129, no. 11, p. 114 106, 2008.

[37] H.-T. Chen, G. Cohen, and D. R. Reichman, "Inchworm Monte Carlo for exact nonadiabatic dynamics. I. Theory and algorithms," J. Chem. Phys., vol. 146, no. 5, p. 054 105, 2017.

[38] J. D. Hybl, A. W. Albrecht, S. M. Gallagher Faeder, and D. M. Jonas, "Two-dimensional electronic spectroscopy," Chem. Phys. Lett., vol. 297, no. 3-4, pp. 307–313, 1998.

[39] S Mukamel, "Multidimensional femtosecond correlation spectroscopies of electronic and vibrational excitations.," Annu. Rev. Phys. Chem., vol. 51, no. 11, pp. 691–729, 2000.

[40] D. M. Jonas, "Two-dimensional femtosecond spectroscopy.," Annu. Rev. Phys. Chem., vol. 54, pp. 425–463, 2003.

[41] S. Jang, Y. C. Cheng, D. R. Reichman, and J. D. Eaves, "Theory of coherent resonance energy transfer," J. Chem. Phys., vol. 129, p. 101 104, 2008.

[42] M. B. Plenio and S. F. Huelga, "Dephasing-assisted transport: Quantum networks and biomolecules," New J. Phys., vol. 10, p. 113 019, 2008.

[43] M. Mohseni, P. Rebentrost, S. Lloyd, and A. Aspuru-Guzik, "Environment-assisted quantum walks in photosynthetic energy transfer," J. Chem. Phys., vol. 129, no. 17, p. 174 106, 2008.

[44] P. Huo and D. F. Coker, "Iterative linearized density matrix propagation for modeling coherent excitation energy transfer in photosynthetic light harvesting," J. Chem. Phys., vol. 133, p. 184 108, 2010.

[45] J. Wu, F. Liu, Y. Shen, J. Cao, and R. J. Silbey, "Efficient energy transfer in light-harvesting systems, I: Optimal temperature, reorganization energy and spatial-temporal correlations," New J. Phys., vol. 12, p. 105 012, 2010.

[46] A. Kolli, A. Nazir, and A. Olaya-Castro, "Electronic excitation dynamics in multichromophoric systems described via a polaron-representation master equation," J. Chem. Phys., vol. 135, no. 15, p. 154 112, 2011.

[47] V. Tiwari, W. K. Peters, and D. M. Jonas, "Electronic resonance with anticorrelated pigment vibrations drives photosynthetic energy transfer outside the adiabatic framework," Proc. Natl. Acad. Sci., vol. 110, no. 4, pp. 1203–1208, 2013.

[48] R. Kubo, "A stochastic theory of line shape," Adv. Chem. Phys., vol. 15, no. 1, p. 101, 1969.

[49] S. A. Egorov, K. F. Everitt, and J. L. Skinner, "Quantum Dynamics and Vibrational Relaxation," J. Phys. Chem. A, vol. 103, no. 47, pp. 9494–9499, 1999.

[50] S. A. Egorov, E Rabani, and B. J. Berne, "On the adequacy of mixed quantum-classical dynamics in condensed phase systems," J. Phys. Chem. B, vol. 103, no. 50, pp. 10 978–10 991, 1999.

[51] J. L. Skinner and D. Hsu, "Pure dephasing of a two-level system," J. Phys. Chem., vol. 90, no. 21, pp. 4931–4938, 1986.

[52] D. Reichman, R. J. Silbey, and A. Suárez, "On the nonperturbative theory of pure dephasing in condensed phases at low temperatures," J. Chem. Phys., vol. 105, no. 23, pp. 10 500–10 506, 1996.

[53] F. Shibata, Y. Takahashi, and N. Hashitsume, "A generalized stochastic liouville equation. Non-Markovian versus memoryless master equations," J. Stat. Phys., vol. 17, no. 4, pp. 171–187, 1977.

[54] S. Chaturvedi and F. Shibata, "Time-convolutionless projection operator formalism for elimination of fast variables. Applications to Brownian motion," Z. Phys. B Condens. Matter, vol. 35, no. 3, pp. 297–308, 1979.

[55] B Yoon, J. M. Deutch, and J. H. Freed, "A comparison of generalized cumulant and projection operator methods in spin-relaxation theory," J. Chem. Phys., vol. 62, no. 1975, p. 4687, 1975.

[56] S. Mukamel, I. Oppenheim, and J. Ross, "Statistical reduction for strongly driven simple quantum systems," Phys. Rev. A, vol. 17, no. 6, pp. 1988–1998, 1978.

[57] M. Lax, "Formal theory of quantum fluctuations from a driven state," Phys. Rev., vol. 129, no. 5, pp. 2342–2348, 1963.

[58] P. Gardiner and P. Zoller, Quantum Noise. Springer-Verlag, Berlin, 2004.

[59] G. W. Ford and R. O'Connell, "There is No Quantum Regression Theorem," Phys. Rev. Lett., vol. 77, no. 5, pp. 798–801, 1996.

[60] S Swain, "Master equation derivation of quantum regression theorem," J. Phys. A. Math. Gen., vol. 14, no. 10, pp. 2577–2580, 1999.

[61] D. Alonso and I. de Vega, "Multiple-time correlation functions for non-markovian interaction: Beyond the quantum regression theorem," Phys. Rev. Lett., vol. 94, no. 20, pp. 1–4, 2005.

[62] D. Alonso and I. de Vega, "Hierarchy of equations of multiple-time correlation functions," Phys. Rev. A - At. Mol. Opt. Phys., vol. 75, no. 5, p. 052 108, 2007.

[63] H. S. Goan, P. W. Chen, and C. C. Jian, "Non-Markovian finite-temperature two-time correlation functions of system operators: Beyond the quantum regression theorem," J. Chem. Phys., vol. 134, no. 12, 2011.

[64] N. Gisin, "Time Correlations and Heisenberg Picture in the Quantum State Diffusion Model of Open Systems," J. Mod. Opt., vol. 40, no. 12, pp. 2313–2319, 1993.

[65] A. Montoya-Castillo, T. C. Berkelbach, and D. R. Reichman, "Extending the applicability of Redfield theories into highly non-Markovian regimes," J. Chem. Phys., vol. 143, p. 194 198, 2015.

[66] S. Valleau, A. Eisfeld, and A. Aspuru-Guzik, "On the alternatives for bath correlators and spectral densities from mixed quantum-classical simulations," J. Chem. Phys., vol. 137, no. 22, p. 224 103, 2012.

[67] M. K. Lee and D. F. Coker, "Modeling Electronic-Nuclear Interactions for Excitation Energy Transfer Processes in Light-Harvesting Complexes," J. Phys. Chem. Lett., vol. 7, no. 16, pp. 3171–3178, 2016.

[68] T. C. Berkelbach, D. R. Reichman, and T. E. Markland, "Reduced density matrix hybrid approach: an efficient and accurate method for adiabatic and non-adiabatic quantum dynamics.," J. Chem. Phys., vol. 136, no. 3, p. 034 113, 2012.

[69] T. C. Berkelbach, T. E. Markland, and D. R. Reichman, "Reduced density matrix hybrid approach: application to electronic energy transfer.," J. Chem. Phys., vol. 136, no. 8, p. 084 104, 2012.

[70] L. E. Fried and S. Mukamel, "Simulation of nonlinear electronic spectroscopy in the condensed phase," in Advances in Chemical Physics. John Wiley & Sons, Ltd, 1993, pp. 435–516.

[71] A. Ishizaki and Y. Tanimura, "Quantum dynamics of system strongly coupled to low-temperature colored noise bath: Reduced hierarchy equations approach," J. Phys. Soc. Japan, vol. 74, no. 12, pp. 3131–3134, 2005.

[72] R.-X. Xu and Y. Yan, "Dynamics of quantum dissipation systems interacting with bosonic canonical bath: Hierarchical equations of motion approach," Phys. Rev. E, vol. 75, p. 031 107, 2007.

[73] Pyrho: A python package for reduced density matrix techniques, `https://github.com/berkelbach-group/pyrho`.

[74] A. Ishizaki and Y. Tanimura, "Nonperturbative non-Markovian quantum master equation: Validity and limitation to calculate nonlinear response functions," Chem. Phys., vol. 347, no. 1-3, pp. 185–193, 2008.

[75] R. X. Xu, P. Cui, X. Q. Li, Y. Mo, and Y. Yan, "Exact quantum master equation via the calculus on path integrals," J. Chem. Phys., vol. 122, no. 4, p. 041 103, 2005.

[76] M. Xu, L. Song, K. Song, and Q. Shi, "Convergence of high order perturbative expansions in open system quantum dynamics," J. Chem. Phys., vol. 146, no. 6, p. 064 102, 2017.

[77] L. Chen, R. Zheng, Q. Shi, and Y. Yan, "Optical line shapes of molecular aggregates: Hierarchical equations of motion method," J. Chem. Phys., vol. 131, no. 9, p. 094 502, 2009.

[78] L. Chen, R. Zheng, Q. Shi, and Y. Yan, "Two-dimensional electronic spectra from the hierarchical equations of motion method: Application to model dimers.," J. Chem. Phys., vol. 132, no. 2, p. 024 505, 2010.

[79] P. Zoller, M. Marte, and D. Walls, "Quantum jumps in atomic systems," Phys. Rev. A, vol. 35, no. 1, pp. 198–207, 1987.

[80] N. Gisin and I. C. Percival, "The quantum-state diffusion model applied to open systems," J. Phys. A. Math. Gen., vol. 25, no. 21, pp. 5677–5691, 1992.

[81] H. J. Carmichael, "Quantum trajectory theory for cascaded open systems," Phys. Rev. Lett., vol. 70, no. 15, pp. 2273–2276, 1993.

[82] J. H. Fetherolf, D. Golež, and T. C. Berkelbach, "A Unification of the Holstein Polaron and Dynamic Disorder Pictures of Charge Transport in Organic Crystals," Phys. Rev. X, vol. 10, no. 2, p. 021 062, 2020.

[83] S. R. Forrest, "The path to ubiquitous and low-cost organic electronic appliances on plastic," Nature, vol. 428, no. 6986, pp. 911–918, 2004.

[84] M. Muccini, "A bright future for organic field-effect transistors," Nat. Mater., vol. 5, no. 8, pp. 605–613, 2006.

[85] H. Sirringhaus, "25th Anniversary Article: Organic Field-Effect Transistors: The Path Beyond Amorphous Silicon," Adv. Mater., vol. 26, no. 9, pp. 1319–1335, 2014.

[86] M. E. Gershenson, V. Podzorov, and A. F. Morpurgo, "Colloquium: Electronic transport in single-crystal organic transistors," Rev. Mod. Phys., vol. 78, no. 3, pp. 973–989, 2006.

[87] V. Podzorov, E. Menard, A. Borissov, V. Kiryukhin, J. A. Rogers, and M. E. Gershenson, "Intrinsic charge transport on the surface of organic semiconductors," Phys. Rev. Lett., vol. 93, no. 8, p. 086 602, 2004.

[88] V. Podzorov, E. Menard, J. A. Rogers, and M. E. Gershenson, "Hall effect in the accumulation layers on the surface of organic semiconductors," Phys. Rev. Lett., vol. 95, no. 22, p. 226 601, 2005.

[89] O. D. Jurchescu, J. Baas, and T. T. M. Palstra, "Effect of impurities on the mobility of single crystal pentacene," Appl. Phys. Lett., vol. 84, no. 16, pp. 3061–3063, 2004.

[90] H. Sirringhaus, T. Sakanoue, and J.-F. Chang, "Charge-transport physics of high-mobility molecular semiconductors," Phys. status solidi, vol. 249, no. 9, pp. 1655–1676, 2012.

[91] N Karl, "Charge carrier transport in organic semiconductors," Synthetic Met., vol. 133-134, pp. 649–657, 2003.

[92] V. M. Kenkre, "Finite-bandwidth calculations for charge carrier mobility in organic crystals," Phys. Lett. A, vol. 305, no. 6, pp. 443–447, 2002.

[93] G. De Filippis, V. Cataudella, A. De Candia, A. S. Mishchenko, and N. Nagaosa, "Alternative representation of the Kubo formula for the optical conductivity: A shortcut to transport properties," Phys. Rev. B, vol. 90, no. 1, p. 014 310, 2014.

[94] N.-E. Lee, J.-J. Zhou, L. A. Agapito, and M. Bernardi, "Charge transport in organic molecular semiconductors from first principles: The bandlike hole mobility in a naphthalene crystal," Phys. Rev. B, vol. 97, no. 11, p. 115 203, 2018.

[95] H. Geng, Q. Peng, L. Wang, H. Li, Y. Liao, Z. Ma, and Z. Shuai, "Toward quantitative prediction of charge mobility in organic semiconductors: Tunneling enabled hopping model," Adv. Mater., vol. 24, no. 26, pp. 3568–3572, 2012.

[96] G. Nan, X. Yang, L. Wang, Z. Shuai, and Y. Zhao, "Nuclear tunneling effects of charge transport in rubrene, tetracene, and pentacene," Phys. Rev. B, vol. 79, no. 11, p. 115 203, 2009.

[97] L. Wang, Q. Li, Z. Shuai, L. Chen, and Q. Shi, "Multiscale study of charge mobility of organic semiconductor with dynamic disorders.," Phys. Chem. Chem. Phys., vol. 12, no. 13, pp. 3309–14, 2010.

[98] L. Wang, D. Beljonne, L. Chen, and Q. Shi, "Mixed quantum-classical simulations of charge transport in organic materials: Numerical benchmark of the Su-Schrieffer-Heeger model," J. Chem. Phys., vol. 134, no. 24, p. 244 116, 2011.

[99] S. Ciuchi, S. Fratini, and D. Mayou, "Transient localization in crystalline organic semiconductors," Phys. Rev. B, vol. 83, no. 8, p. 081 202, 2011.

[100] W. P. Su, J. R. Schrieffer, and A. J. Heeger, "Solitons in Polyacetylene," Phys. Rev. Lett., vol. 42, no. 25, pp. 1698–1701, 1979.

[101] A. Troisi, "Prediction of the absolute charge mobility of molecular semiconductors: The case of rubrene," Adv. Mater., vol. 19, no. 15, pp. 2000–2004, 2007.

[102] A. Girlando, L. Grisanti, M. Masino, A. Brillante, R. G. Della Valle, and E. Venuti, "Interaction of charge carriers with lattice and molecular phonons in crystalline pentacene," J. Chem. Phys., vol. 135, no. 8, p. 084 701, 2011.

[103] I. G. Lang and Y. A. Firsov, "Kinetic Theory of Semiconductors With Low Mobility," J. Exptl. Theor. Phys., vol. 16, no. 5, pp. 1843–1860, 1963.

[104] F. Ortmann, F. Bechstedt, and K. Hannewald, "Theory of charge transport in organic crystals: Beyond Holstein's small-polaron model," Phys. Rev. B, vol. 79, p. 235 206, 2009.

[105] F. Ortmann, F. Bechstedt, and K. Hannewald, "Characteristics of small- and large-polaron motion in organic crystals," J. Phys. Condens. Matter, vol. 22, no. 46, p. 465 802, 2010.

[106] Z. Fan, J. H. Garcia, A. W. Cummings, J. E. Barrios-Vargas, M. Panhans, A. Harju, F. Ortmann, and S. Roche, "Linear Scaling Quantum Transport Methodologies," 2018.

[107] J. Ziman, Electrons and Phonons. Oxford University Press, 2001, ISBN: 9780198507796.

[108] S. H. Lin, C. H. Chang, K. K. Liang, R. Chang, Y. J. Shiu, J. M. Zhang, T.-S. Yang, M. Hayashi, and F. C. Hsu, "Ultrafast Dynamics and Spectroscopy of Bacterial Photosynthetic Reaction Centers," in Advances in Chemical Physics. John Wiley & Sons, Ltd, 2002, pp. 1–88, ISBN: 9780471264316.

[109] A. Troisi, "Dynamic disorder in molecular semiconductors: Charge transport in two dimensions," J. Chem. Phys., vol. 134, no. 3, p. 034 702, 2011.

[110] P. V. Parandekar and J. C. Tully, "Mixed quantum-classical equilibrium," J. Chem. Phys., vol. 122, no. 9, p. 094 102, 2005.

[111] K. Hannewald and P. A. Bobbert, "Anisotropy effects in phonon-assisted charge-carrier transport in organic molecular crystals," Phys. Rev. B, vol. 69, no. 7, p. 075 212, 2004.

[112] L. Wang and D. Beljonne, "Flexible Surface Hopping Approach to Model the Crossover from Hopping to Band-like Transport in Organic Crystals," J. Chem. Phys. Lett., vol. 4, no. 11, pp. 1888–1894, 2013.

[113] C. Perroni, F. Gargiulo, A. Nocera, V. Ramaglia, and V. Cataudella, "The Effects of Different Electron-Phonon Couplings on the Spectral and Transport Properties of Small Molecule Single-Crystal Organic Semiconductors," Electronics, vol. 3, no. 1, pp. 165–189, 2014.

[114] S. Ciuchi and S. Fratini, "Band dispersion and electronic lifetimes in crystalline organic semiconductors," Phys. Rev. Lett., vol. 106, no. 16, p. 166 403, 2011.

[115] G. De Filippis, V. Cataudella, A. S. Mishchenko, N. Nagaosa, A. Fierro, and A. De Candia, "Crossover from super- to subdiffusive motion and memory effects in crystalline organic semiconductors," Phys. Rev. Lett., vol. 114, no. 8, p. 086 601, 2015.

[116] J. Bonča, S. A. Trugman, and I. Batistić, "Holstein polaron," Phys. Rev. B, vol. 60, no. 3, pp. 1633–1642, 1999.

[117] H. Fehske and S. A. Trugman, "Numerical Solution of the Holstein Polaron Problem," in Polarons Adv. Mater. Dordrecht: Springer Netherlands, 2006, pp. 393–461.

[118] H. Wang, M. Thoss, and W. H. Miller, "Systematic convergence in the dynamical hybrid approach for complex systems: A numerically exact methodology," J. Chem. Phys., vol. 115, no. 7, pp. 2979–2990, 2001.

[119] T. C. Berkelbach, D. R. Reichman, and T. E. Markland, "Reduced density matrix hybrid approach: An efficient and accurate method for adiabatic and non-adiabatic quantum dynamics," J. Chem. Phys., vol. 136, no. 3, p. 034 113, 2012.

[120] A. J. Schile and D. T. Limmer, "Simulating conical intersection dynamics in the condensed phase with hybrid quantum master equations," J. Chem. Phys., vol. 151, no. 1, p. 014 106, 2019.

[121] H.-H. Teh, B.-Y. Jin, and Y.-C. Cheng, "Frozen-mode small polaron quantum master equation with variational bound for excitation energy transfer in molecular aggregates," J. Chem. Phys., vol. 150, no. 22, p. 224 110, 2019.

[122] J. Ranninger, "Spectral properties of small-polaron systems," Phys. Rev. B, vol. 48, no. 17, pp. 13 166–13 169, 1993.

[123] J. M. Robin, "Spectral properties of the small polaron," Phys. Rev. B, vol. 56, no. 21, pp. 13 634–13 637, 1997.

[124] J. Loos, M. Hohenadler, and H. Fehske, "Spectral functions of the spinless Holstein model," J. Phys. Condens. Matter, vol. 18, no. 8, pp. 2453–2472, 2006.

[125] F. J. Dyson, "The dynamics of a disordered linear chain," Phys. Rev., vol. 92, no. 6, pp. 1331–1338, 1953.

[126] G. Theodorou and M. H. Cohen, "Extended states in a one-demensional system with off-diagonal disorder," Phys. Rev. B, vol. 13, no. 10, pp. 4597–4601, 1976.

[127] C. M. Soukoulis and E. N. Economou, "Off-diagonal disorder in one-dimensional systems," Phys. Rev. B, vol. 24, no. 10, pp. 5698–5702, 1981.

[128] V. Cataudella, G. De Filippis, and C. A. Perroni, "Transport properties and optical conductivity of the adiabatic Su-Schrieffer-Heeger model: A showcase study for rubrene-based field effect transistors," Phys. Rev. B, vol. 83, no. 16, p. 165 203, 2011.

[129] N. Vukmirović, C. Bruder, and V. M. Stojanović, "Electron-phonon coupling in crystalline organic semiconductors: Microscopic evidence for nonpolaronic charge carriers," Phys. Rev. Lett., vol. 109, no. 12, p. 126 407, 2012.

[130] D. J. Thouless, "A relation between the density of states and range of localization for one dimensional random systems," J. Phys. C Solid State Phys., vol. 5, no. 1, pp. 77–81, 1972.

[131] Y. Li, V. Coropceanu, and J. L. Brédas, "Nonlocal electron-phonon coupling in organic semiconductor crystals: The role of acoustic lattice vibrations," J. Chem. Phys., vol. 138, no. 20, p. 204 713, 2013.

[132] S. Fratini, S. Ciuchi, D. Mayou, G. T. de Laissardière, and A. Troisi, "A map of high-mobility molecular semiconductors," Nat. Mater., vol. 16, no. October, pp. 998–1002, 2017.

[133] D. R. Yarkony and R. Silbey, "Variational approach to exciton transport in molecular crystals," J. Chem. Phys., vol. 67, no. 12, pp. 5818–5827, 1977.

[134] C. A. Perroni and V. Cataudella, "Interplay between electron-phonon coupling and disorder strength on the transport properties of organic semiconductors," Phys. Rev. B, vol. 85, no. 15, p. 155 205, 2012.

[135] N. Prodanović and N. Vukmirović, "Charge carrier mobility in systems with local electron-phonon interaction," Phys. Rev. B, vol. 99, no. 10, p. 104 304, 2019.

[136] M. T. Ruggiero, J. A. Zeitler, and A. Erba, "Intermolecular anharmonicity in molecular crystals: Interplay between experimental low-frequency dynamics and quantum quasi-harmonic simulations of solid purine," Chem. Commun., vol. 53, no. 26, pp. 3781–3784, 2017.

[137] O. Yaffe, Y. Guo, L. Z. Tan, D. A. Egger, T. Hull, C. C. Stoumpos, F. Zheng, T. F. Heinz, L. Kronik, M. G. Kanatzidis, J. S. Owen, A. M. Rappe, M. A. Pimenta, and L. E. Brus, "Local Polar Fluctuations in Lead Halide Perovskite Crystals," Phys. Rev. Lett., vol. 118, no. 13, p. 136 001, 2017.

[138] M. Z. Mayers, L. Z. Tan, D. A. Egger, A. M. Rappe, and D. R. Reichman, "How Lattice and Charge Fluctuations Control Carrier Dynamics in Halide Perovskites," Nano Lett., vol. 18, no. 12, pp. 8041–8046, 2018.

[139] D. Nicoletti and A. Cavalleri, "Nonlinear light–matter interaction at terahertz frequencies," Adv. Opt. Photonics, vol. 8, no. 3, p. 401, 2016.

[140] R. Mankowsky, A. Subedi, M. Först, S. O. Mariager, M. Chollet, H. T. Lemke, J. S. Robinson, J. M. Glownia, M. P. Minitti, A. Frano, M. Fechner, N. A. Spaldin, T. Loew, B. Keimer, A. Georges, and A. Cavalleri, "Nonlinear lattice dynamics as a basis for enhanced superconductivity in YBa2Cu3O6.5," Nature, vol. 516, no. 7529, pp. 71–73, 2014.

[141] T. Shi, E. Demler, and J. Ignacio Cirac, "Variational study of fermionic and bosonic systems with non-Gaussian states: Theory and applications," Ann. Phys. (N. Y)., vol. 390, pp. 245–302, 2018.

[142] C. Zhang, E. Jeckelmann, and S. White, "Dynamical properties of the one-dimensional holstein model," Phys. Rev. B, vol. 60, no. 20, pp. 14 092–14 104, 1999.

[143] C. Brockt, F. Dorfner, L. Vidmar, F. Heidrich-Meisner, and E. Jeckelmann, "Matrix-product-state method with a dynamical local basis optimization for bosonic systems out of equilibrium," Phys. Rev. B, vol. 92, no. 24, p. 241 106, 2015.

[144] M. Berciu, "Green's Function of a Dressed Particle," Phys. Rev. Lett., vol. 97, p. 036 402, 3 2006.

[145] L.-C. Ku, S. A. Trugman, and J. Bonča, "Dimensionality effects on the Holstein polaron," Phys. Rev. B, vol. 65, no. 17, p. 174 306, 2002.

[146] P. Werner and A. J. Millis, "Efficient dynamical mean field simulation of the holstein-hubbard model," Phys. Rev. Lett., vol. 99, no. 14, p. 146 404, 2007.

[147] Y. Murakami, P. Werner, N. Tsuji, and H. Aoki, "Ordered phases in the Holstein-Hubbard model: Interplay of strong Coulomb interaction and electron-phonon coupling," Phys. Rev. B, vol. 88, no. 12, p. 125 126, 2013.

[148] Y. Murakami, P. Werner, N. Tsuji, and H. Aoki, "Supersolid phase accompanied by a quantum critical point in the intermediate coupling regime of the holstein model," Phys. Rev. Lett., vol. 113, no. 26, p. 266 404, 2014.

[149] L. Vidmar, J. Bonča, M. Mierzejewski, P. Prelovek, and S. A. Trugman, "Nonequilibrium dynamics of the Holstein polaron driven by an external electric field," Phys. Rev. B, vol. 83, no. 13, p. 134 301, 2011.

[150] D. Golež, J. Bonča, L. Vidmar, and S. A. Trugman, "Relaxation Dynamics of the Holstein Polaron," Phys. Rev. Lett., vol. 109, no. 23, p. 236 402, 2012.

[151] E. Dagotto, "Correlated electrons in high-temperature superconductors," Rev. Mod. Phys., vol. 66, no. 3, pp. 763–840, 1994.

[152] M. Asher, D. Angerer, R. Korobko, Y. Diskin-Posner, D. A. Egger, and O. Yaffe, "Anharmonic Lattice Vibrations in Small-Molecule Organic Semiconductors," Adv. Mater., vol. 1908028, 2020.

[153] G. Schweicher, G. D'Avino, M. T. Ruggiero, D. J. Harkin, K. Broch, D. Venkateshvaran, G. Liu, A. Richard, C. Ruzié, J. Armstrong, A. R. Kennedy, K. Shankland, K. Takimiya, Y. H. Geerts, J. A. Zeitler, S. Fratini, and H. Sirringhaus, "Chasing the "Killer" Phonon Mode for the Rational Design of Low-Disorder, High-Mobility Molecular Semiconductors," Adv. Mater., vol. 1902407, p. 1 902 407, 2019.

[154] M. T. Ruggiero and J. A. Zeitler, "Resolving the origins of crystalline anharmonicity using terahertz time-domain spectroscopy and ab initio simulations," Journal of Physical Chemistry B, vol. 120, no. 45, pp. 11 733–11 739, 2016.

[155] A. C. Ferreira, S. Paofai, A. Létoublon, J. Ollivier, S. Raymond, B. Hehlen, B. Rufflé, S. Cordier, C. Katan, J. Even, and P. Bourges, "Direct evidence of weakly dispersed and strongly anharmonic optical phonons in hybrid perovskites," Commun. Phys., vol. 3, no. 1, 2020.

[156] N. W. Ashcroft and N. D. Mermin, Solid State Physics. Holt-Saunders, 1976.

[157] J. F. Scott, "Soft-mode spectroscopy: Experimental studies of structural phase transitions," Rev. Mod. Phys., vol. 46, no. 1, pp. 83–128, 1974.

[158] A. Subedi, A. Cavalleri, and A. Georges, "Theory of nonlinear phononics for coherent light control of solids," Phys. Rev. B, vol. 89, no. 22, p. 220 301, 2014.

[159] R. Mankowsky, M. Först, and A. Cavalleri, "Non-equilibrium control of complex solids by nonlinear phononics," Reports on Progress in Physics, vol. 79, no. 6, 2016.

[160] C. E. Patrick, K. W. Jacobsen, and K. S. Thygesen, "Anharmonic stabilization and band gap renormalization in the perovskite CsSnI3," Phys. Rev. B, vol. 92, no. 20, p. 201 205, 2015.

[161] Y.-N. Wu, W. A. Saidi, J. K. Wuenschell, T. Tadano, P. Ohodnicki, B. Chorpening, and Y. Duan, "Anharmonicity Explains Temperature Renormalization Effects of the Band Gap in SrTiO 3," J. Phys. Chem. Lett., vol. 11, no. 7, pp. 2518–2523, 2020.

[162] J. J. Zhou, O. Hellman, and M. Bernardi, "Electron-Phonon Scattering in the Presence of Soft Modes and Electron Mobility in SrTiO3 Perovskite from First Principles," Phys. Rev. Lett., vol. 121, no. 22, p. 226 603, 2018.

[163] Y. Li, Y. Yi, V. Coropceanu, and J. L. Brédas, "Symmetry effects on nonlocal electron-phonon coupling in organic semiconductors," Phys. Rev. B, vol. 85, no. 24, pp. 1–7, 2012.

[164] Z. Tu, Y. Yi, V. Coropceanu, and J. L. Brédas, "Impact of Phonon Dispersion on Nonlocal Electron-Phonon Couplings in Organic Semiconductors: The Naphthalene Crystal as a Case Study," J. Phys. Chem. C, vol. 122, no. 1, pp. 44–49, 2018.

[165] A. Troisi, "Charge transport in high mobility molecular semiconductors: classical models and new theories," Chem. Soc. Rev., vol. 40, no. 5, p. 2347, 2011.

[166] A. J. Millis, J. Hu, and S. Das Sarma, "Resistivity Saturation Revisited: Results from a Dynamical Mean Field Theory," Phys. Rev. Lett., vol. 82, no. 11, pp. 2354–2357, 1999.

[167] C. W. Li, X. Tang, J. A. Muñoz, J. B. Keith, S. J. Tracy, D. L. Abernathy, and B. Fultz, "Structural relationship between negative thermal expansion and quartic anharmonicity of cubic ScF3," Phys. Rev. Lett., vol. 107, no. 19, pp. 1–5, 2011.

[168] M. T. Ruggiero, S. Ciuchi, S. Fratini, and G. D'Avino, "Electronic Structure, Electron-Phonon Coupling, and Charge Transport in Crystalline Rubrene Under Mechanical Strain," J. Phys. Chem. C, vol. 123, no. 26, pp. 15 897–15 907, 2019.

[169] A. Landi, A. Peluso, and A. Troisi, "Quantitative Prediction of the Electro-Mechanical Response in Organic Crystals," Adv. Mater., vol. 33, no. 12, pp. 1–6, 2021.

[170] A. Y. Sosorev, O. Parashchuk, N. Tukachev, D. Maslennikov, D. Dominsky, O. Borshchev, M. S. Polinskaya, M. S. Skorotetcky, O. G. Kharlanov, and D. Paraschuk, "Suppression of dynamic disorder by electrostatic interactions in structurally close organic semiconductors," Phys. Chem. Chem. Phys., vol. 19, 2021.

[171] S. Illig, A. S. Eggeman, A. Troisi, L. Jiang, C. Warwick, M. Nikolka, G. Schweicher, S. G. Yeates, Y. Henri Geerts, J. E. Anthony, and H. Sirringhaus, "Reducing dynamic disorder in small-molecule organic semiconductors by suppressing large-amplitude thermal motions," Nat. Commun., vol. 7, p. 10 736, 2016.

[172] J. H. Fetherolf and T. C. Berkelbach, "Vibrational heat-bath configuration interaction," J. Chem. Phys., vol. 154, no. 7, 2021.

[173] R. B. Gerber, B. Brauer, S. K. Gregurick, and G. M. Chaban, "Calculation of anharmonic vibrational spectroscopy of small biological molecules," PhysChemComm, vol. 5, no. 21, p. 142, 2002.

[174] G. M. Chaban, J. O. Jung, and R. Benny Gerber, "Ab initio calculation of anharmonic vibrational states of polyatomic systems: Electronic structure combined with vibrational self-consistent field," J. Chem. Phys., vol. 111, no. 5, pp. 1823–1829, 1999.

[175] S. Carter, S. J. Culik, and J. M. Bowman, "Vibrational self-consistent field method for many-mode systems: A new approach and application to the vibrations of CO adsorbed on Cu(100)," J. Chem. Phys., vol. 107, no. 24, pp. 10 458–10 469, 1997.

[176] J. M. Bowman, S. Carter, and X. Huang, "Multimode: A code to calculate rovibrational energies of polyatomic molecules," International Reviews in Physical Chemistry, vol. 22, no. 3, pp. 533–549, 2003.

[177] T. K. Roy and R. B. Gerber, "Vibrational self-consistent field calculations for spectroscopy of biological molecules: new algorithmic developments and applications," Phys. Chem. Chem. Phys., vol. 15, no. 24, p. 9468, 2013.

[178] E. L. Sibert, "Theoretical studies of vibrationally excited polyatomic molecules using canonical Van Vleck perturbation theory," J. Chem. Phys., vol. 88, no. 7, pp. 4378–4390, 1987.

[179] S. Banik, S. Pal, and M. D. Prasad, "Calculation of vibrational energy of molecule using coupled cluster linear response theory in bosonic representation: Convergence studies," J. Chem. Phys., vol. 129, no. 13, 2008.

[180] P. Seidler and O. Christiansen, "Automatic derivation and evaluation of vibrational coupled cluster theory equations," J. Chem. Phys., vol. 131, no. 23, 2009.

[181] T. C. Thompson and D. G. Truhlar, "SCF CI calculations for vibrational eigenvalues and wavefunctions of systems exhibiting fermi resonance," Chem. Phys. Lett., vol. 75, no. 1, pp. 87–90, 1980.

[182] K. M. Christoffel and J. M. Bowman, "Investigations of self-consistent field, scf ci and virtual stateconfiguration interaction vibrational energies for a model three-mode system," Chem. Phys. Lett., vol. 85, no. 2, pp. 220–224, 1982.

[183] G. Avila and T. Carrington, "Using nonproduct quadrature grids to solve the vibrational Schrödinger equation in 12D," J. Chem. Phys., vol. 134, no. 5, p. 054 126, 2011.

[184] A. Leclerc and T. Carrington, "Calculating vibrational spectra with sum of product basis functions without storing full-dimensional vectors or matrices," J. Chem. Phys., vol. 140, no. 17, p. 174 111, 2014.

[185] M. Odunlami, V. Le Bris, D. Bégué, I. Baraille, and O. Coulaud, "A-VCI: A flexible method to efficiently compute vibrational spectra," J. Chem. Phys., vol. 146, no. 21, p. 214 108, 2017.

[186] B. Huron, J. P. Malrieu, and P. Rancurel, "Iterative perturbation calculations of ground and excited state energies from multiconfigurational zeroth-order wavefunctions," J. Chem. Phys., vol. 58, no. 12, pp. 5745–5759, 1973.

[187] R. J. Buenker and S. D. Peyerimhoff, "Individualized configuration selection in CI calculations with subsequent energy extrapolation," Theor. Chim. Acta, vol. 35, no. 1, pp. 33–58, 1974.

[188] R. J. Harrison, "Approximating full configuration interaction with selected configuration interaction and perturbation theory," J. Chem. Phys., vol. 94, no. 7, pp. 5021–5031, 1991.

[189] J. B. Schriber and F. A. Evangelista, "Communication: An adaptive configuration interaction approach for strongly correlated electrons with tunable accuracy," J. Chem. Phys., vol. 144, no. 16, p. 161 106, 2016.

[190] N. M. Tubman, J. Lee, T. Y. Takeshita, M. Head-Gordon, and K. B. Whaley, "A deterministic alternative to the full configuration interaction quantum Monte Carlo method," J. Chem. Phys., vol. 145, no. 4, 2016.

[191] N. M. Tubman, C. D. Freeman, D. S. Levine, D. Hait, M. Head-Gordon, and K. B. Whaley, "Modern Approaches to Exact Diagonalization and Selected Configuration Interaction with the Adaptive Sampling CI Method," J. Chem. Theory Comput., vol. 16, no. 4, pp. 2139–2159, 2020.

[192] A. A. Holmes, N. M. Tubman, and C. J. Umrigar, "Heat-Bath Configuration Interaction: An Efficient Selected Configuration Interaction Algorithm Inspired by Heat-Bath Sampling," J. Chem. Theory Comput., vol. 12, no. 8, pp. 3674–3680, 2016.

[193] A. A. Holmes, C. J. Umrigar, and S. Sharma, "Excited states using semistochastic heat-bath configuration interaction," J. Chem. Phys., vol. 147, no. 16, p. 164 111, 2017.

[194] S. Sharma, A. A. Holmes, G. Jeanmairet, A. Alavi, and C. J. Umrigar, "Semistochastic Heat-Bath Configuration Interaction Method: Selected Configuration Interaction with Semistochastic Perturbation Theory," J. Chem. Theory Comput., vol. 13, no. 4, pp. 1595–1604, 2017.

[195] J. Li, M. Otten, A. A. Holmes, S. Sharma, and C. J. Umrigar, "Fast semistochastic heat-bath configuration interaction," J. Chem. Phys., vol. 149, no. 21, p. 214 110, 2018.

[196] K. T. Williams, Y. Yao, J. Li, L. Chen, H. Shi, M. Motta, C. Niu, U. Ray, S. Guo, R. J. Anderson, J. Li, L. N. Tran, C. N. Yeh, B. Mussard, S. Sharma, F. Bruneval, M. Van Schilfgaarde, G. H. Booth, G. K. L. Chan, S. Zhang, E. Gull, D. Zgid, A. Millis, C. J. Umrigar, and L. K. Wagner, "Direct Comparison of Many-Body Methods for Realistic Electronic Hamiltonians," Phys. Rev. X, vol. 10, no. 1, p. 11 041, 2020.

[197] Y. Yao, E. Giner, J. Li, J. Toulouse, and C. J. Umrigar, "Almost exact energies for the Gaussian-2 set with the semistochastic heat-bath configuration interaction method," J. Chem. Phys., vol. 153, no. 12, p. 124 117, 2020.

[198] J. J. Eriksen, T. A. Anderson, J. E. Deustua, K. Ghanem, D. Hait, M. R. Hoffmann, S. Lee, D. S. Levine, I. Magoulas, J. Shen, N. M. Tubman, K. B. Whaley, E. Xu, Y. Yao, N. Zhang, A. Alavi, G. K.-L. Chan, M. Head-Gordon, W. Liu, P. Piecuch, S. Sharma, S. L.

Ten-no, C. J. Umrigar, and J. Gauss, "The Ground State Electronic Energy of Benzene," J. Phys. Chem. Lett., pp. 8922–8929, 2020.

[199] G. Rauhut, "Configuration selection as a route towards efficient vibrational configuration interaction calculations," J. Chem. Phys., vol. 127, no. 18, 2007.

[200] M. Neff and G. Rauhut, "Toward large scale vibrational configuration interaction calculations," J. Chem. Phys., vol. 131, no. 12, 2009.

[201] P. Carbonnière, A. Dargelos, and C. Pouchan, "The VCI-P code: An iterative variation-perturbation scheme for efficient computations of anharmonic vibrational levels and IR intensities of polyatomic molecules," Theor. Chem. Acc., vol. 125, no. 3-6, pp. 543–554, 2010.

[202] M. Sibaev and D. L. Crittenden, "Balancing accuracy and efficiency in selecting vibrational configuration interaction basis states using vibrational perturbation theory," J. Chem. Phys., vol. 145, no. 6, p. 064 106, 2016.

[203] Y. Scribano and D. M. Benoit, "Iterative active-space selection for vibrational configuration interaction calculations using a reduced-coupling VSCF basis," Chem. Phys. Lett., vol. 458, no. 4-6, pp. 384–387, 2008.

[204] E. Lesko, M. Ardiansyah, and K. R. Brorsen, "Vibrational adaptive sampling configuration interaction," J. Chem. Phys., vol. 151, no. 16, p. 164 103, 2019.

[205] E. G. Kratz, LOVCI: Ladder operator vibrational configuration iteraction, `https://github.com/kratman/VibCI`, 2016.

[206] J. H. Fetherolf, VHCI: Vibrational heat-bath configuration interaction v0.1, `https://github.com/berkelbach-group/VHCI`, version v0.1, Oct. 2020.

[207] G. Guennebaud, B. Jacob, et al., Eigen v3, `http://eigen.tuxfamily.org`, 2010.

[208] Y. Qiu, SPECTRA: Sparse eigenvalue computation toolkit as a redesigned ARPACK, `https://spectralib.org/`, 2015.

[209] J. Brown and T. Carrington, "Using an expanding nondirect product harmonic basis with an iterative eigensolver to compute vibrational energy levels with as many as seven atoms," J. Chem. Phys., vol. 145, no. 14, p. 144 104, 2016.

[210] P. S. Thomas, T. Carrington, J. Agarwal, and H. F. Schaefer, "Using an iterative eigensolver and intertwined rank reduction to compute vibrational spectra of molecules with more than a dozen atoms: Uracil and naphthalene," J. Chem. Phys., vol. 149, no. 6, 2018.

[211] D. Begue, P. Carbonniere, and C. Pouchan, "Calculations of Vibrational Energy Levels by Using a Hybrid ab Initio and DFT Quartic Force Field: Application to Acetonitrile," J. Phys. Chem. A, vol. 109, no. 20, pp. 4611–4616, 2005.

[212] R. Garnier, M. Odunlami, V. Le Bris, D. Bégué, I. Baraille, and O. Coulaud, "Adaptive vibrational configuration interaction (A-VCI): A posteriori error estimation to efficiently compute anharmonic IR spectra," J. Chem. Phys., vol. 144, no. 20, pp. 1–4, 2016.

[213] T. Delahaye, A. Nikitin, M. Rey, P. G. Szalay, and V. G. Tyuterev, "A new accurate ground-state potential energy surface of ethylene and predictions for rotational and vibrational energy levels," J. Chem. Phys., vol. 141, no. 10, 2014.

[214] M. Sibaev and D. L. Crittenden, "The PyPES library of high quality semi-global potential energy surfaces," J. Comput. Chem., vol. 36, no. 29, pp. 2200–2207, 2015.

[215] M. Sibaev and D. L. Crittenden, "PyVCI: A flexible open-source code for calculating accurate molecular infrared spectra," Comput. Phys. Commun., vol. 203, pp. 290–297, 2016.

[216] D. Bégué, N. Gohaud, C. Pouchan, P. Cassam-Chenaï, and J. Liévin, "A comparison of two methods for selecting vibrational configuration interaction spaces on a heptatomic system: Ethylene oxide," J. Chem. Phys., vol. 127, no. 16, p. 164 115, 2007.

[217] E. Cané, A. Miani, and A. Trombetti, "Anharmonic force fields of naphthalene-h8 and naphthalene-d 8," J. Phys. Chem. A, vol. 111, no. 33, pp. 8218–8222, 2007.

[218] I. Baraille, C. Larrieu, A. Dargelos, and M. Chaillet, "Calculation of non-fundamental IR frequencies and intensities at the anharmonic level. I. The overtone, combination and difference bands of diazomethane, H2CN2," Chem. Phys., vol. 273, no. 2-3, pp. 91–101, 2001.

[219] R. Burcl, S. Carter, and N. C. Handy, "Infrared intensities from the MULTIMODE code," Chem. Phys. Lett., vol. 380, no. 3-4, pp. 237–244, 2003.

[220] V. Le Bris, M. Odunlami, D. Bégué, I. Baraille, and O. Coulaud, "Using computed infrared intensities for the reduction of vibrational configuration interaction bases," Phys. Chem. Chem. Phys., vol. 22, no. 13, pp. 7021–7030, 2020.

[221] K. Kim, K. D. Jordan, and T. S. Zwier, "Low-Energy Structures and Vibrational Frequencies of the Water Hexamer: Comparison with Benzene-(H2O)6," J. Am. Chem. Soc., vol. 116, no. 25, pp. 11 568–11 569, 1994.

[222] Z. Bačić and J. C. Light, "Theoretical Methods For Rovibrational States Of Floppy Molecules," Annu. Rev. Phys. Chem., vol. 40, no. 1, pp. 469–498, 1989.

[223] M. J. Bramley, J. W. Tromp, T. Carrington, and G. C. Corey, “Efficient calculation of highly excited vibrational energy levels of floppy molecules: The band origins of h + 3 up to 35 000 cm -1,” J. Chem. Phys., vol. 100, no. 9, pp. 6175–6194, 1994.